Thermal management and temperature control of a containerised rapid deployment radar system

Thesis presented in partial fulfilment of the requirements
for the degree of Master of Science in Engineering
at the University of Stellenbosch

Y. Jeggels

Supervisor: RT Dobson

March 2008

Department of Mechanical and Megatronic Engineering
University of Stellenbsoch

Declaration

I, Yusuf Jeggels, the undersigned, hereby declare that the work contained in this thesis is my own original work and has not previously, in its entirety or in part, been submitted for any university degree.

Signature of Candidate

Summary

The thermal problems of the ESR 220 radar system (Kameelperd) have been investigated. To address this and other potential thermal problems a thermal management design process methodology was developed.

The transistors in the high power amplifier (HPA), within the radar equipment container (REC), failed due to thermal shock and excessively high temperatures at high system container air temperatures. The only way to ensure that the transistors in the existing design do not overheat is to cool the system container air to a temperature well below the comfort level of the operating personnel. The four processor boards of the digital signal processors (DSP) exceed their temperature specification if the fans inside the DSP are switched off.

The thermal management design process methodology was used to analyse the Kameelperd, which resulted in the air flow inside the REC and the existing HPA cooling solution being analysed. Alternative HPA cooling solutions need to be explored as possible replacements for the existing HPA cooling solution.

Flomerics FLOTHERM computational fluid dynamics program was used to analyse the air flow through the REC. The analysis showed that the inappropriate positioning and configuration of the various units in the REC not only limits the total air flow rate through the container, but also inhibits the distribution of air to the DSP processors. It is proposed that the receiver front end and driver amplifier be redesigned such that they are open in the horizontal plane. In addition the positioner interface must be removed and the electromagnetic interference (EMI) shield at the entrance of the REC be replaced or removed. The proposed changes will improve the total air flow rate and the distribution of the air flow inside the REC. If the proposed changes are to be applied to the REC, then the system container air flow exit configuration needs to be changed.

A numerical model, based on experimental data of the existing HPA cooling solution, was used to calculate the HPA transistor base temperature and determined that it is

around 65 °C. Alternative HPA cooling solutions must have a transistor base temperature below 65 °C.

The concepts evaluated for the design of the alternative HPA cooling solution include water cooled cold plate, heat pipes, bent thermosyphon and closed loop thermosyphon designs. The water cooled cold plate design was rejected, while the heat pipe design was not feasible. After applying the thermal management design process methodology to the bent thermosyphon and closed loop thermosyphon designs, the only unknown parameters for the designs were the thermal resistance and maximum heat transfer rate for each thermosyphon. The required energy could not be transferred by a single bent thermosyphon. Three closed loop thermosyphons with different diameters (¼", ⅜" and ½" outside diameter pipes) were tested using three different working fluids (R134a, butane and water) with different fill ratios. The recommended alternative HPA cooling solution uses a single ½" water filled closed loop thermosyphon. Depending on the cooling fluid temperature, flow rate and cold plate design, the alternative HPA cooling solution can achieve a transistor base temperature of 65 °C.

It is concluded that the thermal management design process methodology must be implemented from the start of the design process so that the thermally associated risk of the product would have been significantly reduced, if not eliminated.

Opsomming

Die termise probleme van die ESR 220 radar stelsel (Kameelperd) was ondersoek. 'n Termiese bestuur ontwerp proses metodologie was ontwikkel om hierdie en ander potentieële termiese probleme aan te spreek.

Die HPA is geleë binne in die radar toerusting houer (REC). Die transistors in die hoë krag versterker (HPA) faal as gevolg van termiese skok en buitensporige hoë temperature wanneer die sisteem houer se lugtemperatuur hoog is. Die enigste manier om te verseker dat die transistors nie oorverhit nie, is om die lugtemperatuur van die sisteemhouer onverdraaglik laag te maak vir die operateurs. As die waaiers in die digitale sein verwerker (DSP) afgeskakel word oorskry die vier verwerker borde in die DSP die gespesifieseerde/aangewese temperatuur.

Die termiese bestuur ontwerp proses metodologie was gebruik om die Kameelperd te analiseer. Die resultaat het aangedui dat die lugvloei in die REC en die bestaande HPA verkoeling metode geanaliseer moet word. Alternatiewe verkoelings metodes moet ondersoek word as 'n vervangings moontlikheid vir die bestaande HPA verkoelingsmetode.

Flomerics FLOTHERM CFD program was gebruik om die lugvloei deur die REC te analiseer. Die analise het aangedui dat die posisionering en konfigurasie van die eenhede ontoepaslik was en dat dit nie slegs die lugvloei deur die REC beperk nie, maar ook die verspreiding van lug deur die DSP verwerkers verhinder. Daar word voorgestel dat die 'receiver front end' en die 'driver amplifier' her-ontwerp moet word. Daar word ook voorgestel dat die 'positioner interface' verwyder word en die 'EMI shield' verwyder of her-ontwerp moet word. Die voorgestelde veranderinge sal die lugvloei snelheid en die lugverspeiding verbeter. As die voorgestelde veranderinge aan die REC aangewend word dan moet lugvloei uitlaat konfigurasie van die sisteem houer verander word.

'n Numerise model, gebaseer op die eksperimentele data vir die bestaande HPA verkoelingsmetode, was gebruik om die transistor basis temperatuur te bereken en

dit is bepaal dat dit om en by 65 ºC is. Die alternatiewe verkoelings metodes moet dan verseker dat die transistor basis temperatuur onder 65 ºC bly.

Die konsepte wat ge-evalueer was vir die ontwerp van die alternatiewe HPA verkoelingsmetode, sluit in, water-verkoelings plaat, 'heat pipe', gebuigde 'thermosyphon', geslote lus 'thermosyphon'ontwerpe. Die water-verkoelings plaat ontwerp was verwerp terwyl die 'heat pipe'ontwerp nie uitvoerbaar was nie. Die enigste onbekende parameter vir die gebuigde 'thermosyphon' en die geslote lus 'thermosyphon' ontwerpe was die termiese weerstand en maksimum hitte oordrag vir elke 'thermosyphon'. Die gebuigde 'thermosyphon' kon nie die benodigde energie oordra nie. Drie geslote lus 'thermosyphon' met verskillende deursnitte (¼", ⅜" en ½" buite deursnitte) was getoets met drie verskillende vloeistowwe (R134a, butane en water) met verskillende vullings ratios. Die voorgestelde alternatiewe HPA verkoelingsmetode gebruik 'n enkele ½" water gevulde geslote lus 'thermosyphon'. Afhangend van die verkoelings vloeistof temperatuur, vloeisnelheid en verkoelingsplaat ontwerp, kan die alternatiewe HPA verkoelings metode 'n transistor basis temperatuur van minder as 65 ºC behaal.

Daar is dus tot 'n gevolgtrekking gekom dat die termiese bestuur ontwerp proses metodologie, vanaf die aanvang van die ontwerp proses geimplementeer moet word, sodat die termiese risiko verbonde aan die produk aansienlik verminder of elimineer word.

Acknowledgements

The author would like to acknowledge the following persons for their help and assistance during the project.

Mr. R.T. Dobson of Stellenbosch University

Ms. D. Chan of Flomerics, U.K.

Mr. A. Graham of Reutech Radar Systems.

Mr. C.J. Zietsmann and the technical staff at the Department of Mechanical Engineering, Stellenbosch University

Contents

List of figures

List of tables

Nomenclature

A	Area, m²
c	Length, m
c_p	Specific heat, J/(kg·K)
D	Diameter, m
FR	Filling ratio
H	Height, m
h	Heat transfer coefficient, W/m²·K
h_{fg}	Latent heat of vaporisation, kJ/kg
k	Thermal conductivity, W/(m·K)
L	Length, m
m	Mass, kg
m	Integer
$\dot{m}$	Mass flow rate, kg/s
n	Integer
Nu	Nusselt number
P	Pressure, Pa
P	Perimeter, m
Pr	Prandtl number
$\dot{Q}$	Heat transfer rate, W
$\dot{Q}''$	Heat flux, W/m²
$\dot{Q}'''$	Heat transfer rate per unit volume, W/m³
R	Thermal resistance, K/W
R	Electrical resistance, Ω
R	Specific gas constant, J/(kg·K)
Re	Reynolds number
S	Temperature spread, °C
T	Temperature, °C or K
t	Thickness, m
w	Width, m
y	Length, m

z	Length, m
β	Angle, °
ρ	Density, kg/m³
η	Efficiency
μ	Viscosity, Pa s
σ	Surface tension, N/m²

Subscripts

av	Average
c	Condenser plate
c	Channel
g	Generated at a specific node
h	Evaporator plate, hot
h	Hydraulic
h	Heat dissipated
hsb	Heat sink base (mean)
i	Inlet
l	Liquid
m	Water
max	Maximum
min	Minimum
o	Outlet
p	Plate
t	Total
w	Wall

Abbreviations

ACU	Air conditioning unit
CLTS	Close loop thermosyphon
CSLD	Cooling solution level definitions
BTS	Bent thermosyphon
DA	Driver amplifier
DSP	Digital signal processor
EMI	Electromagnetic interference
FR	Fill ratio
FOM	Figure of merit
HPA	High power amplifier
LRU	Line replaceable unit
PSI	Positioner interface
REC	Radar equipment container
RFE	Receiver front end
SYN	Synthesiser
TMDP	Thermal management design process

Chapter 1 Introduction

Electronic equipment has various life spans, ranging typically from 5 years for cell phones to 10 years for computers. However, military systems have a service life in excess of 30 years. During that time, the military systems are periodically upgraded. These upgrades can include improved armour and weapons, but can also include electronic based upgrades, such as sights, laser range finders, targeting systems, etc (Gelbart, 2004). When a military system's electronic equipment is upgraded, new thermal problems may arise. These problems are often due to the increase in electronic equipment power densities and designers not taking the thermal management of the new electronic equipment as a whole into account.

This project arises from the thermal problems encountered with the ESR 220 'Kameelperd' system. The thermal problems will be described and analysed in Chapter 3. A brief introduction to the Kameelperd is given in section 1.1.3. From the analysis of Chapter 3, changes to radar system will be recommended. The thermal analysis of proposed changes is documented in Chapter 4. The proposed changes will use two-phase heat transfer devices, such as bent and closed loop thermosyphons. The two-phase heat transfer devices' thermal resistance and maximum heat transfer rates will be experimentally determined. Correlations for the heat transfer coefficients will be calculated.

Important to the effective design of electronic equipment is the methodology or process for the thermal management of the system. Jeggels (2007) discusses a thermal management methodology, followed by general guidelines for the thermal design of electronic equipment. An introduction to Jeggels (2007) is given in Chapter 2.

1.1. Literature study

The literature study has been divided into three sections. The first discusses literature dealing with the thermal management philosophy, while the second deals

with specific cooling solutions or the method in which heat is transferred. The third gives a brief introduction to the Kameelperd and the radar equipment container.

1.1.1. Thermal management philosophy

Articles by Minichiello and Belady (2002) and Belady, Kelkar and Patankar (2006) all refer to the "enhanced product development process", a design philosophy first published by Belady (2001). Sergent and Krum (1998) give their own thermal design process based on a process flow chart, which is shown in Figure 1-1. Figure 1-1 also gives Sergent and Krum's (1998) explanation for the design logic flow chart. Belady's (2001) "enhanced product development process" and Sergent and Krum (1998) thermal design process flow chart are used in the thermal management design process methodology.

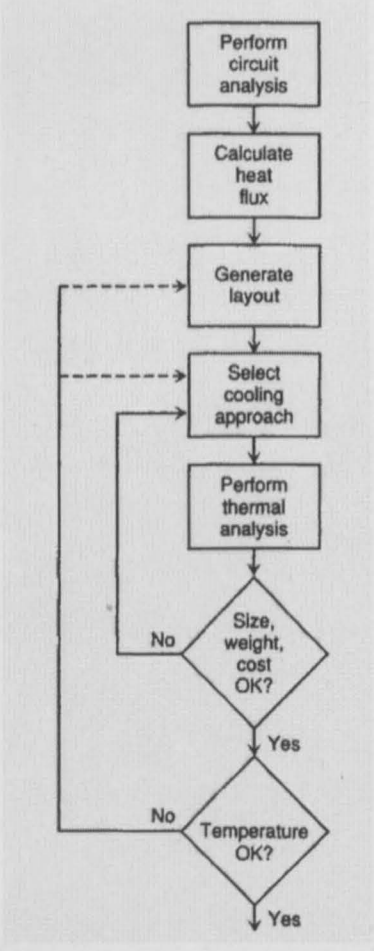

From Sergent and Krum (1998): "Thermal design is an iterative process. The temperature of various points in the circuit depends on the location of the heat generated elements and the thermal path. A process of flow chart for the thermal design is shown in" Figure 1-1. "The layout (of the design) is generated and the heat flux at each point of the topography is calculated. From this data, a preliminary cooling approach is selected and a thermal analysis is performed on the overall combination (overall thermal design). The layout and/or the thermal path is adjusted until the thermal analysis indicates that the temperature is below the desired level. Several approaches may be compared for cost, weight, and size, and the thermal design may be optimized for all these criteria in the shortest time."

Figure 1-1: Thermal design process flow chart (Sergent and Krum, 1998)

1.1.2. Cooling solutions

A cooling solution is the method of heat transfer employed to transfer heat from one object or location to another. Phase change materials, direct air cooling, indirect water cooling are some examples of cooling solutions. Articles, in most cases, deal with a specific cooling solution or an experimental method which may not be commercially viable. Sergent and Krum (1998), Kraus and Bar-Cohen (1983), Yeh and Chu (2002) and Steinberg (1980) deal with the cooling solutions shown in Table 1-1. Various cooling solutions are given in Table 1-1, with possible item levels given. The item level indicates the position of the cooling solution in the heat transfer path from a component item to the environment.

Table 1-1: Various cooling solutions

Cooling solutions	Details	Item level
Conduction	Conduction heat transfer	Any level, but not recommended higher than component level
Natural convection	Components mounted on a vertical PCB	Component
Direct air cooling	Forced convection cooling	Any
Indirect air cooling	Forced convection cooling, cold plate	Not component
Direct water cooling		Component
Indirect two-phase cooling	Forced convection boiling	Not component
Direct two-phase cooling	Spray cooling, immersion component cooling	Component
Heat pipes	Not really a cooling solution by itself but will make other cooling solutions better.	Any
Thermoelectric coolers		Component
Phase change materials		Component

1.1.3. ESR 220 'Kameelperd' and its radar equipment container

The ESR 220 'Kameelperd' system, is a highly mobile solid state L-band 2D surveillance radar (system) designed to provide early warning to mechanised troops in the battlefield (RRS, 2007). It is a fully autonomous armoured system with self-

contained power plant packaged on a single vehicle. The radar system is contained in a system container, which can be mounted on an all-terrain 8x8 transporter.

The system container supports the mast mounted radar antenna. The mast can be rotated vertically, thereby giving the radar antenna higher ground clearance. The system container is shown in Figure 1-2 mounted on the transporter. Although the antenna is shown deployed, the mast is in its storage position.

Figure 1-2: ESR 220 "Kameelperd", shown with the mast in storage position.

The radar equipment container (REC) is located in the system container, as shown in Figure 1-3. The REC consists of the following units: the high power amplifier (HPA), the receiver front end (RFE), the driver amplifier (DA), the synthesiser (SYN), the digital signal processor (DSP) and the positioner interface (PSI). These units are shown in Figure 1-4 alongside their container. The entrance of the HPA blower is shown in Figure 1-4. More detail on the units will be given in Chapter 3, when the thermal problems are discussed.

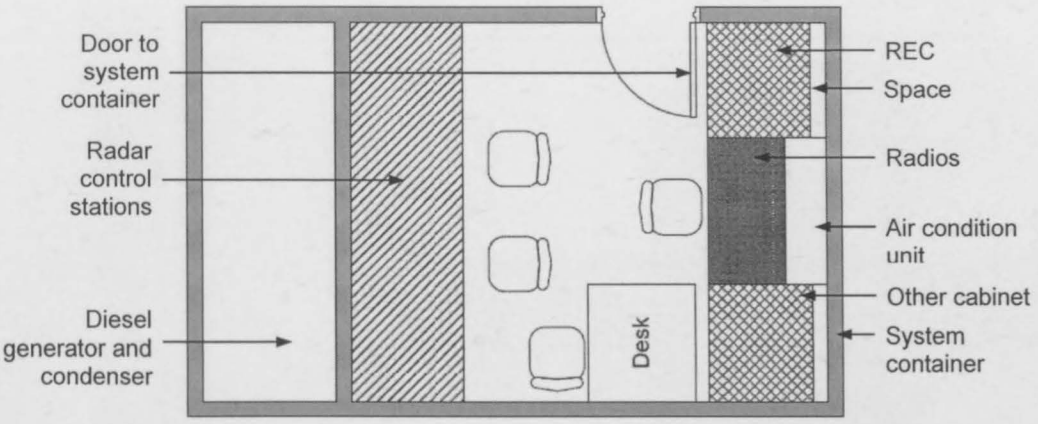

Figure 1-3: Plan of system container. Not to scale.

The system container has seating for four personnel, namely a radio operator, two radar operators and a commander. The air conditioning unit above and slightly behind the radios can be blocked from the main seating area by books above the radios. There is a 100mm space between the back of the REC and the system container wall. The REC is open at the bottom on all sides. Another air condition unit is under the radar control stations. It provides biological and chemical warfare filtered air to the system container, at a pressure greater than atmospheric.

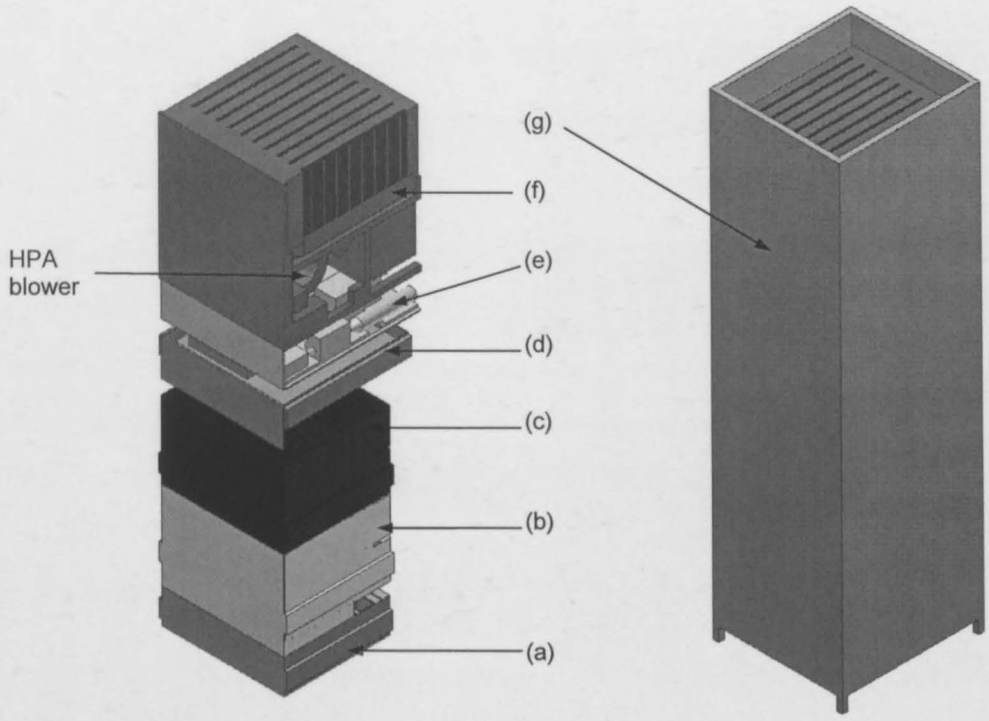

Figure 1-4: Sketch of the REC without the housing (left) and with a simple container (right). Shown in the figure are the PSI (a), DSP (b), SYN (c), DA (d), RFE (e) and the HPA (f). The position of the door to the REC is indicated by (g).

1.2. Thesis Objectives

The following are the objectives of this thesis as listed in the thesis proposal (Jeggels, 2006)

1. Investigate the air flow in the existing radar container.
2. Recommend ameliorating interventions to the existing system so that the air flow rate in the system can be increased.
3. Set up a thermal design methodology.
4. Apply the thermal design methodology to the existing radar container and to any proposed changes that might come about from the application of the methodology to the existing radar system.

Chapter 2 Thermal management design process for electronic equipment

This chapter discusses the document "thermal management design process for electronic equipment" (Jeggels, 2007), which details a thermal design process that can be used in the thermal design of electronic equipment. This thermal design process will be referred to as the thermal management design process (TMDP) and consists of two sections. The first is called the TDMP methodology. It is the core of the TDMP and is discussed in section 2.1. The second section is the general electronic equipment design guidelines for the TMDP and is discussed in section 2.2.

2.1. Thermal management design process methodology

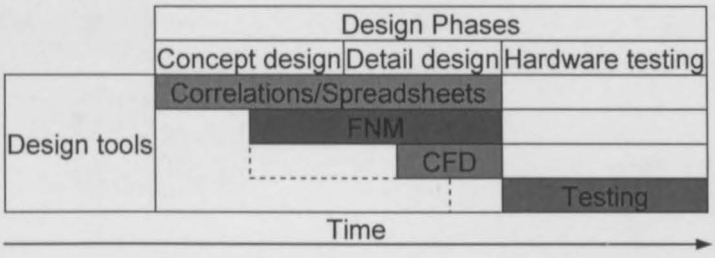

Figure 2-1: The three design phases of the thermal management design process methodology, based on a modified enhanced product design cycle by Belady (2001)

The TMDP methodology consists of the three design phases and support materials. The design phases are based on the "enhanced product development process" first published by Belady (2001). The first phase of the methodology is the concept design phase, which uses correlations and spreadsheets to evaluate different designs. The second phase is the detailed design phase, where correlations and spreadsheets may still be used, but depending on the complexity of the design, flow network modelling (FNM), computation fluid dynamics (CFD) or a combination of the aforementioned may be used. When the electronic equipment has been manufactured, the designer needs to confirm that the equipment is working as

Chapter 3 Thermal analysis of the radar system

To apply the TMDP, the thermal problems of the Kameelperd must first be known. Air conditioning units (ACU) have been installed in the system container. When the Kameelperd is transmitting, transistors and power supply units in the HPA fail. To get the HPA to an acceptable temperature, the system container air temperature was decreased to as low as 8 °C. As a guideline, air temperature while doing "seated thinking tasks" is between 18-24 °C (Dul and Weerdmeester, 2001). The operators found this too cold and switched off the ACU, resulting in the HPA overheating. To prevent overheating, the ACU are always on when the radar system is on. Then the operators opened the doors while transmitting, also resulting in the HPA overheating. It is now required that the doors be closed while the Kameelperd is transmitting. There is also an uncertainty to how the air gets into the REC.

When the DSP was upgraded, it was found that the processor chips exceeded their temperature specifications (Graham, 2007). A fan tray was installed and, as with the ACU in the system container, is always operating when the radar system is on.

The thermal management of electronic equipment needs to be taken into account from the beginning of the design process to have an effective design. This will not necessarily guarantee that the equipment will be without thermal problems, but will decrease the thermally associated risk to the product (Minichiello and Belady, 2002). It was decided not to apply the three design phases of the TMDP methodology to the Kameelperd. However, the cooling solution level definitions analysis (CSLD) was applied to the radar system and is shown below.

1. Conduction from the transistors to the subunit's aluminium case. The transistors and subunit case are 1st and 5th level items. Note that although conduction takes place between two objects, there is no thermal paste involved. The transistors are earthed through its base. Adding thermal paste between the transistor base and the plate added too much capacitance to the earth of the transistors (Graham, 2007).
2. Conduction and convection in the subunit case.

3. The subunit is mounted in a unit, which are 5th and 6th level items. Heat transfer takes place from the subunit's finned case surface to the air flow generated by the unit's blower.
4. The air flows through the rack, in which the unit is mounted. The unit and rack are 6th and 7th level items, respectively.
5. The air flow leaves the rack to the system container, which are 7th and 8th level items, respectively.
6. The air flow leaves the system container.

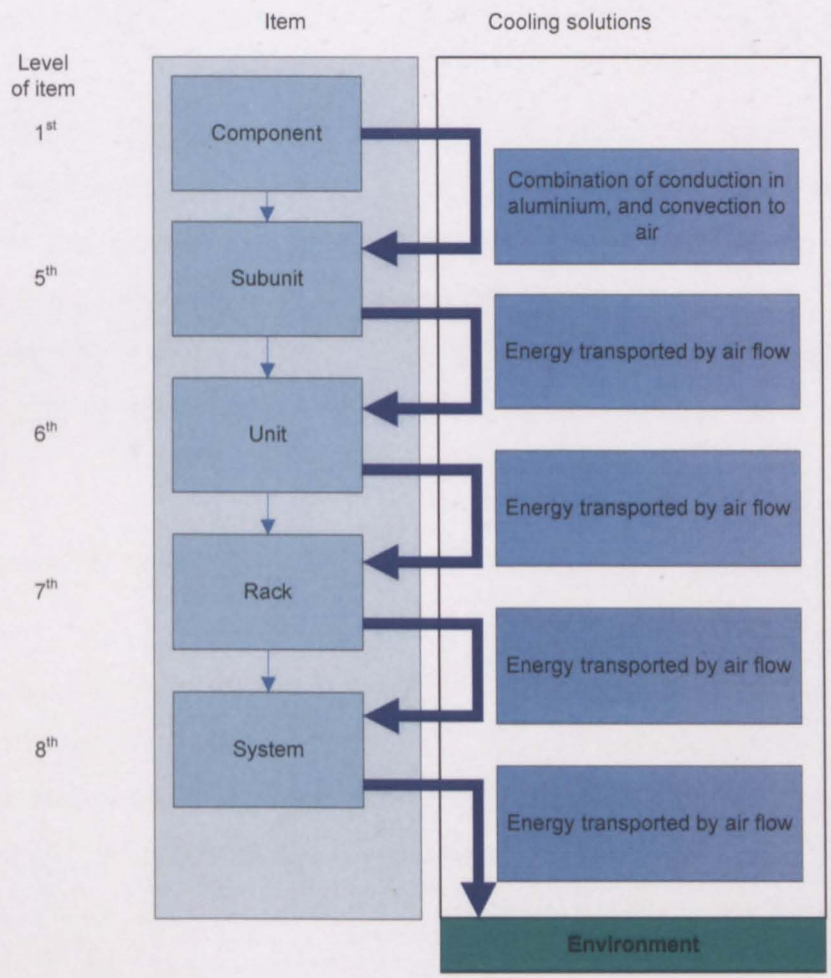

Figure 3-1: Cooling solution level definition breakdown of the radar system

The heat dissipated by the transistors is transferred to the air flow, generated by the HPA blower, through the HPA subunits by conduction through a thermal contact interface, conduction in thermal paste and aluminium and convection. The thermal

problems arise in the heat transfer methods in which the heat is transferred to the environment. The air flow is dependent and, in the current system, restricted by the pressure drops in the high power amplifier subunit, the rack, the entrance of the rack, the exit of the rack, and the exit to the environment through the system container wall. This is also shown in Figure 3-1 with the number of cooling solutions "energy transported by air flow".

Using the discussed thermal problems and the CSLD analysis, the radar system thermal analysis will be divided into an evaluation of the flow inside the REC and an analysis of the HPA cooling solution.

The air flow inside the REC will be evaluated using Flomeric's FLOTHERM computational fluid dynamics (CFD) program. The experimental analysis of the REC (section 3.1) is followed by the CFD analysis (section 3.2), which includes the comparison of the experimental data and the CFD data with the intention to validate the CFD analysis. The results of the CFD analysis are discussed in section 3.3. The analysis of the HPA cooling solution is discussed in section 3.4.

3.1. Experimental analysis of the air flow inside the REC

Experimental data is used to validate the FLOTHERM simulation of the REC. It also provides data for the FLOTHERM simulation. This section details the experimental set up and procedure used to acquire the experimental data. The data gathered is then processed and used to validate the simulation.

3.1.1. Experimental set up

The purpose of the experiment is to gather air flow data for the REC. This, under ideal circumstances, would include getting mass and energy balances. However, due to the complex nature of the REC, this is not possible for the system as a whole. The Kameelperd is an operational system owned by the South African National Defence

Force. Therefore, no permanent changes may be made to the system to facilitate the measurement of the air flow inside the REC.

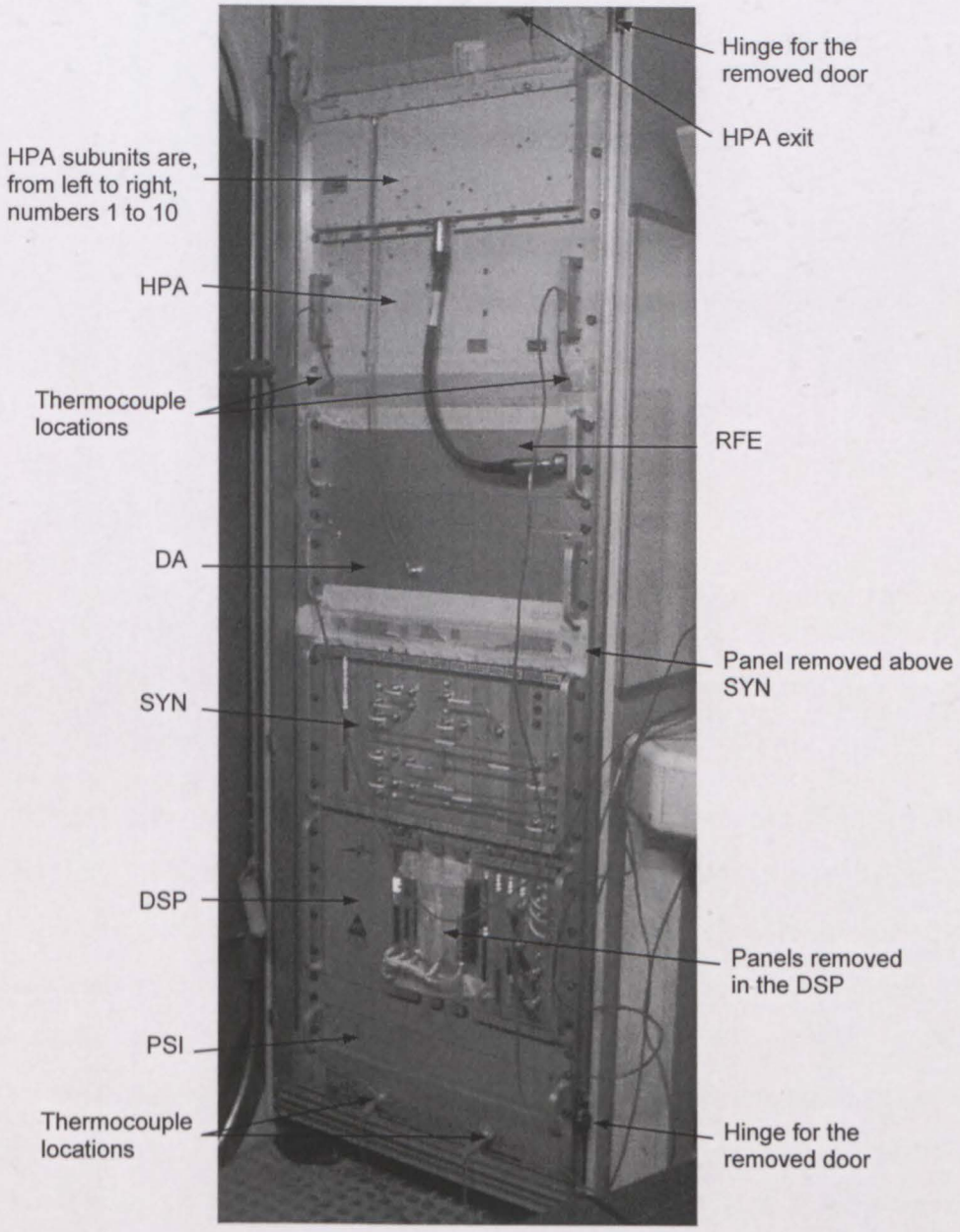

Figure 3-2: Experimental set up of the REC

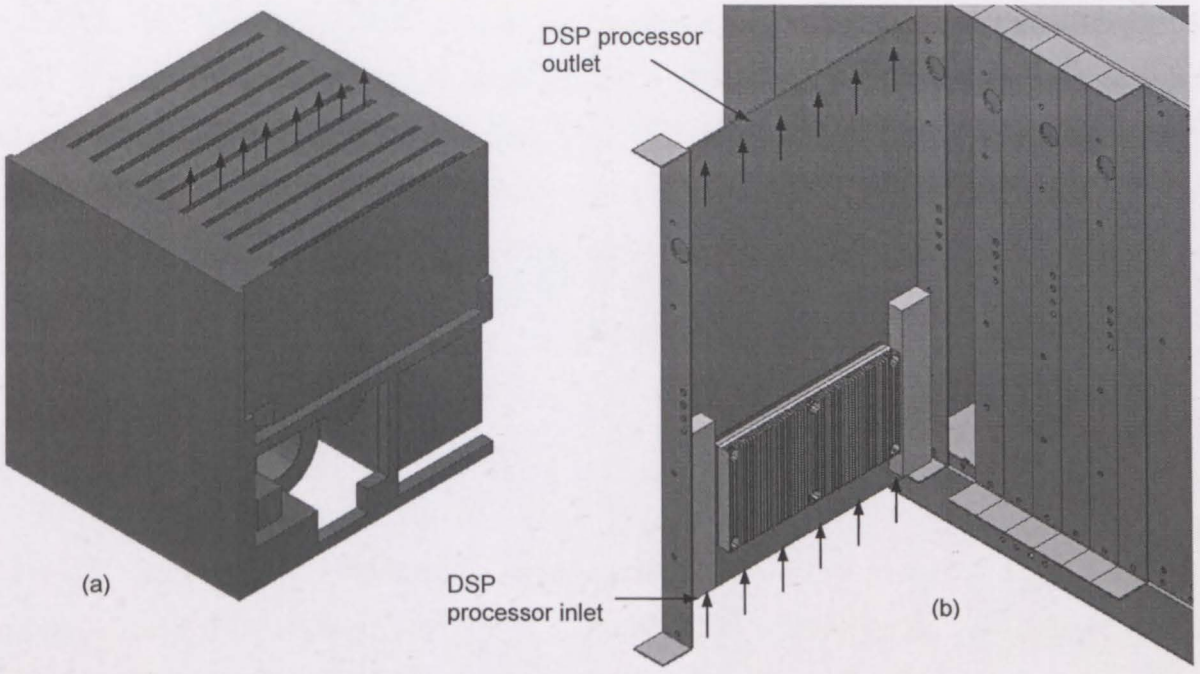

Figure 3-3: Velocity measurement locations for the HPA outlet (a) and DSP processor (b)

The exit air flow rate can be measured at the high power amplifier's (HPA) exit, shown in Figure 3-2 and Figure 3-3 (a). However, in order to gain access to the outside of the REC's units, the (REC's) container door had to be removed. To maintain a closed system, the outside of the REC units were masking taped. A hot wire anemometer probe could not be mounted inside any of the REC units. A hot wire anemometer needs to be properly orientated to give an accurate measurement (Potter and Wiggert, 2002). The single-wire anemometer senses only the normal component of velocity; if the wire is properly orientated, both the mean and the fluctuations in the mean flow direction can be measured (Potter and Wiggert, 2002). In other words, if the orientation of the flow is unknown, or if the orientation of the hot-wire anemometer can not be accurately determined, then the anemometer will not give an accurate flow velocity measurement. Therefore, due to the unknown air flow orientations inside the REC, the use of a hot wire anemometer is limited.

The aluminium panel above the SYN was removed and covered with cardboard and masking tape. The average air flow velocity was measured above the SYN, between

it and the container walls. The locations are shown in Figure 3-2 and areas in Figure 3-11 on page 3-14. The panels between the master and estimation, and estimation and detection processors were also removed and covered with cardboard and masking tape. However the air flow velocity was only measured between the estimation and the detection processors. The air flow area was measured as 2 x 0.024 x 0.3 = 0.0144 m².

3.1.2. Experimental procedure

The DSP fans and the HPA blower switch on when the radar system is in the standby mode, i.e. not transmitting. The exit velocity at the HPA was measured using an AIR FLOW TA-5 (Bat no.: 315473) hot wire anemometer. The air flow direction was vertical and the hot wire anemometer's probe was orientated accordingly. The system was then switched into transmitting mode. The temperatures of the HPA exit air and inlet air, at the bottom of the REC, were monitored until quasi steady-state was reached. The exit velocity at the HPA was again measured. The measured experimental results are given in Appendix C.2.

The velocity and temperature of the air entering and leaving the area between the estimation and detection processor board was measured using the hot wire anemometer. The location of the velocity of the air entering and leaving area between boards are indicated in Figure 3-3 (b). The air flow direction was assumed to be vertical. Although there were fans 50 mm below the processor heat sinks, the swirl of the air at the entrance could not be removed. The measured experimental results are given in Appendix C.1.

3.1.3. Processed results

The exit air flow area of one of the HPA subunits was measured at 0.01 x 0.37 = 0.0037 m². The average exit velocities for subunit 3 and 7 (Figure 3-2) were 4.29 m/s and 4.13 m/s, resulting in an average of 0.0159 m³/s and 0.015283 m³/s. Taking the average of the aforementioned air flow rates and multiplying by ten, the number of

subunits, the total air flow rate through the HPA was calculated as 0.1559 m³/s. Measurements were taken while the REC was not transmitting. An average entrance velocity of 0.854 m/s (3.1) and exit velocity of 0.951 m/s (3.2) was measured in the area between the estimation and detection processors in the DSP.

$$V_{o,av} = \frac{1}{m}\sum_{n=1}^{m} V_{o,n} = 0.854 \text{ m/s} \tag{3.1}$$

$$V_{i,av} = \frac{1}{m}\sum_{n=1}^{m} V_{i,n} = 0.951 \text{ m/s} \tag{3.2}$$

The average velocity above the SYN, between it and the container wall, was 0.5 m/s on the left and between 0.64 m/s and 0.67 m/s on the right. To get a flow rate, a known area and the average velocity is needed. Due to the complexity of the SYN, it is impossible to experimentally determine the flow rate without drastically altering the REC.

3.2. CFD evaluation of the air flow inside the REC

This section details the CFD evaluation of the air flow inside the REC. The CFD program used is FLOTHERM v6.1. The CFD REC model and other CFD parameter generation processes will be discussed in section 3.2.1. Simulation considerations will be discussed in section 3.2.2. The comparison between the experimental and simulation results will be discussed in section 3.2.3.

3.2.1. CFD REC Model

This section discusses the physical geometry of the REC and the generation of the REC CFD model. Discussion of the physical geometry of the REC units is intended to make the reader aware of the aspects of the units that will affect the air flow through the REC. For this section, please refer to Figure 3-7 and the drawings provided in the data DVD in Appendix A. Note that the units of the REC shown in Figure 3-7 are spaced out. This was done to give the reader a better view of the individual units. Figure 1-4, on page 1-6, shows the true spacing between the units. The units were

created using Autodesk INVENTOR 9 PRO from hard copy assembly drawings. The dimensions used in the INVENTOR drawings were reverse engineered.

The units of the REC will be discussed from bottom to top. The units will be described by the features that influence the air flow through the REC. Also note that the air flow in the REC is, for the most part, in the vertical direction, as indicated by the arrow in the bottom left hand corner of Figure 3-7. The units of the REC are in a container, similar to the container shown in Figure 1-4 on page 1-6.

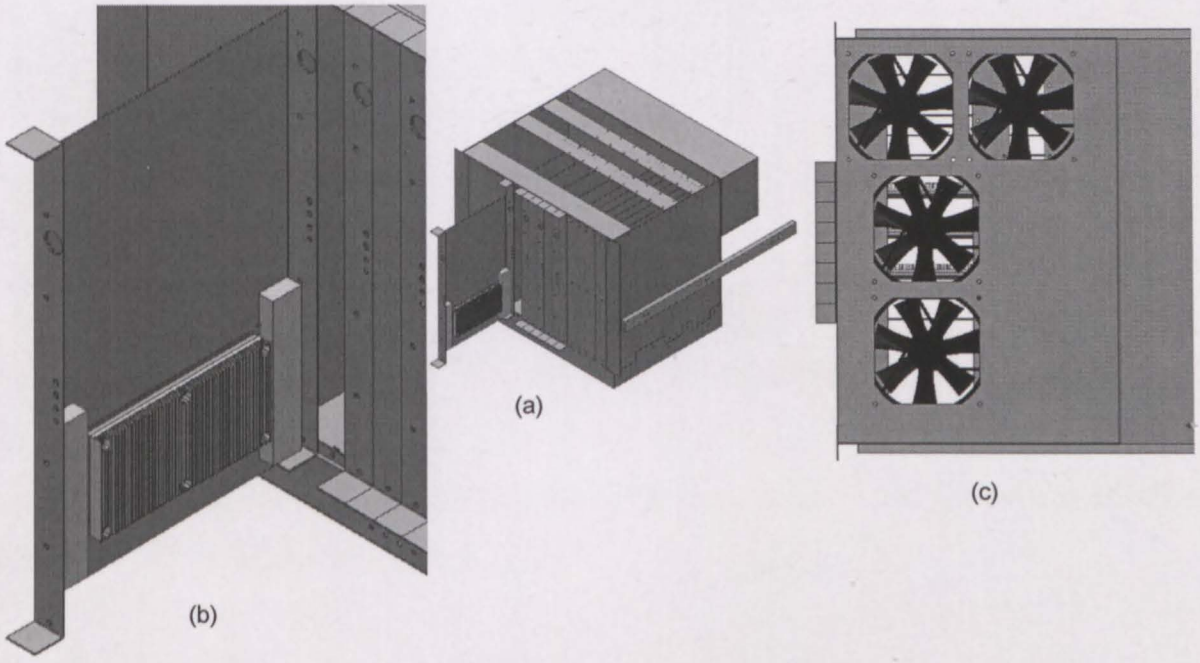

Figure 3-4: An isometric view of DSP (a), with a close up view of the DSP processor heat sinks (b) and a bottom view of the DSP (c), showing the locations of the DSP fans

The PSI has two PCBs that are in a horizontal position directly below the DSP processors. There are four processors in the DSP. The processors are, as shown in Figure 3-7 (c), from right to left the data, master, estimation and detection processors. Heat sinks are used to transfer the heat dissipated by the processors to the air flow through the DSP processor areas. Both of the DSP and the SYN have power supply units at their rears, but were not considered for the CFD simulation.

The SYN has a number of 'blocks' mounted on boards (Figure 3-5 (a)). These boards do not have a large air flow area around them, as shown in Figure 3-5 (c). Note that in Figure 3-7 (c), the SYN has some of the 'blocks' directly above the processors in the DSP. The DA and RFE are for the most part solid in the horizontal direction, as shown in Figure 3-7 (c). There are no significant obstructions to the blower entrance in the HPA.

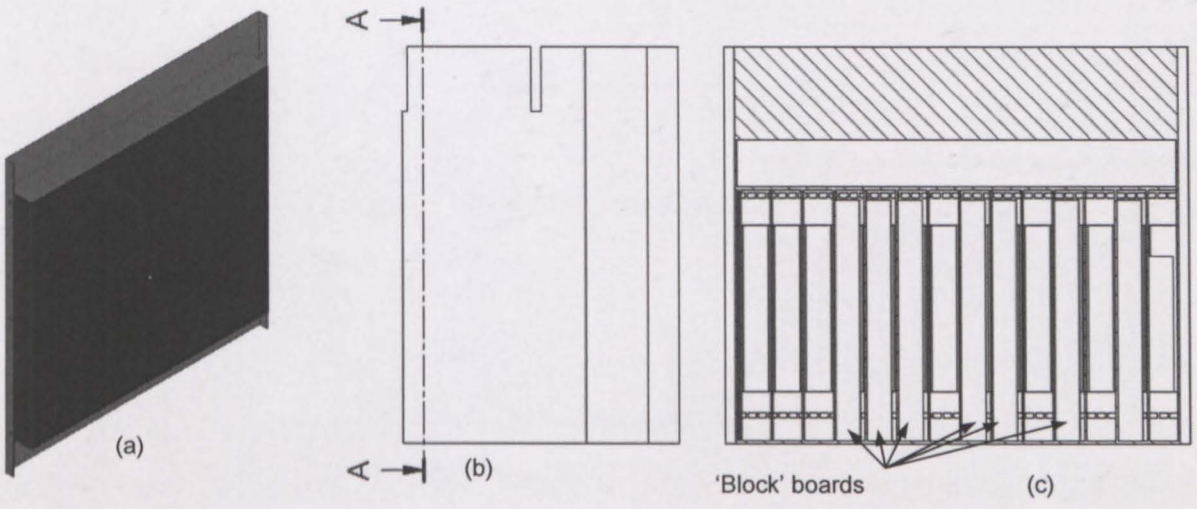

Figure 3-5: SYN 'block' boards (a), the side view of the SYN (b) with a section top view of the SYN (c)

The drawings created in INVENTOR were exported to a SAT file format and then imported into FLOMCAD. The model was simplified by FLOMCAD and then transferred to FLOTHERM. The fins of the DSP were removed and replaced with a FLOTHERM *heat sink* object. A *cuboid* object generating 50 W of energy was placed at the base of each *heat sink*. The heat generating object and *heat sink* were the only objects given material properties, namely aluminium. Since the other objects in the model were not given any material properties, they do not change temperature.

A single fan was placed at the entrance of the HPA with a fixed air flow rate of 0.15 m^3/s. The air flow rate was determined by the experimental analysis of the REC. The HPA at that time did not have a blower enclosure such as on the simplified HPA,

shown in Figure 3-7 (b). The PAPST 4314 G DSP fans were simulated using the 'FLOTHERM' curve in Figure 3-6.

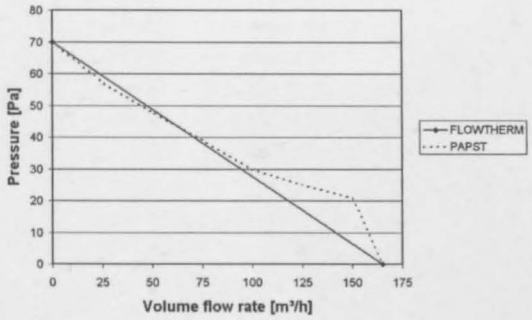

Figure 3-6: Fan curve and simplified fan curve of the PAPST 4314 G fan used in the DSP (Papst, undated).

The current model with 4.5 million cells could not converge. The number of cells were limited by the computer RAM. The HPA was simplified by removing the subunits, as shown in Figure 3-7 (b). The simplified HPA was drawn so that it had a blower enclosure with two exits and entrances. A fixed air flow rate fan (0.075 m^3/s) was placed at the entrance of each blower enclosure. I.e. the total air flow rate through the fans is 0.15 m^3/s. Due to the simplification of the simulation, it can only be evaluated below the entrance of the blower. With the simplification to the HPA, the simulation was able to converge.

The electromagnetic interference (EMI) shield, a more detailed container and cable housing were placed into the model. The EMI shield is below the PSI, in the REC wall. Dimensions of the EMI shield are provided in Appendix C.3. There are cable housings behind the PSI, DSP, RFE and the DA. A cable housing is a metal hinge onto which cables are clamped. It enables a unit to move in and out of the REC with the cables still attached to it. The housing was simulated using two *cuboid*s forming an L-shaped object. There are four vertical *cuboid*s in each corner of the REC, simulating the metal bars which hold together the physical container. The sides of the units are flush with the vertical *cuboid*s, while the units' fronts are on the simulation boundary. The HPA and RFE back faces are also on the simulation boundary.

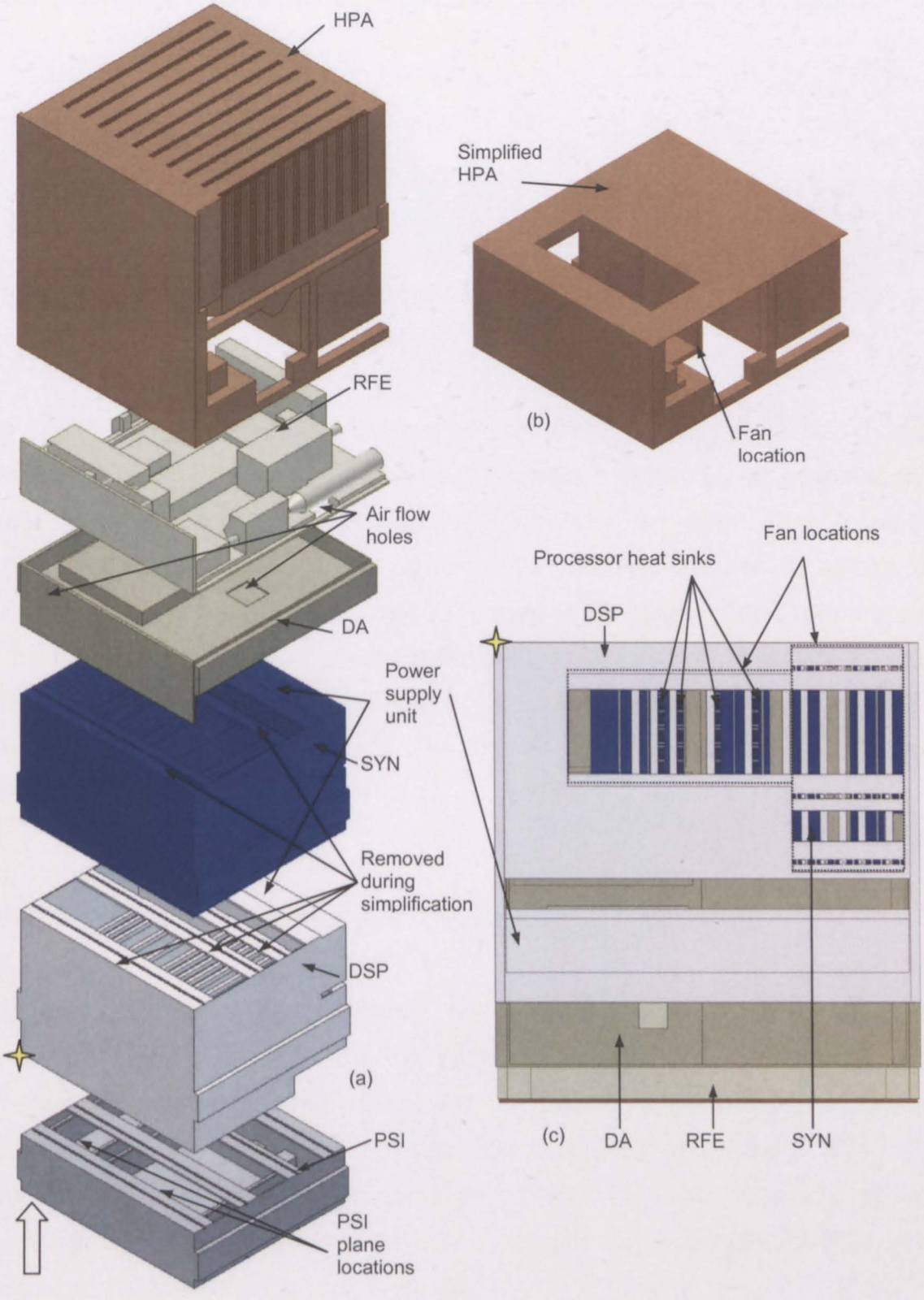

Figure 3-7: Units of the REC shown with spacing increased

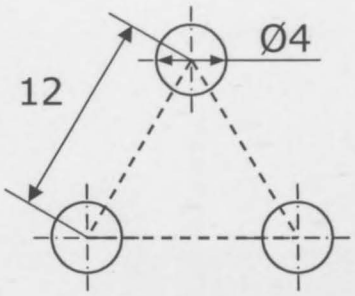

Figure 3-8: EMI shield K_1 base array sketch. EMI shield K_2 uses a 4.3 mm triangle side, instead of the EMI shield K_1's 12 mm

The EMI shield K_1 used in the REC has an array of 12 mm side equilateral triangles with 4 mm holes on the triangles' corners. This mesh can also be called a staggered whole mesh. The EMI pressure loss coefficient was calculated, from a table in Sergent and Krum (1998), as 30. A sketch of the EMI shield, table and calculations are given in Appendix C.3. EMI shield K_2 is used to simulate a shield with a greater air flow area and will therefore offer less resistance to air flow. It is similar to EMI shield K_1 but with 4.3 mm a side triangles. The pressure loss coefficient of the EMI shield K_2 was calculated as K = 0.35. The CFD simulations will be discussed in detail in section 3.3.

3.2.2. Simulation considerations

This section discusses the simulation parameters used for the CFD simulation. Hexahedral cells were used for the simulation, since FLOTHERM cannot use tetrahedral cells. The grid dimensions are specified on a minimum and maximum basis for each axis and not on a volume basis as in STARCD and FLUENT CFD programs. The turbulence model used on FLOTHERM is an automatic scheme, which the user has no input into. The inlet air temperature was set at 35 °C, which is the default air temperature for FLOTHERM.

The number of cells was increased until it was limited by the computer RAM. However, grid independence can be shown from the DSP *heat sink* temperature monitor points, as shown in Figure 3-9 (b).

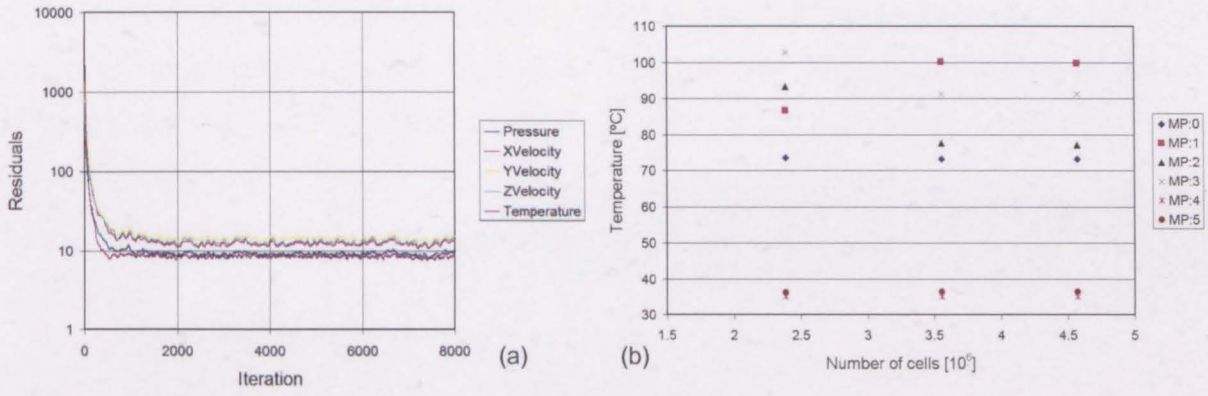

Figure 3-9: Convergence (a) and grid independence (b)

3.2.3. Validation of the CFD results

This section discusses the validation of the CFD the simulation. The CFD datum simulation is compared to experimental data compiled from the experimental analysis documented in section 3.1 on page 3-3. None of the REC units were removed and EMI shield K_1 was used for the datum simulation.

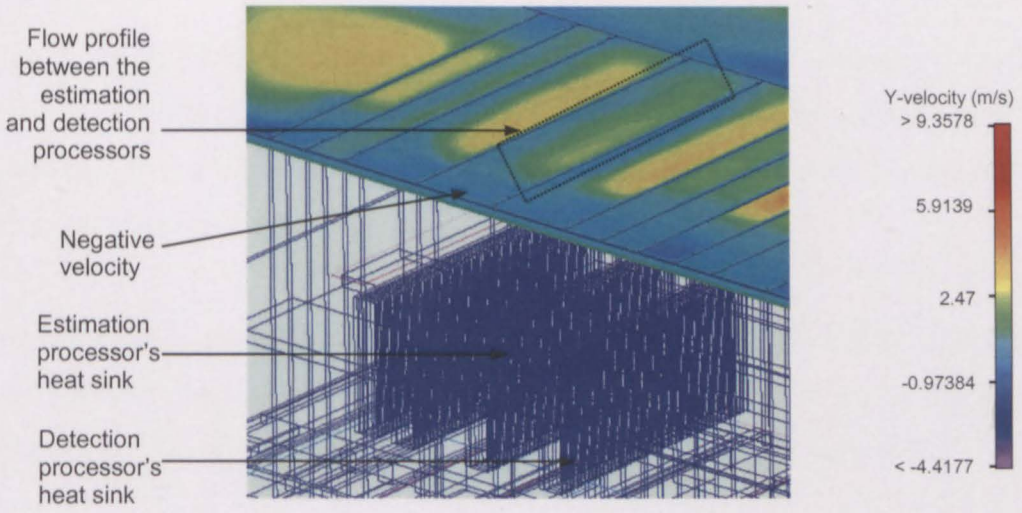

Figure 3-10: Y-velocity profile (total) above 70 mm above the DSP processors.

The velocity values shown in Figure 3-10 are similar to that of the experimental data given in section 3.1.3. However, the negative velocity closer to the front of the DSP was not present in the experimental data. This could be because of the simplification of the model that FLOTHERM did, as discussed in 3.2.1. As shown in Figure 3-7, the holes that are in the DSP and SYN units are used by the board support mechanisms. These holes could prevent the negative velocity present in the simulations.

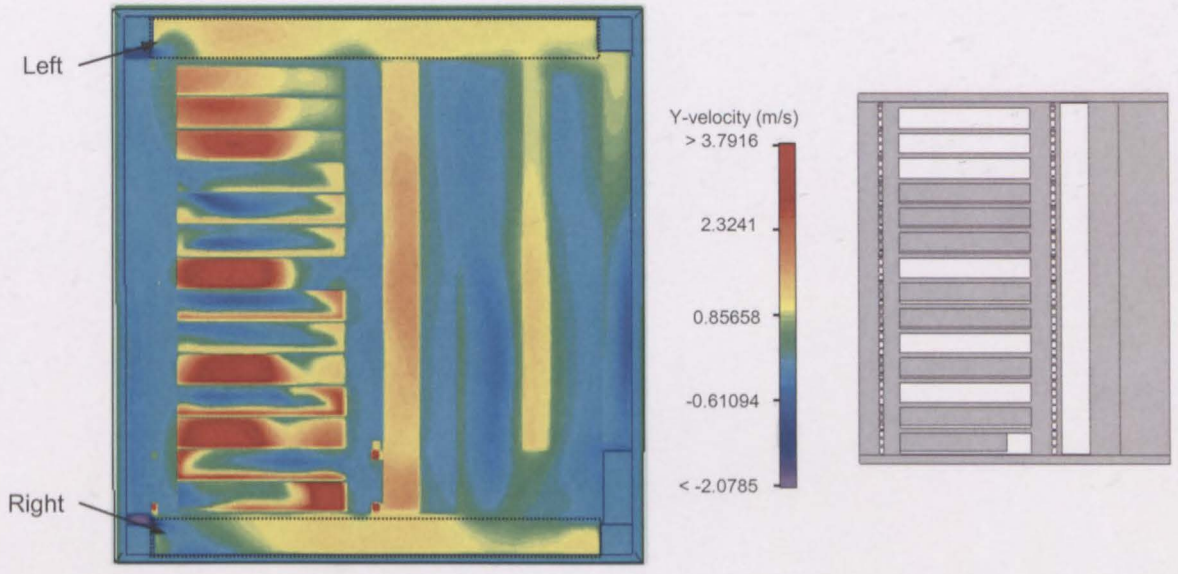

Figure 3-11: Y-velocity profile (auto), for simulation datum, above the SYN with the top view of the SYN shown right.

Above the SYN, a vertical orientation velocity of 0.5 m/s was measured on the left side of the REC, and a vertical orientation velocity of 0.64 m/s to 0.67 m/s on the right hand side. For the CFD simulation, the air flow velocities vary between 1.3 and 0.6 m/s, but average around 0.86 m/s.

There are similarities between the experimental data and the CFD simulation, but it is not a validation of the model. However, due to the complex nature of the REC, the simulation could only be a qualitative evaluation of the air flow in the REC.

3.3. Results and discussion of the CFD simulations for the REC

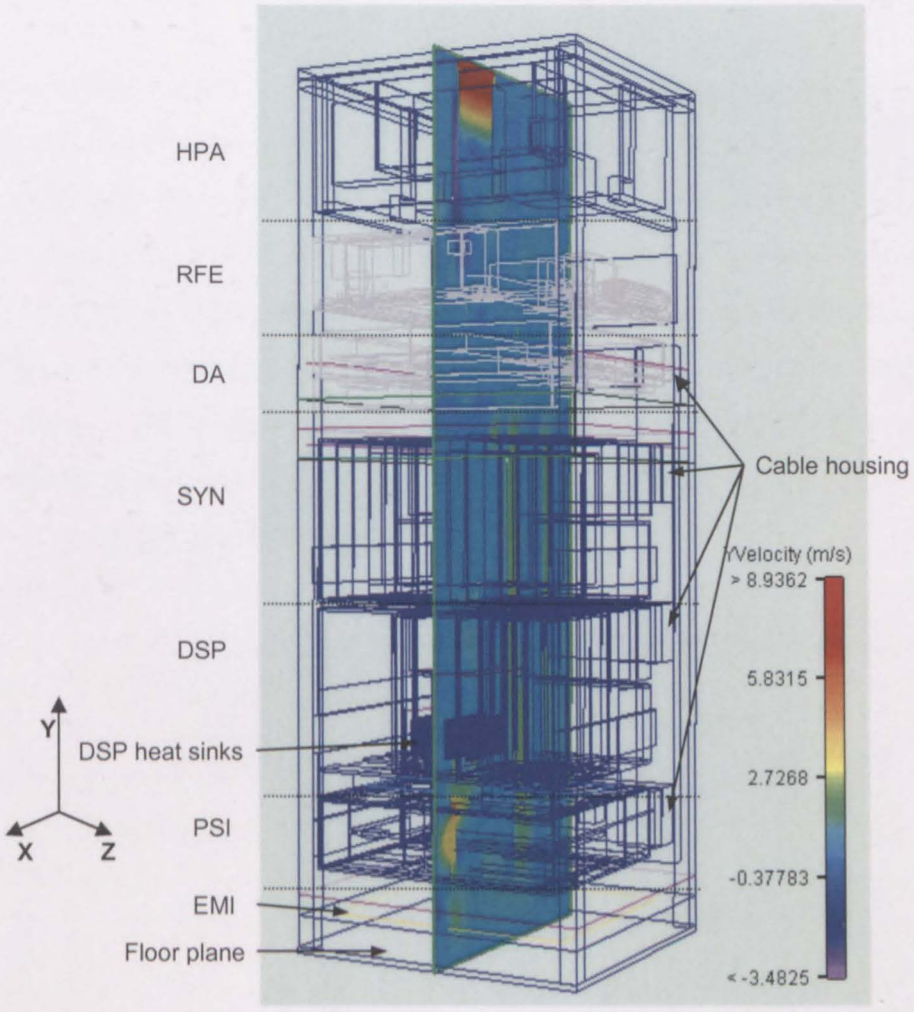

Figure 3-12: 3D wire mesh view of REC with a y-velocity plot shown through the estimation processor

The purpose of the evaluation of the flow inside the REC is to recommend changes to the REC. Changes recommended are to increase the total air flow rate through the REC and to improve the air flow distribution in the REC. Increasing the flow rate will be achieved by increasing the negative pressure at the blower entrance. Note that the blower pressure is negative. An increase in the blower pressure is therefore required. This will decrease the gradient of the system pressure curve and allow the blower to increase the air flow rate. Increasing the total air flow rate will decrease the thermal resistance of the HPA cooling method. The decreased thermal resistance of the HPA cooling method will therefore decrease the transistor mounting base

temperature[1]. Improving the air flow distribution will increase the air flow rate through the DSP processor areas. A reduction of the DSP processor temperature will be achieved and may even result in the redundancy of the DSP fans.

The simulations will be discussed by comparing the average DSP processor heat sink base temperatures and the blower entrance pressure. They will also be compared by discussing the y-velocity and pressures in a sectional plot through the estimation processor. The sectional plot is shown in Figure 3-12 in a REC wire mesh. The wire mesh view can be compared to the solid views of the REC, such as shown in Figure 1-4 on page 1-6. (Files containing more CFD simulations can be found on the data DVD in Appendix A.) The y-velocity plots show the y-direction velocity component of the air flow. Sectional pressure plot uses the maximum and minimum pressure for the current section of the simulation.

Table 3-1: CFD simulation results with HPA present: temperatures

	Processor		Data		Master		Estimation		Detection		
Simulation	Items taken out	EMI shield[2]	$T_{hsb,1}$ [°C]	ΔT (%)	$T_{hsb,2}$ [°C]	ΔT (%)	$T_{hsb,3}$ [°C]	ΔT (%)	$T_{hsb,4}$ [°C]	ΔT (%)	$\Delta T_{hsb,av}$ (%)
Datum		K_1	91.70		77.68		99.89		73.85		
1		K_2	91.49	-0.23	77.70	0.02	99.93	0.04	73.91	0.08	-0.02
2	EMI		91.54	-0.18	77.73	0.05	99.94	0.05	73.95	0.14	0.02
3	PSI	K_1	76.68	-16.38	67.08	-13.65	82.92	-16.99	65.23	-11.67	-14.67
4	PSI	K_2	76.70	-16.36	67.07	-13.66	82.96	-16.95	65.23	-11.67	-14.66
5	DSP fans	K_1	221.4	141.4	165.4	112.9	232.6	132.8	150.0	103.1	122.6
6	DSP fans	K_2	210.5	129.5	147.0	89.17	203.0	103.2	139.6	89.05	102.7
7	DSP fans, PSI	K_1	170.5	85.94	117.5	51.24	196.8	96.98	140.2	89.90	81.01
8	DSP fans, PSI	K_2	171.6	87.10	119.7	54.12	205.7	106.0	149.4	102.3	87.38
9	PSI, RFE, DA	K_1	72.33	-21.12	67.18	-13.52	78.78	-21.13	65.04	-11.93	-16.93

The physical locations of the DSP processors are, from right to left, the data, master, estimation and detection processors, as shown in Figure 3-7 on page 3-11. Table 3-1 shows the DSP processor heat sink base temperatures for different simulations. The

[1] The transistor mounting base temperature is a temperature measured below the transistor in the aluminium on which it is mounted.

[2] The EMI shield K_1 (K = 30) is the original EMI shield, while the EMI shield K_2 (K = 0.35) has a greater flow area, due to the increased hole density.

percentage difference temperatures are relative to the datum simulation temperatures. The percentage difference temperatures give an indication of the change in the air flow rate through the DSP processors area relative to the datum simulation. Table 3-2 shows the blower pressure for each simulation. The greater the pressure difference between a simulation and the datum, the more flow can potentially go through the REC.

The EMI location is indicated in the datum simulation in Figure 3-13 (A). A decrease of 36 % in the blower pressure was noted between simulation-1 and datum. Therefore, when the EMI shield K_1 is removed, as in simulation-1, the blower entrance pressure is reduced by 36 %. When EMI shield K_2 is used in simulation-2, the blower entrance pressure is also reduced by 36 %.

Table 3-2: CFD simulation results with HPA present: pressure

			Blower entrance pressure	
Simulation	Items taken out	EMI shield	P_{min} [Pa]	ΔP (%)
Datum		K_1	-49.2	
1		K_2	-31.4	-36.3
2	EMI		-31.2	-36.6
3	PSI	K_1	-46.9	-4.8
4	PSI	K_2	-29.2	-40.7
5	DSP fans	K_1	-51.7	5.0
6	DSP fans	K_2	-33.2	-32.6
7	DSP fans, PSI	K_1	-47.9	-2.8
8	DSP fans, PSI	K_2	-30.2	-38.7
9	PSI, RFE, DA	K_1	-24.5	-50.3

The sectional pressure plot for the datum simulation, Figure 3-13 (A), shows that there are significant pressure drops over the RFE (a) and DA (b). It also shows a significant pressure drop above the horizontal PCB boards in the PSI. The pressure drop corresponds to the features of the units as discussed in section 3.2.1 on page 3-7. It was stated in section 3.2.1 that the RFE and DA are basically a solid in the horizontal plane and that there are horizontal PCB boards in the PSI below the DSP processors. The DSP fans cause the pressure rise from (c) to (d). The figure also shows that the pressure at (e) is a lower than at (d). This corresponds to the negative y-velocity at (f) and also the significant velocity at (g). This shows that the SYN

causes some of the air to go in the negative y-direction. There are significant air flows behind the DSP processors and behind the DSP and SYN themselves (g). There is a high y-velocity region through the PSI (h) caused by the DSP fans, which corresponds to the high pressure drop at (c).

Removing the PSI in simulation-4, as shown in Figure 3-13 (C), still results in a pressure drop above the RFE (i) and DA (j). However, there is no significant pressure drop below the DSP, since the PSI has been removed (k). There is still a pressure rise above the DSP processors (l), while there is a lower pressure behind the DSP processors. There is also a pressure drop at (m), which corresponds to the negative y-velocity, at Figure 3-14 (a). The significant velocities behind the DSP processors, behind the SYN blocks, behind the DSP and SYN themselves are still present at (b).

Removing the PSI removes an air flow resistance to the DSP fans. This results in a 14 % decrease in temperature, irrespective of the EMI shield. The blower pressure was also reduced, but the magnitude depends on the EMI shield.

In simulations with the DSP fans still present, there was a pressure difference between the DSP processor area and the area directly behind it. However due to their removal in simulation-6, shown in Figure 3-14, there was no pressure difference at (c) and no pressure drop above the PSI (d). This means that the flow rate has been changed and results in an average increase of 102 % in DSP processor heat sink temperatures. The temperature rise is also dependent on the EMI shield. There are still pressure drops above the RFE (e) and DA (f).

The significant air flow behind the DSP processors area, behind the DSP and SYN themselves is still present (g). The high y-velocity present in the PSI in Figure 3-13 (h) is less in simulation-6, Figure 3-14 (h). This shows that it is easier for the flow to go around the DSP than through it. The increase in the temperature also relates to the physical REC behaviour (Graham, 2007). Graham (2007) stated that when the DSP fans were switched off, there was an increase in the DSP processor temperatures. As a result, the DSP fans switched on automatically when the REC is in standby mode.

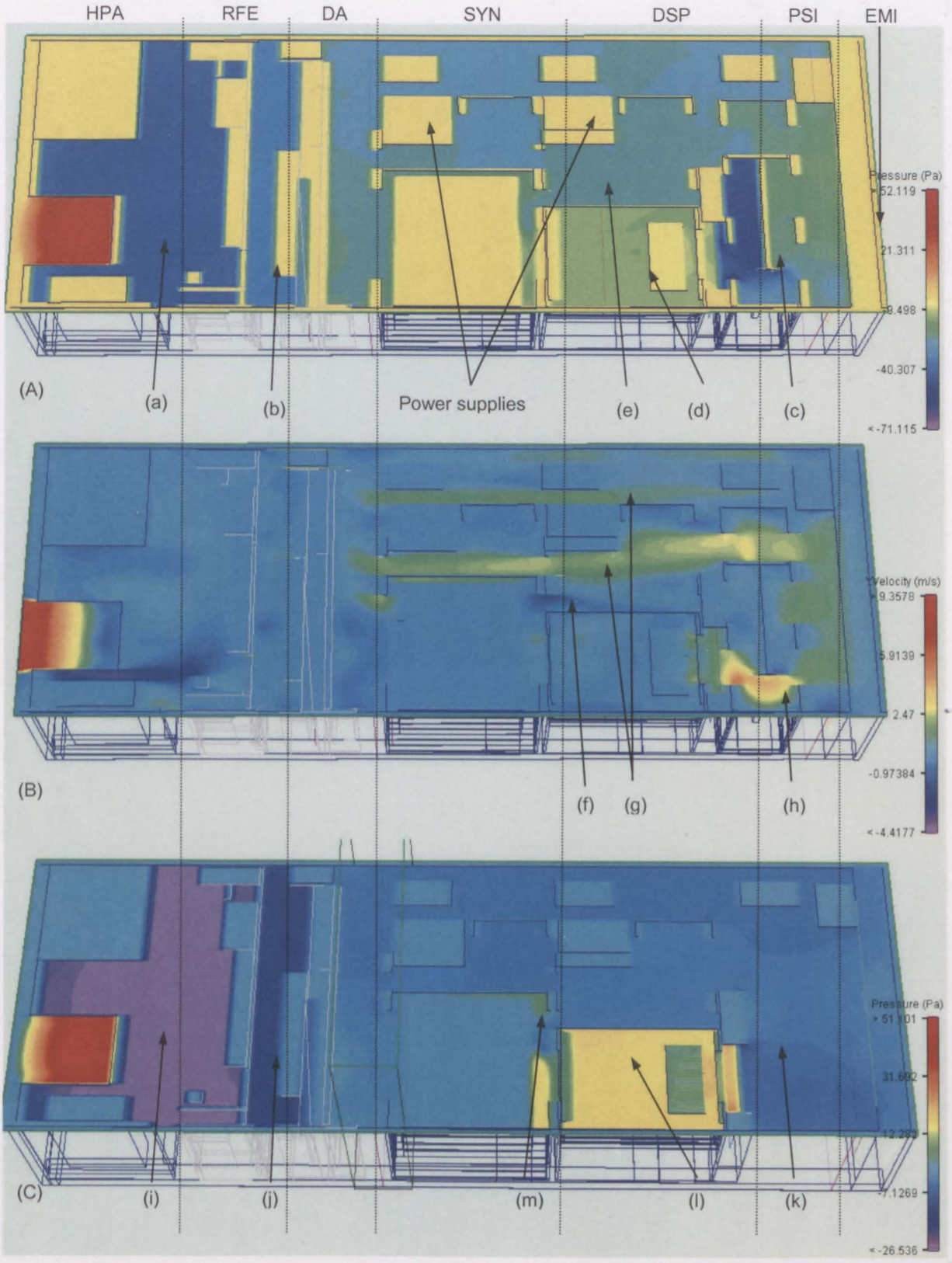

Figure 3-13: Sectional pressure (A) and y-velocity (B) plots in REC for simulation datum. Also shown is the sectional pressure (C) plot for simulation-4.

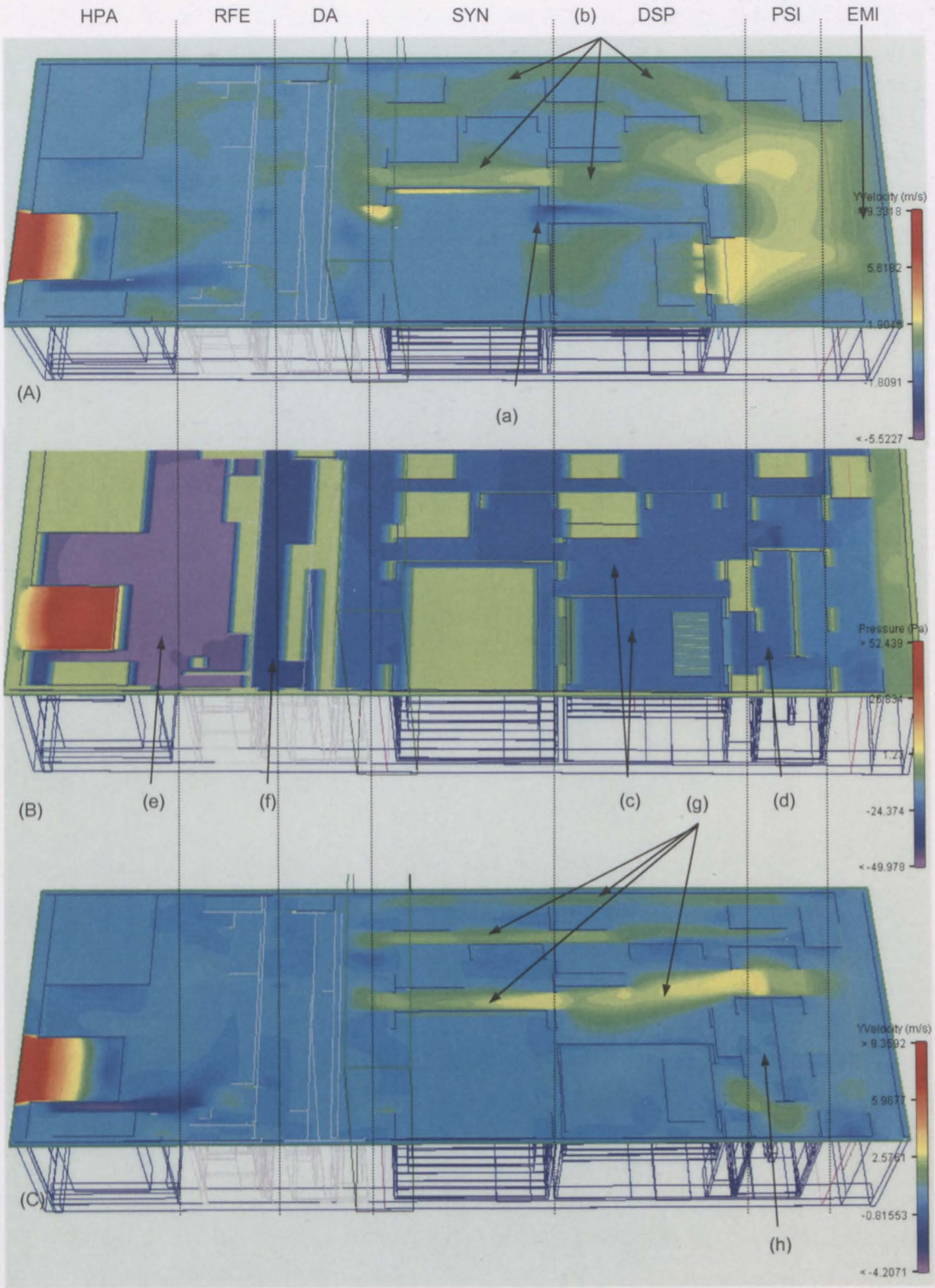

Figure 3-14: Y-velocity (A) plot for simulation-4. Also shown are the sectional pressure (B) and y-velocity (C) plots in REC for simulation-6.

When the PSI was removed there was, on average, a 40 % decrease in the DSP processor temperatures for simulations that did not have the DSP fans compared to the simulations that did have the DSP fans. This is another indication that the PSI hinders the air flow into the DSP processor areas.

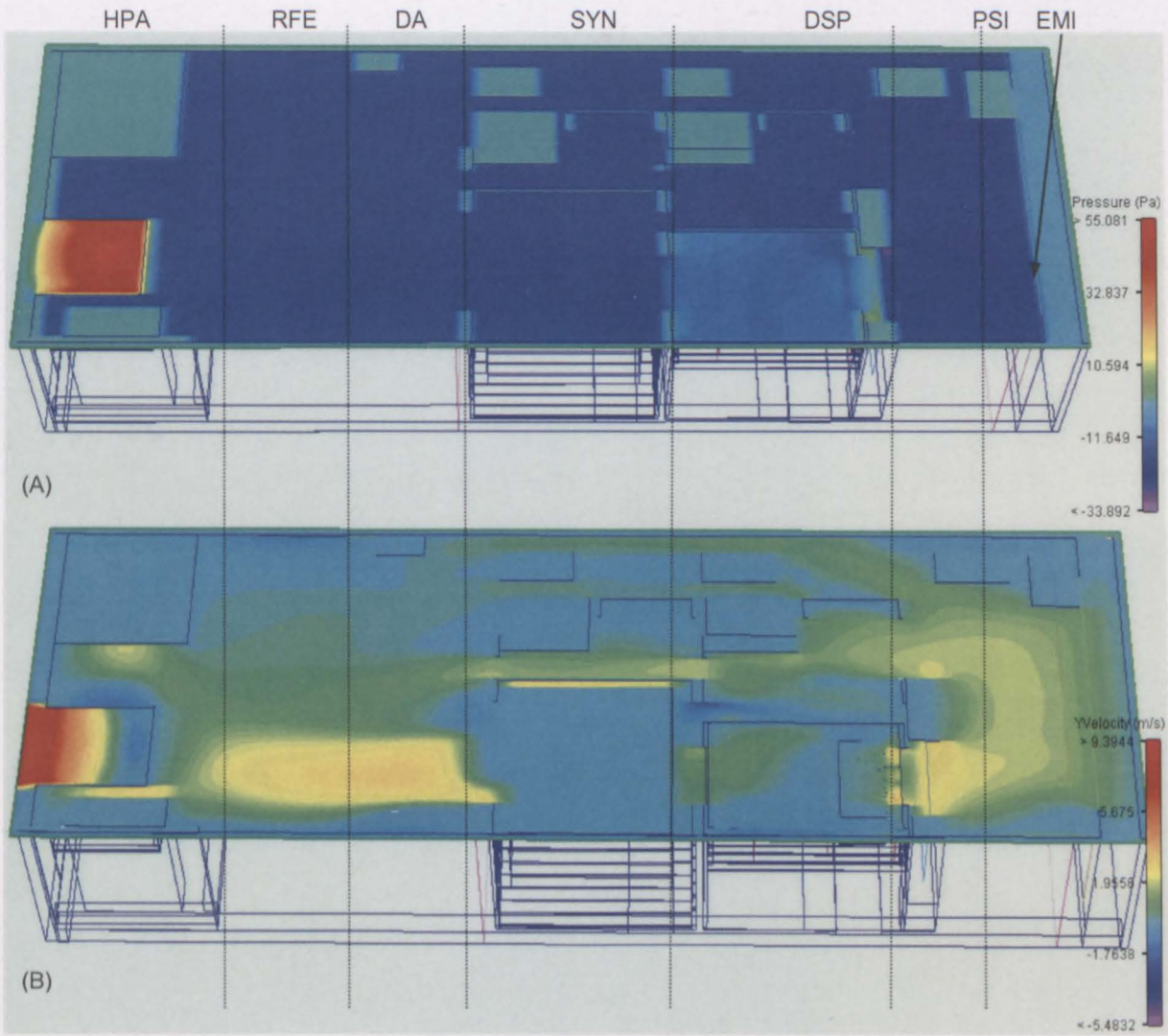

Figure 3-15: Sectional pressure (A) and y-velocity (B) plots for simulation-8.

As stated in the description on the REC units, the RFE and DA are basically solid. When they were removed, there was a significant temperature drop in the DSP processor heat sinks. Figure 3-15 shows only a pressure rise in the DSP processor area, while the rest of REC is at a similar pressure. This then shows that the RFE and DA negatively influence the flow path in the REC. There was also a 50 % drop in

the blower pressure. This will result in an increase of the air flow through the HPA's blower. This would further decrease the temperature in the DSP processor heat sinks. Note that the simulation was done the EMI shield K_1. Using the EMI shield K_2, would result in a further decrease of the blower pressure.

Table 3-3: CFD simulation results without the HPA present

	Processor		Data		Master		Estimation		Detection		
Simulation	Items taken out	EMI shield	$T_{hsb,1}$ [°C]	ΔT (%)	$T_{hsb,2}$ [°C]	ΔT (%)	$T_{hsb,3}$ [°C]	ΔT (%)	$T_{hsb,4}$ [°C]	ΔT (%)	$\Delta T_{hsb,av}$ (%)
Datum		K_1	91.70		77.68		99.89		73.85		
10	HPA	K_1	96.55	5.28	81.52	4.94	104.8	4.89	78.84	6.75	5.46
11	HPA	K_2	95.68	4.33	80.93	4.17	103.8	3.87	78.07	5.72	4.52
12	HPA, PSI	K_1	83.83	-8.59	72.64	-6.50	87.44	-12.46	68.03	-7.89	-8.86
13	HPA, PSI	K_2	82.51	-10.0	71.69	-7.72	86.24	-13.66	66.70	-9.68	-10.27
14	HPA, RFE, PSI, DA	K_1	73.87	-19.4	69.20	-10.9	80.64	-19.27	65.60	-11.17	-15.20
15	HPA, RFE, PSI, DA	K_2	73.00	-20.4	68.31	-12.1	80.22	-19.68	65.35	-11.50	-15.91

Of interest to the project is the evaluation of the air flow inside the REC when the HPA has been removed. When the HPA is present, it dominates the air flow inside the REC. This can be seen in the lack of recirculation (negative y-velocity) in Figure 3-13, Figure 3-14 and Figure 3-15. In Figure 3-16, the HPA has been removed (a). The particle tracks show the paths that particles would take if they originated at the EMI shield. The particles at (b) show that some of the air can get through the DA but not through the RFE.

Note that there is still a pressure drop above the PCB PSI boards (c) and a pressure rise above the DSP fans (d). The particles at (e) are moving in the negative y-direction, i.e. they are circulating in the REC. This can be shown to be so by the negative y-velocity at (f). There are also very high y-velocities at (g), where the air flow has to go through the PSI.

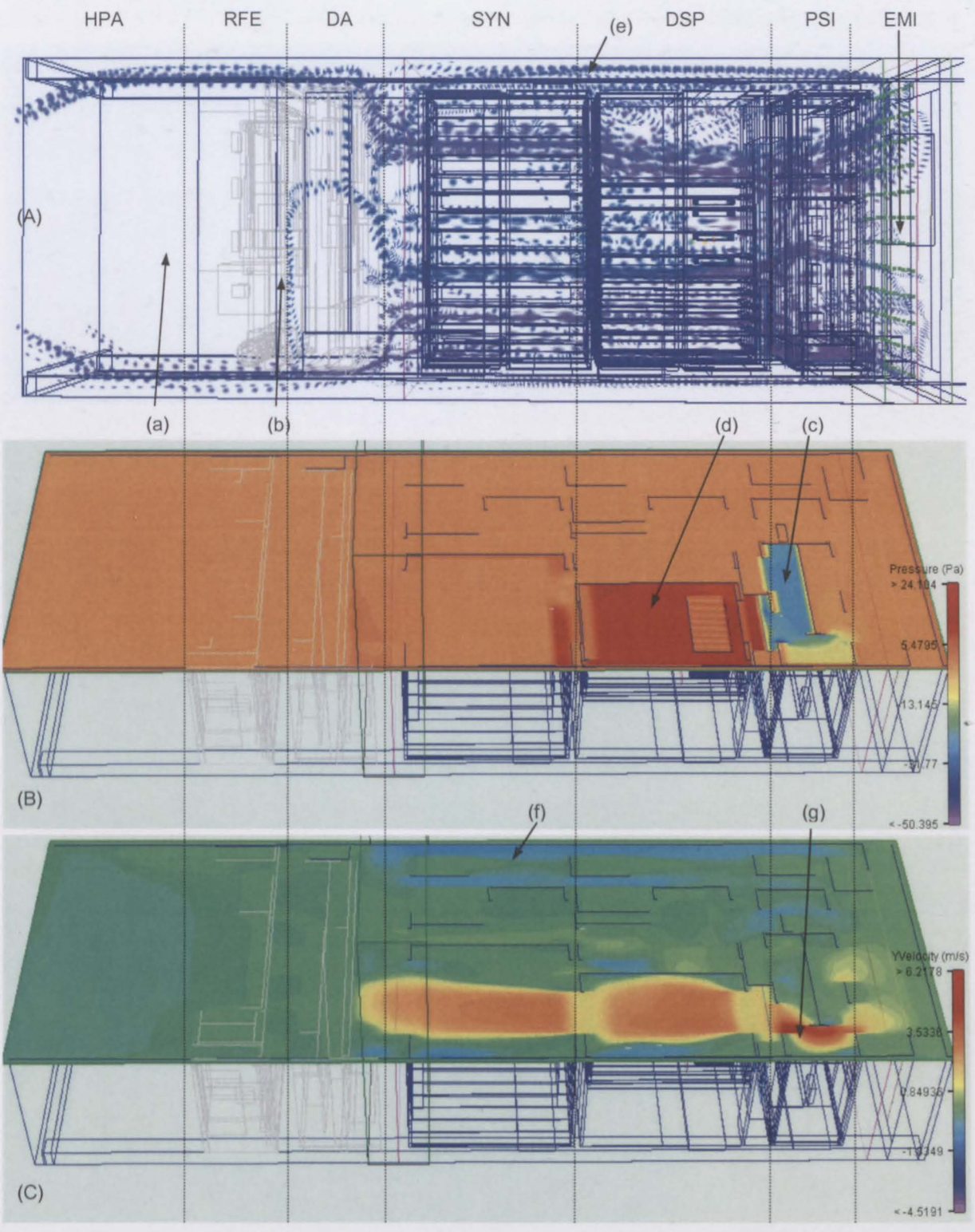

Figure 3-16: EMI shield particle track (A), sectional pressure (B) and y-velocity (C) plots for simulation-11.

In conclusion, removing the HPA removes the dominating air flow object of the previous simulations. The only objects which can provide an air flow, and therefore

also dictate where the air flow will go, are the DSP fans. The RFE and DA provide a flow resistance and the air flow then circulates to below the PSI. There are no significant temperature differences between simulations with EMI shield K_1 and K_2. This indicates that the flow rates through the DSP processors are similar, though the air flow rate through the EMI shield differs.

3.4. Original HPA cooling solution design

From the thermal problems and the CSLD analysis discussed in the introduction of Chapter 3, an analysis of the HPA cooling solution is to be done. The original HPA cooling solution consisted of an aluminium block machined hollow as shown in Figure 3-17 (a). Fins were sintered onto the outside of the 8mm side of the case. Six transistors are bolted to the case on the other side of the fins. The transistors are not the only items in the subunit, as shown in Figure 3-17 (b) and Figure 3-18 (b). The heat dissipated by the transistors are spread through the case where the fins transfer the heat to air flow.

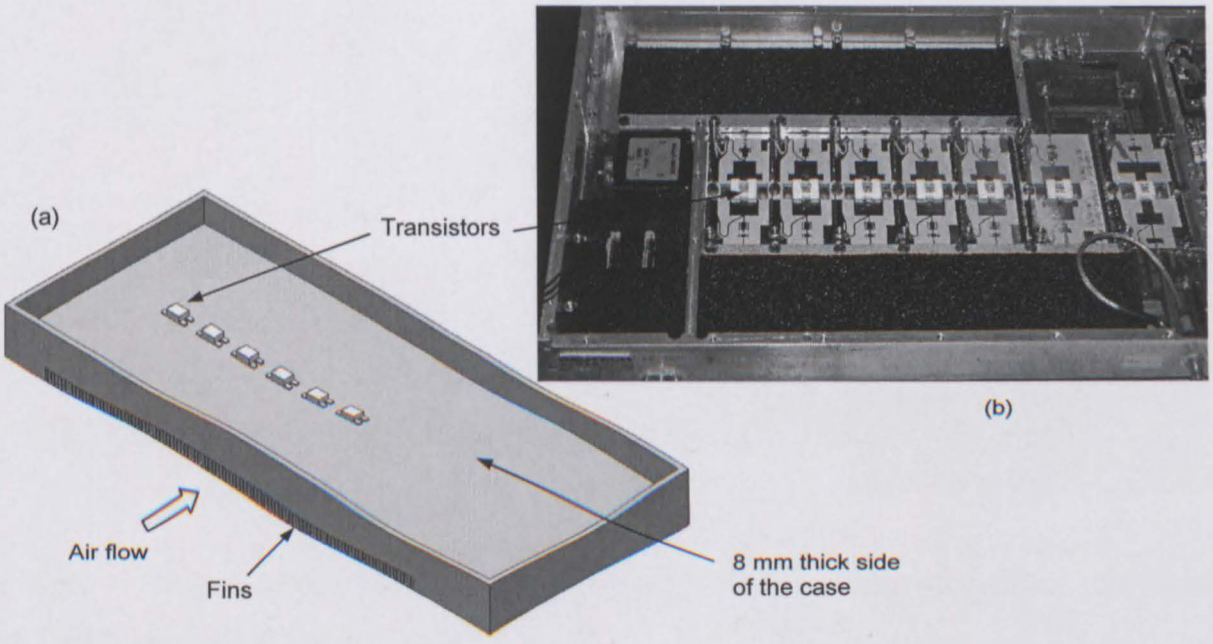

Figure 3-17: Sketch of the original HPA cooling solution design (a). Internal layout of the HPA subunit (b).

A subunit bench test is used to provide data for a numerical model of the HPA subunit. The numerical model will estimate transistor mounting base temperatures from the aluminium plate temperatures at the transistors.

3.4.1. Subunit bench test

This section details the experimental set up, procedure and results of a HPA subunit bench test. The external case, inlet and exit air temperatures were measured as well as the power input to the subunit. The power and heat dissipation in the subunit is listed below.

1. 488 W input power to the subunit at 80 V.
2. 400 W from the power supply units in the subunit at 300 V.
3. 80 W RF power leaves the subunit.
4. 320 W is dissipated in heat energy.

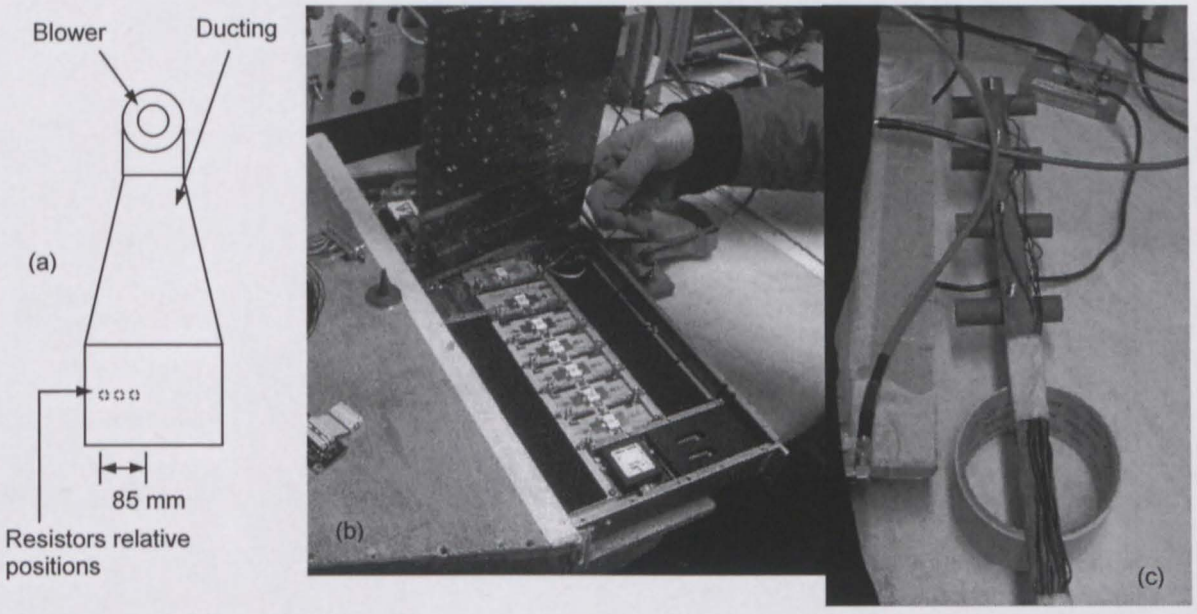

Figure 3-18: Subunit bench test schematic (a), resistor locations (b) and radiation shielded thermocouples (c).

The experimental set up consisted of a wood ducting onto which the subunit was attached. A blower was mounted on the other end of the ducting. Masking tape was

used to try and seal the ducting, but this was unsuccessful. The flow rate was measured at the subunit exit, since the inlet flow rate could not be guaranteed to be the exit flow rate. The inlet air temperature was measured at the inlet of the blower. The case temperature was measured on 85 mm from the start of the fins, as shown in Figure 3-19.

At the exit of the subunit, nodes were marked off and then their displacement, from where the fins start, measured. The air flow velocity and the temperature were measured at these nodes. In turn the mass flow rate and the energy gained by the air were calculated from the flow velocities, temperatures and displacements. A hot wire anemometer (Airflow TA-5, bat no.: 315473) was used to measure the air flow velocity, while radiation shielded t-type thermocouples were used to measure the inlet and exit air temperatures, as show in Figure 3-18 (c). Once the subunit had been switched on, temperatures were recorded until quasi steady-state was reached. The inlet air temperature was taken as the reference temperature.

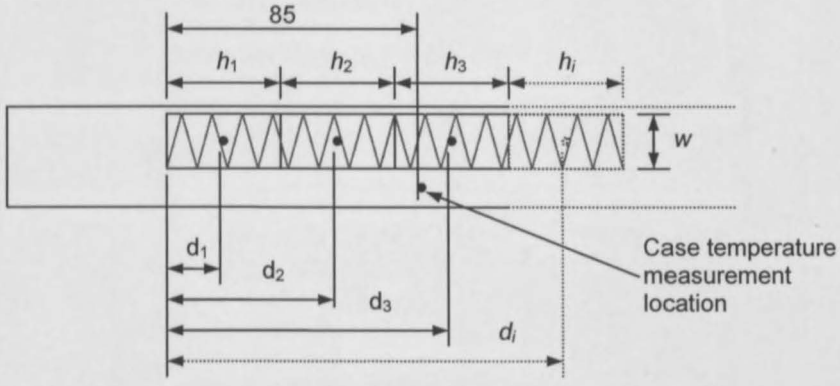

Figure 3-19: HPA subunit air flow cell and node

The shared border between two cells is halfway in between the cells. The height of each cell, h_n, can then be calculated from the node displacement measurements. The cell area, A_n, can be calculated from the height, h_n, and the width, w using equation (3.3). Equation (3.4) is used to calculate the mass flow rate for a cell, $\dot{m}_n$, is calculated from the product of the air density, average velocity and area of the cell. By applying energy balance to the flow through the subunit, and assuming the flow

does not mix in the fins, the energy gained by the air is calculated using equation (3.5).

$$A_n = h_n \times w \tag{3.3}$$

$$\dot{m}_n = \rho \dot{G}_n = \rho V_{av,n} A_n \tag{3.4}$$

$$\dot{Q}_n = \dot{m}_n c_{p,av} \left(T_{m,o,n} - T_{m,i} \right) \tag{3.5}$$

The total energy gained by the air is the sum of the energy gained by the air for each individual cell, equation (3.6). Equations (3.3) to (3.6) were applied to the measured data. The result is that the total energy gained by the air is $\dot{Q}_t$ = 286.03 W, which is 10 % less than the heat dissipated ($\dot{Q}_{hd}$ = 320 W), as calculated using equation (3.7). The measured and processed data is provided in Appendix D.

$$\dot{Q}_t = \sum_{n=1}^{m} \dot{Q}_n \tag{3.6}$$

$$\begin{aligned} \Delta\dot{Q} &= 100 \times \left(\dot{Q}_{hd} - \dot{Q}_t \right) / \dot{Q}_{hd} \\ &= 100 \times (320 - 286.03) / 320 \\ &= 10.62\ \% \end{aligned} \tag{3.7}$$

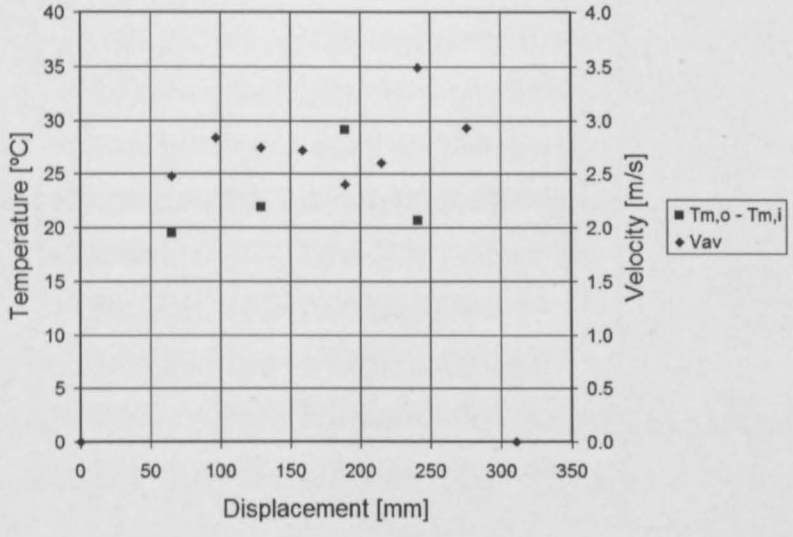

Figure 3-20: Velocity and relative temperature displacement for the high power amplifier subunit test

The rise in the temperature at around 200 mm displacement, in Figure 3-20, coincides with local velocity drop. When the fins were examined, it was found that they were damaged at around 200 mm displacement. The case temperature measured was 49.7 °C at an inlet temperature of 15.7 °C.

3.4.2. Numerical model

The numerical model of the subunit is used to estimate the aluminium plate temperatures at the transistor locations. The model was coded in MATLAB and is provided in the data DVD in Appendix A. The model assumes that there is no mixing of the air flow as it moves over the plate, uniform heat transfer rate from the plate to the air, constant material properties and uniform velocity distribution.

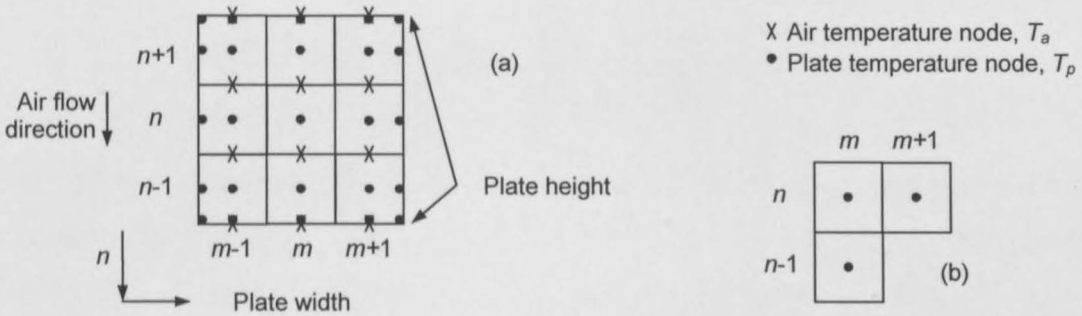

Figure 3-21: Sketch of internal nodes (a) and top left corner node (b) for the subunit numerical model

For an internal node, using the nodes shown in Figure 3-21 (a), applying steady-state energy balance, equation (3.9) to the internal node, gives equation (3.8).

$$\dot{E}_{in} + \dot{E}_{out} = 0 \tag{3.8}$$

$$\sum_{i=1}^{4} \dot{Q}_{(i)\to(m,n)} + \dot{E}_g + \dot{Q}_{c(m,n)\to(m,n)} = 0 \tag{3.9}$$

where i refers to the neighbouring nodes, $\dot{Q}_{(i)\to(m,n)}$ is the conduction between nodes, $\dot{E}_g$ is the energy generated in a specific node, while $\dot{Q}_{c(m,n)\to(m,n)}$ is the convection from a node to the air. The aforementioned terms are expressed using equations

(3.10) to (3.15). The conduction heat transfer between the nodes is given by equations (3.10) to (3.13). The discretetion of Fourier's law, or conduction heat transfer, is shown in Appendix C.4. The node size is Δx by Δx and Δz high. The average air temperature is assumed to be the linear average of the air temperature entering and leaving the node in equation (3.15).

$$\dot{Q}_{(m-1,n)\to(m,n)} = k(\Delta x \Delta z)\frac{T_{p(m-1,n)} - T_{p(m,n)}}{\Delta x} \tag{3.10}$$

$$\dot{Q}_{(m,n-1)\to(m,n)} = k(\Delta x \Delta z)\frac{T_{p(m,n-1)} - T_{p(m,n)}}{\Delta x} \tag{3.11}$$

$$\dot{Q}_{(m+1,n)\to(m,n)} = k(\Delta x \Delta z)\frac{T_{p(m+1,n)} - T_{p(m,n)}}{\Delta x} \tag{3.12}$$

$$\dot{Q}_{(m,n+1)\to(m,n)} = k(\Delta x \Delta z)\frac{T_{p(m,n+1)} - T_{p(m,n)}}{\Delta x} \tag{3.13}$$

$$\dot{E}_g = \dot{Q}'''_{(m,n)}(\Delta x \Delta x \Delta z) \tag{3.14}$$

$$\dot{Q}_{c(m,n)\to(m,n)} = h_{av}\left(\left[T_{a(m-1,n-1)} - T_{a(m-1,n)}\right]/2 - T_{p(m,n)}\right) \tag{3.15}$$

Substituting equations (3.10) to (3.15) into equation (3.9) gives equation (3.16). Rearranging equation (3.16) gives equation (3.17). Replacing the constants in equation (3.17) with the variables α, β, γ, δ and ζ gives equation (3.18).

$$\begin{aligned} &k\Delta z\left(T_{p(m-1,n)} + T_{p(m,n-1)} + T_{p(m+1,n)} + T_{p(m,n+1)} - 4T_{p(m,n)}\right) + \dot{Q}'''_{(m,n)}\left(\Delta x^2 \Delta z\right) \\ &+h_{av}\Delta x^2\left(\left[T_{a(m-1,n-1)} - T_{a(m-1,n)}\right]/2 - T_{p(m,n)}\right) = 0 \end{aligned} \tag{3.16}$$

$$\begin{aligned} &k\Delta z\left(T_{p(m-1,n)} + T_{p(m,n-1)} + T_{p(m+1,n)} + T_{p(m,n+1)}\right) + \dot{Q}'''_{(m,n)}\left(\Delta x^2 \Delta z\right) \\ &+0.5h_{av}\Delta x^2\left(T_{a(m-1,n-1)} - T_{a(m-1,n)}\right) = (4k\Delta z + h_{av}\Delta x^2)T_{p(m,n)} \end{aligned} \tag{3.17}$$

$$\begin{aligned} &k\Delta z\left(\alpha T_{p(m-1,n)} + \beta T_{p(m,n-1)} + \gamma T_{p(m+1,n)} + \delta T_{p(m,n+1)}\right) + \dot{Q}'''_{(m,n)}\left(\Delta x^2 \Delta z\right) \\ &+0.5h_{av}\Delta x^2\left(T_{a(m-1,n-1)} - T_{a(m-1,n)}\right) = (\zeta k\Delta z + h_{av}\Delta x^2)T_{p(m,n)} \end{aligned} \tag{3.18}$$

where α, β, γ, δ are equal to 1 while ζ is equal to 4.

Applying the energy balance equation (3.9) to the top left corner node, using the nodes shown in Figure 3-21 (b), gives equation (3.19). Replacing the constants in equation (3.19) with the variables α, β, γ, δ and ζ gives equation (3.20)

$$k\Delta z\left(T_{p(m,n-1)}+T_{p(m+1,n)}\right)+\dot{Q}'''_{(m,n)}\left(\Delta x^2\Delta z\right)+0.5h_{av}\Delta x^2\left(T_{a(m-1,n-1)}-T_{a(m-1,n)}\right)$$
$$=(2k\Delta z+h_{av}\Delta x^2)T_{m,n} \tag{3.19}$$

$$k\Delta z\left(\alpha T_{p(m-1,n)}+\beta T_{p(m,n-1)}+\gamma T_{p(m+1,n)}+\delta T_{p(m,n+1)}\right)+\dot{Q}'''_{(m,n)}\left(\Delta x^2\Delta z\right)$$
$$+0.5h_{av}\Delta x^2\left(T_{a(m-1,n-1)}-T_{a(m-1,n)}\right)=(\zeta k\Delta z+h_{av}\Delta x^2)T_{p(m,n)} \tag{3.20}$$

where β and γ are equal to 1, while α and δ are equal to 0. The constant ζ is equal to 2. The variables for the other corner and side nodes can be similarly generated and are given in Table 3-4.

Table 3-4: Subunit numerical model node variables

	Variable				
Node position	α	β	γ	δ	ζ
Right	1	0	1	1	3
Right, Top	1	0	1	0	2
Right, Bottom	1	0	0	1	2
Left	0	1	1	1	3
Left, Top	0	1	1	0	2
Left, Bottom	0	1	0	1	2
Internal	1	1	1	1	4

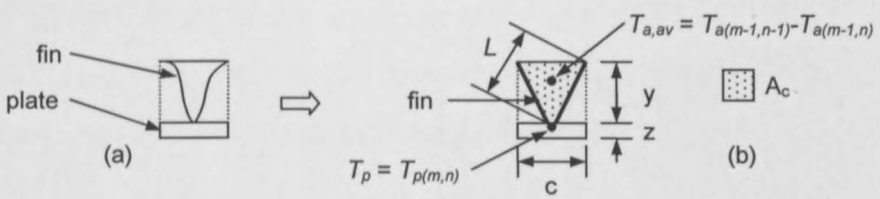

Figure 3-22: Original HPA cooling solution fin simplification and fin parameters.

The average heat transfer coefficient, h_{av}, for the heat transfer from the plate to the air in equations (3.18) and (3.20) is calculated from the equations that follow. The heat transfer coefficient is calculated for the triangular channel shown by the dotted area A_c in Figure 3-22. The width of the channel is c, while the height is y. The flow area of the channel is calculated using equation (3.21). The length of the fin is l and is calculated using Pythagoras in equation (3.22). The flow in the channel G_c is

based on the fraction of the channel area over the total flow area, A_t (equation 3.23), in equation (3.24). The parameters are: c = 5.5 mm, y = 13 mm, t = 0.1 mm, z = 8 mm, w_p = 310 mm, G_t = 0.0111 m³/s.

$$A_c = 0.5cy \tag{3.21}$$

$$L = \sqrt{(c/2)^2 + y^2} \tag{3.22}$$

$$A_t = w_p y \tag{3.23}$$

$$\dot{G}_c = \dot{G}_t A_c / A_t \tag{3.24}$$

The perimeter, P_c (equation 3.25), is used to calculate the hydraulic diameter of the channel D_{hc} (equation 3.26). The channel Reynolds number, $\mathrm{Re}_{D_{hc}}$ (equation 3.28), is calculated using the velocity of the air flow in the channel, V_c (equation 3.27).

$$P_c = c + 2l \tag{3.25}$$

$$D_{hc} = 4A_c / P_c \tag{3.26}$$

$$V_c = G_c / D_{hc} \tag{3.27}$$

$$\mathrm{Re}_{D_{hc}} = \rho V_c D_{hc} / \mu \tag{3.28}$$

The characteristic length of the fin, L_c (Incropera and DeWitt, 2002) (equation 3.29), is used to calculate the thermal efficiency of the fin, η, in equation (3.31), which also uses the term mL_c. mL_c is calculated in equation (3.30).

$$L_c = L + t/2 \tag{3.29}$$

$$mL_c = (2h / kA_p)^{1/2} L_c^{3/2} \tag{3.30}$$

$$\eta = \tanh(mL_c) / mL_c \tag{3.31}$$

Since the flow in the channel is laminar ($\mathrm{Re}_{D_{hc}}$ = 6.05), a Nusselt number is selected and used to calculate the heat transfer coefficient for the channel, h. The Nusselt number is selected such that the node closest to the experimental case temperature measurement location is equal to the experimental case temperature.

$$h = Nuk / D_{hc} \tag{3.32}$$

To calculate the average heat transfer coefficient, the heat transfer rate from the node to the air is calculated from the surface heat transfer coefficient (hc^2 term) and from the fins. The heat transfer from one side of the fin is the ηhLc term in equation (3.33). It is multiplied by 2 since the heat transfer is from both sides of the fins. And multiplied again by 2 since there are 2 fins in the area being used. Equation (3.33) is simplified to equation (3.34), which is used in the MATLAB code.

$$h_{av} = \left[hc^2 + 2(2\eta hLc)\right]/c^2 \tag{3.33}$$

$$h_{av} = h(c^2 + 4\eta Lc)/c^2 \tag{3.34}$$

Equation (3.18) and Table 3-4 are applied to each node in the mesh in an iterative method. The iteration is stopped when steady-state plate and air node temperatures have been achieved. The nodes on the edge of the mesh are made equal to the edge nodes temperatures, when the corner nodes are made equal to the average of the nodes around it. Care must be taken when setting the tolerance for the convergence of the temperatures. The conductance in the plate is a 'slow' process. Therefore sufficient iterations must be allowed to get a real steady-state answer.

3.4.3. Numerical results

The results for the heat transfer coefficient calculations are D_{hc} = 4.5 mm, h = 18.0 W/m²·K, h_{av} = 1149.4 W/m²·K, Nu = 18 with a plate case temperature 53.84 °C. This corresponds to a maximum plate temperature of 64.25 °C.

The difference in the numerical and experimental exit air temperature profiles, as shown in Figure 3-23 (b), could be attributed to the non-uniformity of the flow through the subunit (Figure 3-20) and damage to some of the fins.

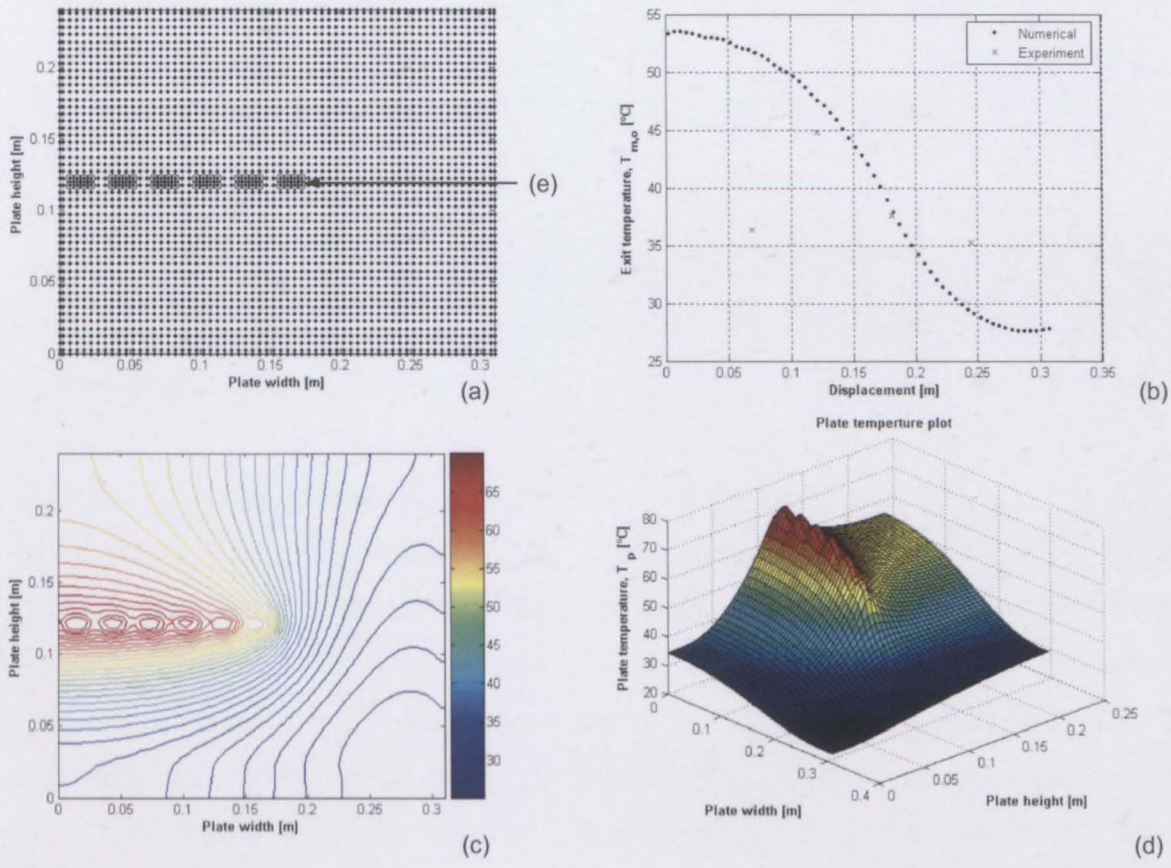

Figure 3-23: Node plot of the plate (a), the exit air temperature profile (b), contour plot of the plate (c) and the 3D plate temperature plot (d). The locations of the transistors on the nodal plot (a) is shown at (e).

3.5. Discussion, conclusion and recommendations

Due to the thermal problems identified with the Kameelperd, the air flow through the REC and the original HPA cooling solution have been analysed. The former was analysed using the results of the REC simulations. From the CFD simulations, the following is recommended to increase the blower pressure and to improve the air flow path in the REC. Note that the blower pressure is negative. An increase in the blower pressure is therefore required.

1. Redesign of the RFE and DA. The units can be combined in a single unit that is more open in the horizontal plane than the current RFE and DA design. The RFE

and DA cannot be removed from their current container due their interaction with the HPA.

2. Removal of the PSI. The PSI can be moved to the other container in the system container. See Figure 1-3 on page 1-5.
3. Rearranging the SYN line replaceable boards such that the boards on which 'block' components are mounted are not above the DSP processors.
4. Either the removal of the existing EMI shield K_1 or replacing it with a new EMI shield design K_2.

In addition to the experimental data shown and discussed in section 3.1, the author tried to measure the air circulating into the system container from the REC. Figure 3-24 shows a sketch representing the HPA with blower, the exits EMI filters and system container wall. The arrows at (a) indicate the air leaving the HPA. The arrows at (b) indicate the air flow leaving the system container. The hot wire anemometer could not get a reading for air entering or leaving the gap between the REC and the system container. However, when the author used a 'wet finger test', it was found that the air changes from leaving and entering the gap frequently at the front and side of the REC. It was possible that at one place the air was entering and at another it was leaving. The arrows at (c) indicate this uncertain air flow. The author does not know what is happening behind the REC (d), since it is inaccessible.

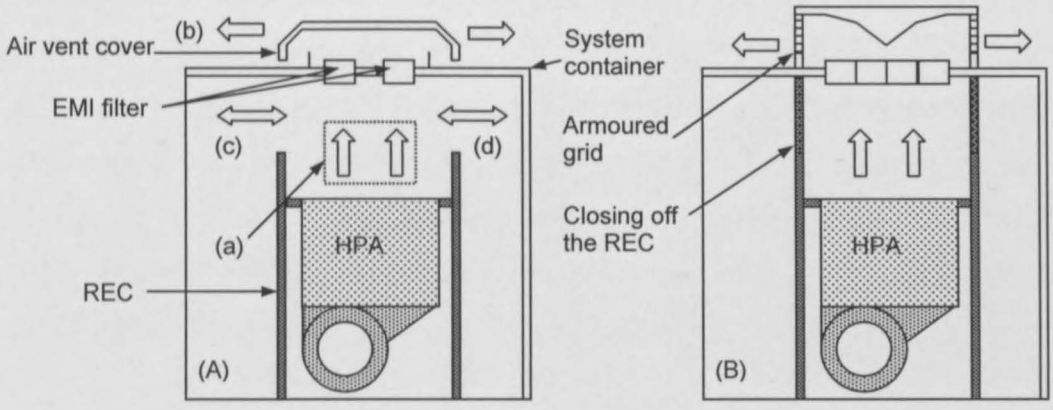

Figure 3-24: Present (a) and recommended (b) REC exit configurations

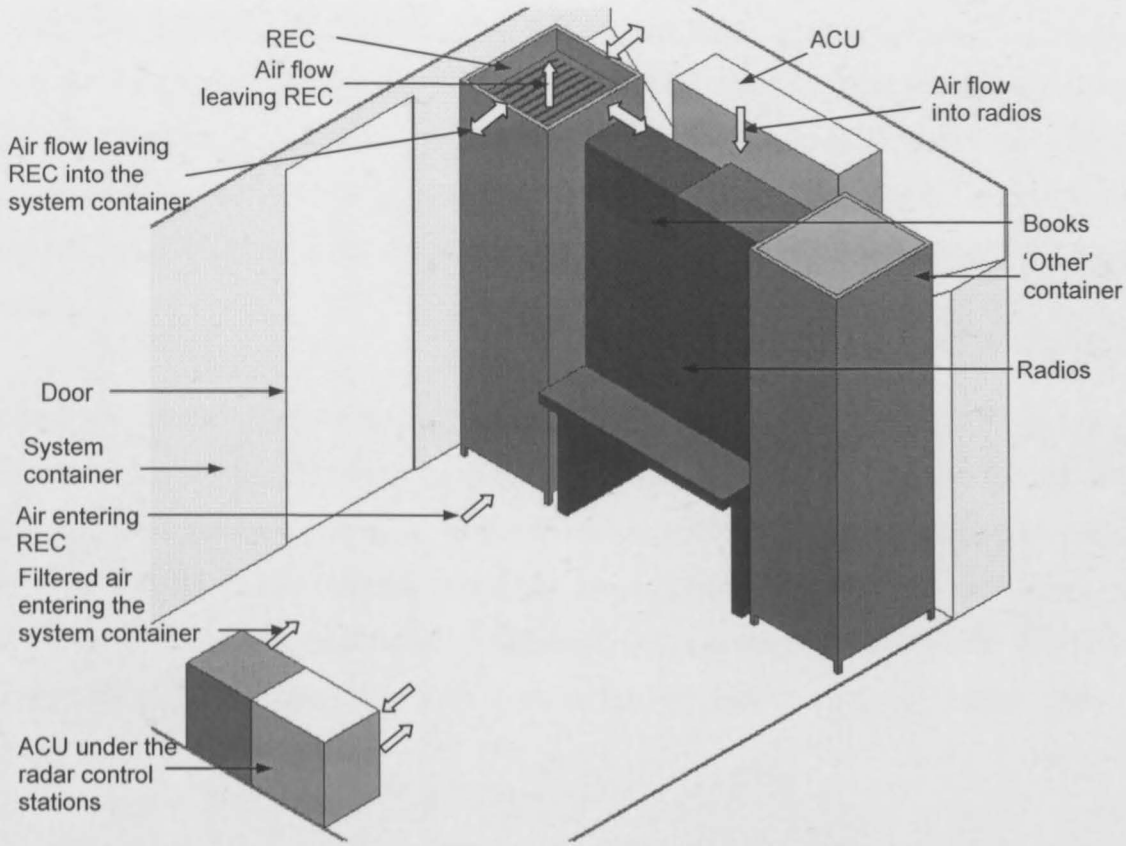

Figure 3-25: Air flow in the system container. Also showing the ACU locations in system container

The EMI filter and air vent cover causes the air flow to circulate back into the system container from the REC. It is recommended that the EMI air flow area and air vent cover exit area be increased to at least 60% of the air flow area inside the REC. Kordyban (1998) states that when the inlet or exit is reduced to less than 60% of the main air flow area in a cabinet, the entrance and exit areas decrease the maximum air flow rate. The air vents cover also needs to be a redesigned, such that it helps the exit air change direction from the vertical to horizontal. To prevent circulation back into the system container, the REC can be closed off, as shown in Figure 3-24 (B).

The increase in the blower entrance will increase the blower air flow rate. If the blower entrance pressure has been increased, the exit EMI shield and cover will still hinder the air flow rate, and must then be redesigned similarly to the sketch shown in Figure 3-24 (b). If, however, the exit EMI shields and cover are not redesigned and the air flow through the REC is increased, this will result in the increase in the

recirculation into the system container. This will result in the increase in the system container temperature and then increase the HPA transistor temperatures. There are air conditioning units inside the system container; however they are not effectively positioned to cooling the air entering the REC. There is an ACU under the radar control stations, while another ACU is located above the radio in a relatively enclosed space.

The focus of the air flow through the REC evaluation was to increase the maximum flow rate. However, at high system container temperatures, the transistors in the HPA exceed their temperature specifications. High system container temperatures occur when the ACU in the system container are switched off. Another condition is when the door of the system container is left open for a protracted time while the system is transmitting. The conditioned air leaves the system container, rather than going through the REC.

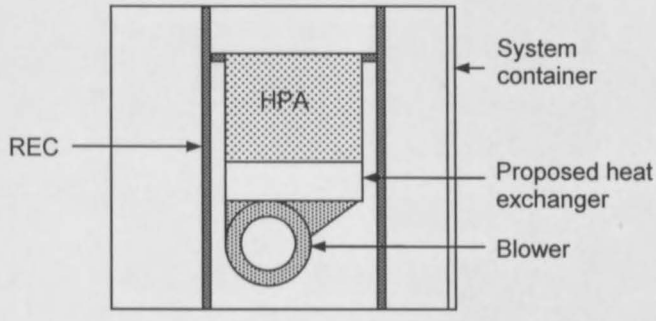

Figure 3-26: Sketch showing the location of the proposed heat exchanger between the HPA and blower

It is proposed that below the HPA subunit and above the blower a heat exchanger be mounted, as shown in Figure 3-26. The heat exchanger will be the evaporator of an air conditioning or refrigeration system. The heat exchanger will remedy the HPA transistor failure when the system container temperature increases if the door is left open. At present, the inlet air flow temperature of the HPA is dependent on the system container temperature. The heat exchanger would make the HPA inlet air flow temperature dependent, primarily, on the evaporator temperature of the refrigerant in the air conditioning system.

In the existing REC layout, there is no space for the heat exchanger. If the recommendations for the reduction of the minimum pressure and improvement of the flow distribution are implemented, this will result in the removal of the PSI. Assuming that the redesign of the RFE and DA will not create a larger combined unit, the space gained in the REC will be that of the PSI. Moving DSP, SYN, RFE/DA down, will create the required space for the heat exchanger.

If the HPA design with the blower, as simulated in this chapter, is removed, it will create circulation problems, as discussed in section 3.3. Replacing the HPA with a closed loop thermosyphon (CLTS) cold plate cooled line replaceable unit (LRU) HPA design, as discussed in section 4.3 on page 4-35, will result in similar problems. CLTS HPA LRU design will be solid in the horizontal direction. It will therefore force the air flow to go around it.

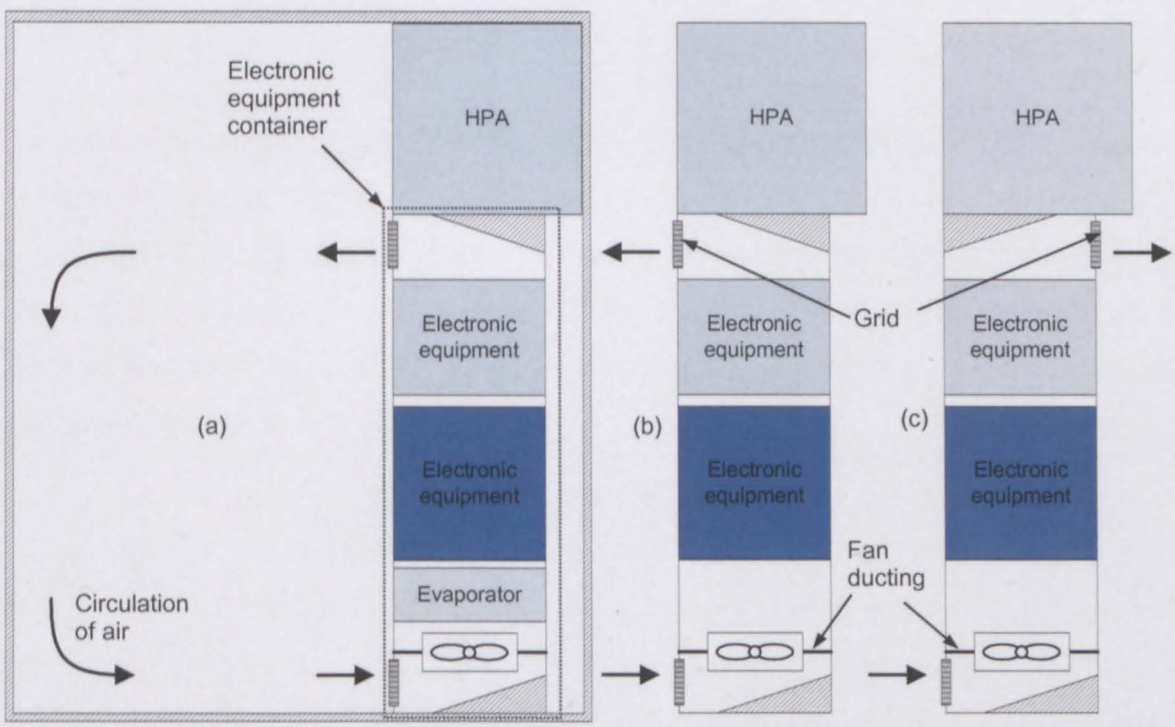

Figure 3-27: Possible future radar equipment container layouts with the HPA above the electronic equipment containers

Figure 3-27 shows configurations where the HPA design is separate to the rest of the electronic equipment. The HPA can either be above or below the electronic

equipment container. A separate HPA design will allow it to be designed such that any water leakages will be prevented from going into the electronic equipment container. Having the HPA below the electronic equipment container will further reduce the risk, if not remove it.

Figure 3-27 (a) shows a REC configuration where the electronic equipment has air cooled by its own air conditioning unit. If the system container air temperature is sufficient for the cooling requirements of the electronic equipment, then the configurations shown in Figure 3-27 (b) & (c) may be used. A circulation zone may be formed between the entrance and exit of the electronic equipment container in Figure 3-27 (a) and (b). This circulation zone must not bypass the system container air conditioning unit. If the circulation zone does bypass the air conditioning unit, then the temperature of the air being circulated in the electronic equipment container will steadily increase until the electronic equipment temperature specifications are exceeded.

To prevent a circulation zone from being formed, the exit of the electronic equipment container could be placed on another side of the container, as shown in Figure 3-27 (c). This exit would now be under the same design considerations as any air flow exit, i.e. the exit must not be blocked off, the air flow area must not be reduced, etc. For configuration (c), the exit could be designed so that the air leaves the system container through it.

Chapter 4 Thermal analysis of proposed changes to the radar system

Due to the thermal problems of Kameelperd and the CSLD analysis done on the original cooling solution, changes to the radar system are needed. Having already completed an evaluation of the flow inside the REC and the original HPA cooling solution in Chapter 3, an alternative HPA cooling solution is to be evaluated.

Before the TMDP can be applied the specifications must first be known. Since the dimensions of the cooling solution are not known, dimensions similar to that of the current HPA are acceptable. The heat transfer rate required is 320 W. Since two-phase thermosyphon/heat pipes are among the cooling solutions being considered, the heat transfer rate required must not be close to the maximum heat transfer rate of the thermosyphon/heat pipe arrangement. The plate temperature, which corresponds to the transistor mounting base temperature, must be below 65 ºC, though the lower the better. The transistor mounting base temperature (65 ºC) was estimated from the plate temperature determined by the numerical model in section 3.4. The energy required to achieve the plate temperature must also be considered. The cooling solution must also be a line replaceable unit (LRU) design (Graham, 2007).

Applying the TMDP, in order to get an alternative HPA cooling solution, requires that the concepts be first generated. Referring to Table 1-1 on page 1-3, the conduction with indirect air cooling, indirect water cooling, heat pipes with indirect water cooling are the cooling solutions being considered. Conduction with indirect air cooling is the original HPA cooling solution and will not be considered. Although indirect water cooling via a water cooled cold plate would have resulted in a cooling solution that has a low thermal resistance and plate temperatures that are independent of the system container air temperature, the client does not want to consider using water inside the electronic equipment container, such as the REC. The risk of water leakage onto the electronics makes direct water cooling of the transistors in the HPA an undesirable cooling solution (Graham, 2007).

Having a cooling solution that is independent of the system container air temperature is a desirable attribute. This would mean that the inlet temperature of the cooling solution can be at 0 °C or lower while the system container air temperature can be 18 °C. The heat dissipated would first be transferred outside the REC and then transferred to water or refrigerant at low temperatures.

Heat pipes were considered to transfer the heat dissipated by the transistors to a water cooled cold plate, which would be outside of the REC. In order to have a LRU design, there was insufficient space to have a sufficient condenser area, as shown in Figure 4-1. The limited condenser area will adversely affect the maximum heat transfer rate of the heat pipe.

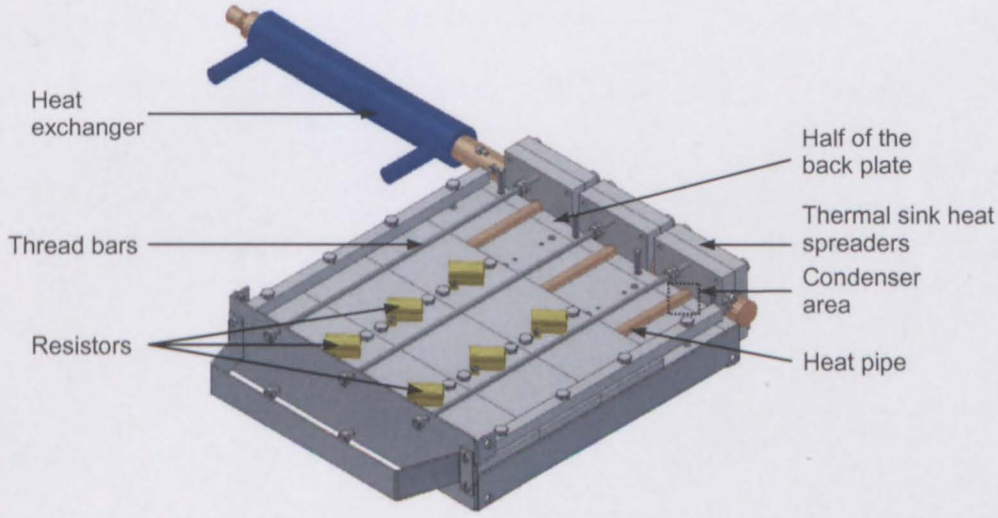

Figure 4-1: Cut away sketch of the heat pipe HPA LRU design

In order to increase the condenser length, a bent heat pipe was proposed. Since the bent heat pipes had to be custom made and imported, it was decided to use a bent thermosyphon (BTS) instead of a bent heat pipe. An alternative to a BTS is a closed loop thermosyphon (CLTS). In most cases, a CLTS would have the condenser and evaporator either both in the vertical position, shown in Figure 4-2 (a), or both in the horizontal position. The CLTS that will be used will have the condenser vertical, while the evaporator is horizontal, as shown in Figure 4-2 (b). The concept for the BTS and CLTS HPA LRU designs are similar to each other and are shown in Figure 4-3.

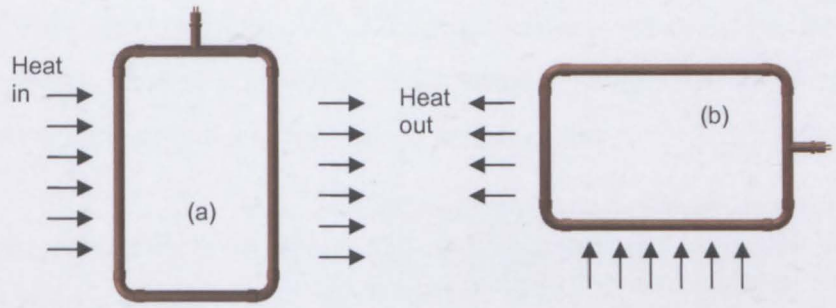

Figure 4-2: A frequently used closed loop thermosyphon confirguration (a), with the configuration used shown (b)

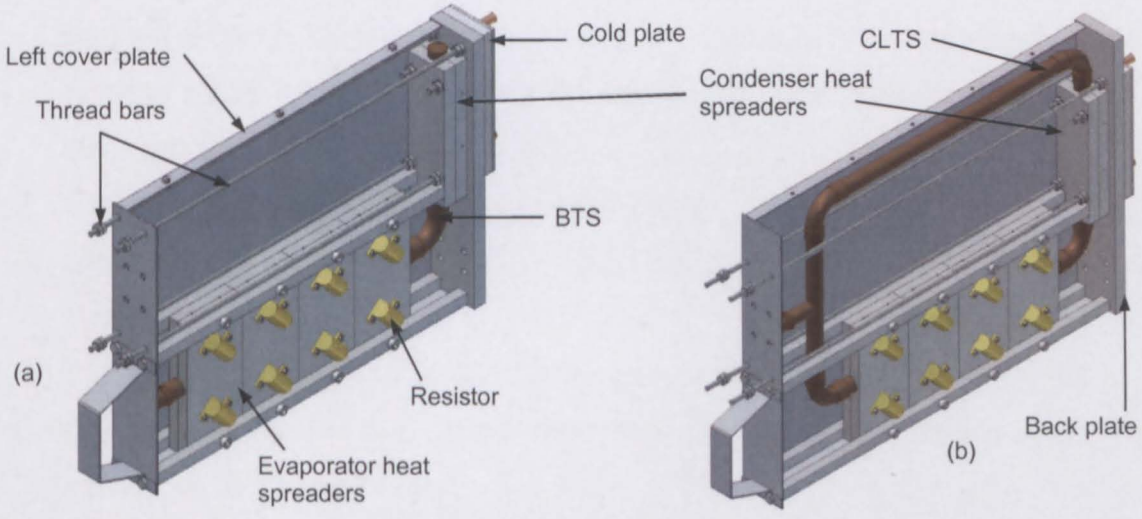

Figure 4-3: BTS (a) and CLTS (b) HPA LRU concepts

In the BTS and CLTS concepts there are four sets of evaporator heat spreaders, on which eight resistors are mounted. The condenser section is held between two heat spreaders which are bolted to the back plate. The evaporator and condenser heat spreaders are enclosed by two covers, which can be secured externally. Only the left cover plates are shown in Figure 4-3.

Thread bars enable the back face of the LRU to be securely mounted to an external thermal sink. The thread bars also enabled the design to be a LRU, while still having

a good thermal interface with the thermal sink. The thermal sink in Figure 4-3 is a water cooled cold plate. BTS and CLTS industrial designs could be cooled by either water or refrigerant cooled cold plate. The water or refrigerant temperature will also be independent of the system container air temperature.

Since the concepts have been chosen, a CSLD analysis was done to help identify the heat transfer path. CSLD also helps identify possible problems which may arise. The cooling solution level definitions, as discussed in Jeggels (2007), for the BTS and CLTS HPA LRU are given by the following points:

1. Conduction from the transistors to plate heat spreaders of the evaporator. The transistor is a 1st level item. Note that although conduction takes place between two objects, there is no thermal paste involved. The transistors are earthed through its base. Adding thermal paste between the transistor base and the plate, as in the original HPA design, added too much capacitance to the earth of the transistors.
2. Conduction in the evaporator heat spreaders.
3. Conduction via thermal paste from the evaporator plate heat spreader to the themosyphon.
4. Two-phase heat transfer in the thermosyphon.
5. Conduction via thermal paste from the thermosyphon to the plate heat spreaders of the condenser.
6. Conduction in the condenser heat spreaders.
7. Conduction via thermal paste from the condenser heat spreaders to the back plate.
8. Conduction in the back plate. The back plate is a 5th level item, since it is the interface of the LRU.
9. Conduction via thermal paste from the back plate to a refrigerant cooled cold plate. The cold plate is 6th level item, since a number of LRUs would transfer their heat dissipated to it.
10. Either single or two-phase convection heat transfer to water or refrigerant, respectively.
11. Energy gained by the water or refrigerant is transported by the fluid to a refrigeration unit. The refrigeration unit is an 8th level item, since it is normally considered to be a complete system on its own.

12. Refrigeration unit dissipates energy to the environment.

Note that in point 1, conduction heat transfer takes place from the transistor to the evaporator heat spreaders without the aid of thermal paste. The surface finish of the transistors and evaporator heat spreaders are critical. The above points with "conduction via thermal paste" indicate an interface between two items. Care must be taken to reduce the thermal contact resistance by first simplifying the interface design and then applying the thermal paste correctly (Jeggels and Dobson, 2007). The CSLD is shown graphically in Figure 4-4.

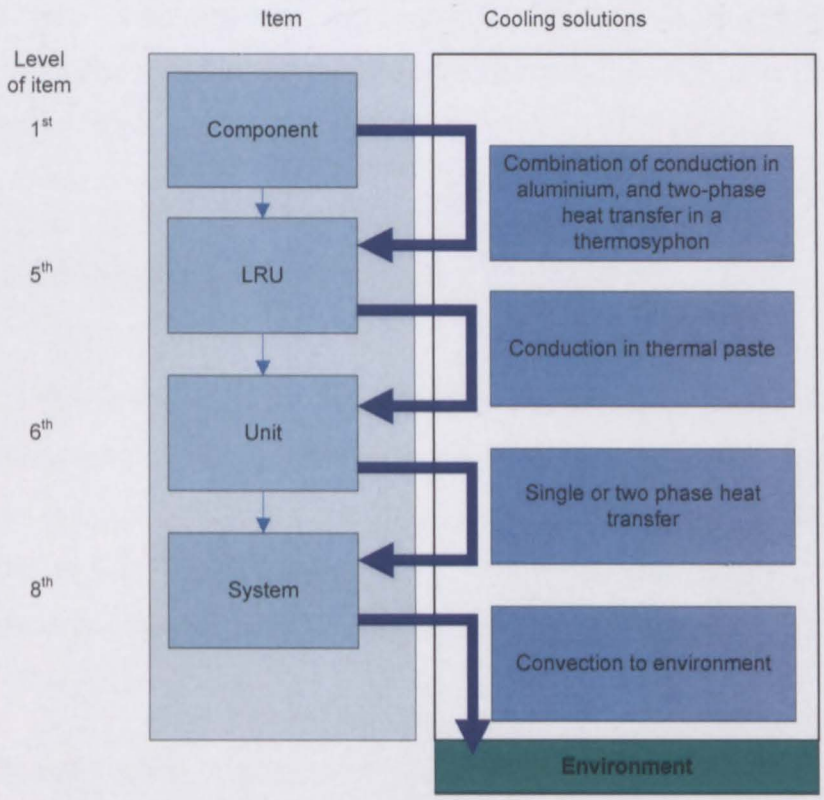

Figure 4-4: BTS and CLTS HPA LRU CSLD breakdown

For this project, the BTS and CLTS HPA LRU will be designed up to point 8. For an industrial project, all the points will have to be taken into account. When the energy dissipated by the transistors has been transferred to the water or refrigerant in point 10, the transfer of the fluid to the refrigeration unit (point 11) and the heat dissipation of the refrigeration unit to the environment (point 12) needs to be taken into

consideration. The refrigeration unit cannot have, for example, the condenser heat exchanger in an enclosed space or next to the diesel generator.

Considering the CSLD, the only unknown heat transfer parameters are the thermal resistance and maximum heat transfer rates of the BTS and CLTS. There is literature on a cranked shaped (⌙) heat pipe by Imura and Ippohshi (2000), but none found for the BTS configuration. Miyasake, Nakajima and Tsunoda (1995) documented experiments for different evaporator locations for a 2 mm inside diameter copper tube. There is not enough information to get any useful data from the article. It does however mention that the current configuration works. Ippohshi, et al. (2003) gives a top-heat mode loop thermosyphon, but is not the current CLTS configuration. The thermal resistance and maximum heat transfer rates of the BTS and CLTS needs to be experimentally determined.

4.1. Bent thermosyphon experiment

The purpose of this section is to document the experiments conducted to find the thermal resistance and maximum heat transfer rate of different BTS configurations. The subsequent sections describe the experimental set up and procedure (4.1.1), analysed results (4.1.2) of the experiments. The measured values and processed results of the experiments are given on the DVD in Appendix A.

4.1.1. BTS experimental set up and procedure

The BTS was manufactured from ½" cold drawn copper tubes, a standard long radius elbow, a schurder valve and two thermocouple attachments, and is shown in Figure 4-5. Heat was dissipated by 25 Watt ARCOL power resistors mounted on plate heat spreaders. There are three sets of plate heat spreaders with 6 resistors in total. The heat dissipated is removed by a water cooled tube-in-tube heat exchanger, with spirals between the heat exchanger copper tube and the BTS copper tube. The plate heat spreaders are 50 mm square and 10 mm thick. The resistors are mounted so that they are above the BTS evaporator and in the centre of the plate heat spreaders.

The last plate heat spreaders are mounted 10 mm from the end of the evaporator. There is a 2-3 mm gap between the evaporator heat spreaders. The evaporator length is 200 mm while the condenser length covered by a heat exchanger is 100 mm long. The heat exchanger weld starts at the elbow.

R134a was used as the working fluid. The mass of working fluid required is a sixth of the volume of the total length of the BTS while the working fluid is at 25°C. The fill ratio (FR) is defined as the mass of working fluid added to the BTS divided by the mass required. The volume required for the tested BTS was 5.829 mL, resulting in 7g being the required mass of R134a.

$$V_{wf} = V_t/6 = \pi d_i^2 L_t/24 \tag{4.1}$$

$$m_{wf,required} = \rho_{wf}\big|_{T_{wf}=25°C} \times V_{wf} \tag{4.2}$$

$$FR = m_{wf,filled}/m_{wf,required} \tag{4.3}$$

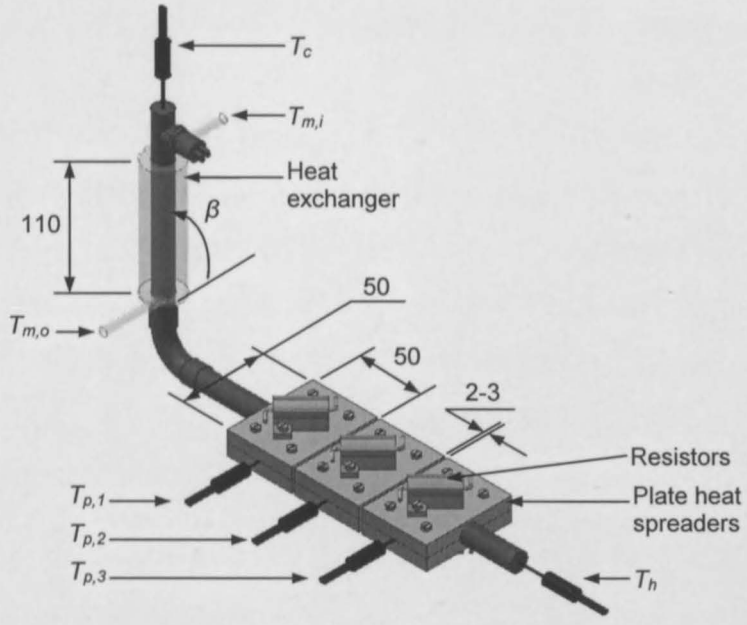

Figure 4-5: Sketch of the experimental BTS set up. Insulation is not shown.

The BTS was assembled using the thermal paste application method in Jeggels and Dobson (2007). The evaporator was covered by insulation, while making sure that the evaporator is horizontal. Plastic tubes were connected to the heat exchanger.

Holes were cut in the plastic tube and thermocouples inserted so that they were pointed in the opposite direction of the water flow. The thermocouples used in the testing had a collective bias error of ±0.1 °C.

To fill the BTS, the empty BTS configuration was weighed using Adam equipment CBW-30 scale (serial no. AE 273510821). A specific volume of working fluid was drawn into an evacuated filling tube. A vacuum was drawn in the BTS and the working fluid was poured into it from the filling tube. In order to get the working fluid to flow from one container to another, the container losing the working fluid is heated. The temperature difference causes a pressure difference between the containers. This results in fluid leaving the higher temperature container. When filled the BTS is purged of any air remaining in it and weighed. Purging a thermosyphon is when the non-condensable gases are removed from the thermosypon. This is achieved by depressing the valve of the thermosyphon. The difference between the filled mass and the empty mass is the mass of working fluid added. Excess working fluid is purged until the working fluid in the BTS is equal to the required working fluid mass.

The cooling water flow rate was measured using a stop watch and a measuring cylinder. Power was supplied to the resistors by a power supply. At a given power rating, temperatures were recorded when they had reached steady-state. The angle of the condenser, β, was also varied. The angle was measured from the horizontal, i.e. a vertical condenser was measured as 90°, as shown in Figure 4-5. A computer, Solatron Instruments SI 35951C IMP (serial no. 00115331) and T-type thermocouples were used during the experiments.

4.1.2. BTS experimental results

The energy input into the system is calculated from the sum of the energy dissipated by the resistors. The energy dissipated by the resistors is calculated from Ohm's law, equation (4.4). The energy leaving the system is calculated from the energy gained by the cooling water (equation 4.5), while the percentage difference between the energy input and output or energy loss is calculated using equation (4.6). It can be seen in Figure 4-6 (a) that the average energy loss was 10%.

$$\dot{Q}_i = \sum V^2/R \tag{4.4}$$

$$\dot{Q}_o = \rho_m \dot{G}_m c_{p,av}\left(T_{m,o} - T_{m,i}\right) \tag{4.5}$$

$$\Delta\dot{Q} = 100 \times \left(\dot{Q}_i - \dot{Q}_o\right)/\dot{Q}_i \tag{4.6}$$

To evaluate the heat transfer rate for the BTS, a system temperature difference was defined as the difference between the average plate temperature and the average water temperature (equation 4.9). To evaluate the difference in the plate temperatures for an experiment, the spread in the plate temperatures is indicated by S_+ and S_- (equation 4.10 & 4.11), which are indicated by the "error" bars shown in Figure 4-6 (b).

$$T_{p,ave} = \frac{1}{m}\sum_{n=1}^{m=3} T_{p,n} \tag{4.7}$$

$$T_{m,av} = \left(T_{m,i} + T_{m,o}\right)/2 \tag{4.8}$$

$$\Delta T_{sys} = T_{p,ave} - T_{m,ave} \tag{4.9}$$

$$S_+ = \left|\mathrm{MAX}\left(\left\{T_{p,n} - T_{m,av}\right\}\Big|_{n=1}^{m}\right) - \left(T_{p,av} - T_{m,av}\right)\right| \tag{4.10}$$

$$S_- = \left|\mathrm{MIN}\left(\left\{T_{p,n} - T_{m,av}\right\}\Big|_{n=1}^{m}\right) - \left(T_{p,av} - T_{m,av}\right)\right| \tag{4.11}$$

Below 110 W power input the BTS configurations, shown in Figure 4-6 (b), have the same thermal resistance characteristics. The 90° FR 1 configuration shows a steady increase in the spread of the plate temperatures. For example, at 146 W the minimum plate temperature is 82.5 °C while the maximum is 93.0 °C. Increasing the power input to 156 W gives a minimum plate temperature of 84.4 °C while the maximum is at 153.5 °C. Although the BTS at 90° FR 1 can transfer energy up to 146 W with only a plate temperature spread of 4.4 °C, a more practical heat transfer rate for the BTS is a power input of 134 W.

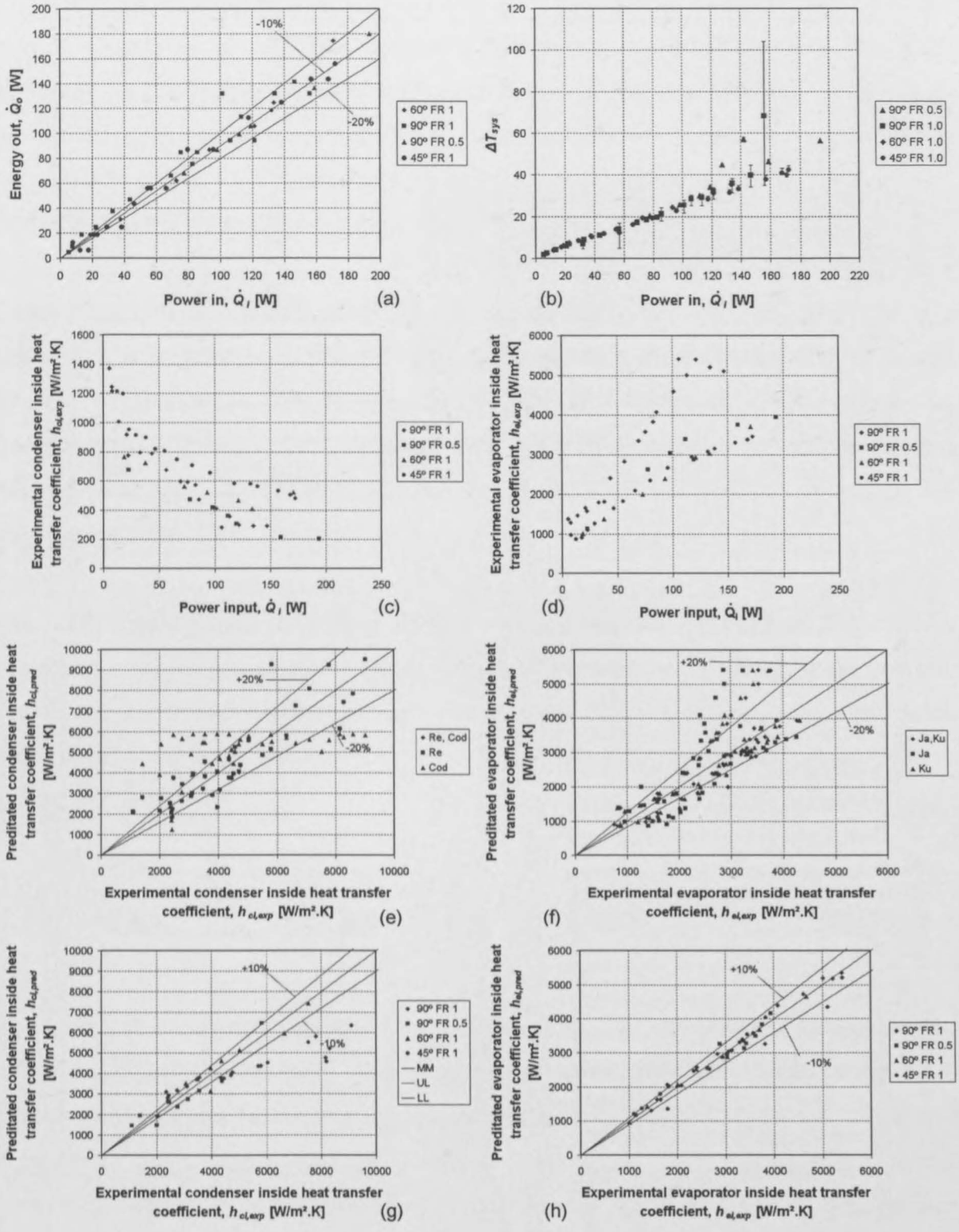

Figure 4-6: Heat transfer rate, energy balances and evaporator and condenser inside heat transfer coefficients, predicted and experimental, for different β angles of the BTS condenser. (R134a working fluid)

When the FR is decreased to 0.5 for a 90° configuration the maximum heat transfer rate is increased to 193 W. Increasing the power input will lead to the plate temperature increasing uncontrollably. But there is also no indication (spread in temperature) to when the maximum heat transfer rates will be achieved, in comparison to the FR 1 experiment. A practical power input would be between 160 and 180 W, with a plate temperature spread of 2 °C at 160 W.

Decreasing the condenser angle, β, to 60 or 45° gives no noticeable thermal resistance advantage over the 90° orientation below 110 W. Above 110 W power input, the thermal resistance increases for the 90° FR 1 configuration. However, decreasing the FR for a 90° orientation (90° FR 0.5) does not increase the thermal resistance above 110 W. The tests were stopped at a 40° temperature difference, i.e. the maximum heat transfer rate was not achieved for 60° or 45° β angles.

The internal temperature of the BTS is defined as the average of the internal thermocouples temperatures (equation 4.12). The evaporator inside heat transfer coefficient is defined for the power input at the difference between average plate temperature and the internal temperature for the evaporator length (equation 4.14).

$$T_i = \left(T_h + T_c\right)/2 \tag{4.12}$$

$$A_{e,i} = \pi d_i L_e \tag{4.13}$$

$$h_{e,i} = \dot{Q}_i \Big/ \left(A_{e,i} \times \left(T_{p,av} - T_i\right)\right) \tag{4.14}$$

The condenser inside heat transfer coefficient is not as easy to define as the evaporator heat transfer coefficient. This is due to the condenser tube's temperature being unknown. The heat transfer from the working fluid to the condenser is defined in equation (4.15), assuming negligible wall resistance. The condenser inside heat transfer coefficient $h_{c,i}$ is for heat transfer from the working fluid in the BTS to the wall of the condenser. The heat transfer coefficient $h_{c,o}$ is the heat transfer coefficient for heat transfer from the wall of the condenser to the water. Equation (4.15) is rearranged into equation (4.16), after which it is simplified to equation (4.17). The heat transfer coefficient $h_{c,i}$ is determined equation (4.18), by rearranging equation (4.17).

$$\dot{Q}_i = \frac{T_i - T_{m,av}}{R_{w,m} + R_{i,w}} = \frac{T_i - T_{m,av}}{\frac{1}{h_{c,o}A_{c,i}} + \frac{1}{h_{c,i}A_{c,i}}} \tag{4.15}$$

$$\dot{Q}_i \times \frac{\left(\frac{1}{h_{c,o}A_{c,i}} + \frac{1}{h_{c,i}A_{c,i}}\right)}{\dot{Q}_i} = \frac{T_i - T_{m,av}}{\frac{1}{h_{c,o}A_{c,i}} + \frac{1}{h_{c,i}A_{c,i}}} \times \frac{\left(\frac{1}{h_{c,o}A_{c,i}} + \frac{1}{h_{c,i}A_{c,i}}\right)}{\dot{Q}_i} \tag{4.16}$$

$$\frac{1}{h_{c,o}} + \frac{1}{h_{c,i}} = A_{c,i}\frac{T_i - T_{m,av}}{\dot{Q}_i} \tag{4.17}$$

$$h_{c,i} = \left(A_{c,i}\frac{T_i - T_{m,av}}{\dot{Q}_i} - \frac{1}{h_{c,o}}\right)^{-1} \tag{4.18}$$

$$A_{c,i} = \pi d_i L_c \tag{4.19}$$

To determine $h_{c,o}$, a channel is defined out of the four spirals in the condenser heat exchanger. Since the heat exchanger is 100 mm long, the channel will have a width w = 20 mm. The height is the difference between the heat exchanger tube radius of 11 mm and the condenser radius of 6.35 mm, which results in b = 4.65 mm. The hydraulic diameter is defined in equation (4.20).

$$D_h = 4A/P \tag{4.20}$$

where $A = w \times b$ (4.21)

$$P = 2(w + b) \tag{4.22}$$

The mass flow rate is determined from the volume flow rate and the density of the water at the linear average water temperature. The viscosity, Prandtl number and conductivity are also determined at the linear average water temperature. The Dittus-Boelter equation, equation (4.25), is used to determine the Nusselt number for $h_{c,o}$. The heat transfer coefficients are plotted against the input power in Figure 4-6 (c) and (d).

$$\dot{m} = \rho_{m,av}\dot{G}_m \tag{4.23}$$

$$\mathrm{Re} = (4\dot{m})/(\pi D_h \mu_{m,av}) \tag{4.24}$$

$$Nu = 0.023 Re^{0.8} Pr^{0.4} \quad (4.25)$$

$$h_{c,o} = Nu k_{m,av} / D_h \quad (4.26)$$

Figure 4-6 (c) shows that as the power input is increased, the condenser inside heat transfer coefficient decreases while the evaporator heat transfer coefficient increases (d). This is because the higher the heat flux rate in the evaporator, the higher the nucleate boiling and 'bubble pumping', therefore the higher the evaporator heat transfer rate. Liquid deposition on a surface creates a film which increases in thickness as the heat transfer rate increases. Due to the thermal resistance of the film, the condensation heat transfer coefficient decreases with increasing heat transfer rate. The regression equations to be applied to the experimentally determined evaporator and condenser inside heat transfer coefficients are given by equations (4.27) and (4.28), respectively. The equations (4.27) and (4.28) were previously used by Meyer (2004). The terms are determined at the average of T_c and T_h. Data used for the regression were while the BTS experiment heat transfer rate increased linearly with temperature difference, and before maximum heat transfer rate was achieved. For the 90° FR 1, heat transfer rates less than 120 W were used, while all the data was used for the 90° Fr 0.5, 60° and 45° experiments.

$$h_{ei} = b \times Ja^{m1} Ku^{m2} \quad (4.27)$$

$$h_{ci} = b \times Re_l^{m1} Cond^{m2} \quad (4.28)$$

where

$$Ja = c_{p,l}\left(T_w - T_{sat}\right)/h_{fg} \quad (4.29)$$

$$Re_l = \frac{\rho V d_i}{\mu} = \frac{\rho\left(4\dot{m}/\rho\pi d_i^2\right)d_i}{\mu} = \frac{4\dot{m}}{\pi d_i \mu} = \frac{4\dot{Q}/h_{fg}}{\pi d_i \mu} = \frac{4\dot{Q}}{\pi d_i \mu h_{fg}} \quad (4.30)$$

$$Ku = \dot{Q} \Big/ \left[\rho_v h_{fg} \left(\frac{\sigma g \left(\rho_l - \rho_v\right)}{\rho_v^2} \right)^{0.25} \right] \quad (4.31)$$

$$Cond = k_l \Big/ \left(\frac{\mu_l^2}{\rho_l g \left(\rho_l - \rho_v\right)} \right)^{1/3} \quad (4.32)$$

The Jakob number is the ratio of sensible to latent energy absorbed during the liquid-vapour phase change (Incropera and DeWitt, 2002). It, therefore, compares the maximum sensible heat, $c_p \Delta T$, absorded by the liquid to the latent heat absorbed (Lienhard and Lienhard, 2006). The Kutateladze number is a non-dimensional heat flux. The Reynolds number is the ratio of the inertia and viscous forces (Incropera and DeWitt, 2002). The condensation term, Cond, is from laminar film condensation theory.

Correlations using all the data of the BTS experiments give widely scattered results, as shown in Figure 4-6 (e) and (f). For example, using Ja and Ku to predict the evaporator inside heat transfer coefficient results in an average percentage difference between the predicted and experimental data of 17.9 % with a maximum of 49.2 %, as shown in Table 4-1. Generating correlations for each experiment gave the best results, shown in Table 4-2. Using the Reynolds number for condensation regression gave the best correlation, while using Ku and Ja numbers gave the best correlations for the evaporator. The regression limitations for a specific configuration of the BTS experiment are also shown in Table 4-2.

Table 4-1: Regression coefficient for correlation for all BTS experimental data

	Regression hei			Regression hci		
Regression terms used	Ja, Ku	Ja	Ku	Re, Cond	Re	Cond
b	668462.47	19610.74	383124.23	2953217	77655.96	5.43E-79
m1	-0.2109	0.6714		14.898	11.260	-180.213
m2	0.5740		0.4629	-0.510	-0.506	
R^2	0.8054	0.5639	0.7901	-0.418		21.788
Average % difference	17.9	27.0	18.2	0.674	0.676	0.231
Maximum % difference	49.2	94.3	47.9	22.987	23.014	44.226

Table 4-2: Regression coefficients for the BTS experiments

Experimental configuration	90° FR 1		90° FR 0.5		60° FR 1		45° FR 1	
Heat transfer coefficients	h_{ei}	h_{ci}	h_{ei}	h_{ci}	h_{ei}	h_{ci}	h_{ei}	h_{ci}
Regression terms used	Ja, Ku	Re	Ja, Ku	Re	Ja, Ku	Re	Ja, Ku	Re
b	11745577	16099.64	6336518	55187.5	5560447	22782.92	164238	151505.1
m1	-0.88992	-0.24278	-0.6875	-0.51086	-0.39230	-0.29	0.20067	-0.54821

m2	1.016	0	0.935	0	0.84396	0.00	0.34343	
R^2	0.96	0.433	0.982	0.826437	0.99463	0.7898	0.96317	0.995353
Average % difference	7.8	28.2	3.4	17.52607	13.7	8.946252	7.0	55.47151
Maximum % difference	23.4	70.8	12.1	37.95545	33.5	21.14124	20.5	136.1347
Maximum heat transfer limits [W]	120		190		170			

4.1.3. Discussion and conclusions for the BTS experiments

The purpose of the BTS experiment was to experimentally determine the thermal resistance and maximum heat transfer rates, in order to evaluate its use as a cooling solution for the HPA. This section has documented the experimental set up and procedure of the BTS experiments, followed by the experimental results. A maximum heat transfer rate of 190 W was found for a vertical condenser, which is less than the required heat transfer rate of 320 W. A single BTS configuration can thus not be used as a possible cooling solution for the HPA.

It was found that changing the condenser angle, β, increases the maximum heat transfer rates while not changing the thermal resistance. When a condenser is vertical, counter flow annular two-phase flow is present. When a condenser is inclined, counter flow stratified two-phase flow is present. Counter flow stratified two-phase flow can therefore maintain a higher maximum heat transfer rate than counter flow annular two-phase flow.

4.2. Closed loop thermosyphon experiment

The purpose of this section is to document the experiments conducted to find the thermal resistance and maximum heat transfer rate of different CLTS configurations. The configurations differ in diameters and working fluid. The diameters chosen were ¼" (6.35 mm, 0.61 mm t_w), ⅜" (9.5 mm, 0.61 mm t_w) and ½" (12.7 mm, 0.71 mm t_w) outside diameter tubes. The diameter of the thermosyphon selected for practical designs will depend on the heat transfer rate, the maximum heat transfer rate, the

volume and, dependent on the aforementioned, the mass of the cooling solution. Working fluid selection depends on its compatibility with the thermosyphon tube material copper and the working temperature range.

Possible working fluids are water, refrigerant R134a, ammonia, acetone, methanol, ethanol, propane and butane. The working fluid will be evaluated depending on the minimum and maximum operational temperatures, compatibility with the thermosyphon tube material and the maximum heat transfer rate. Ammonia cannot be used since it is incompatible with the copper thermosyphon tube material. Water will freeze if the internal temperature of the thermosyphon is below 0 °C.

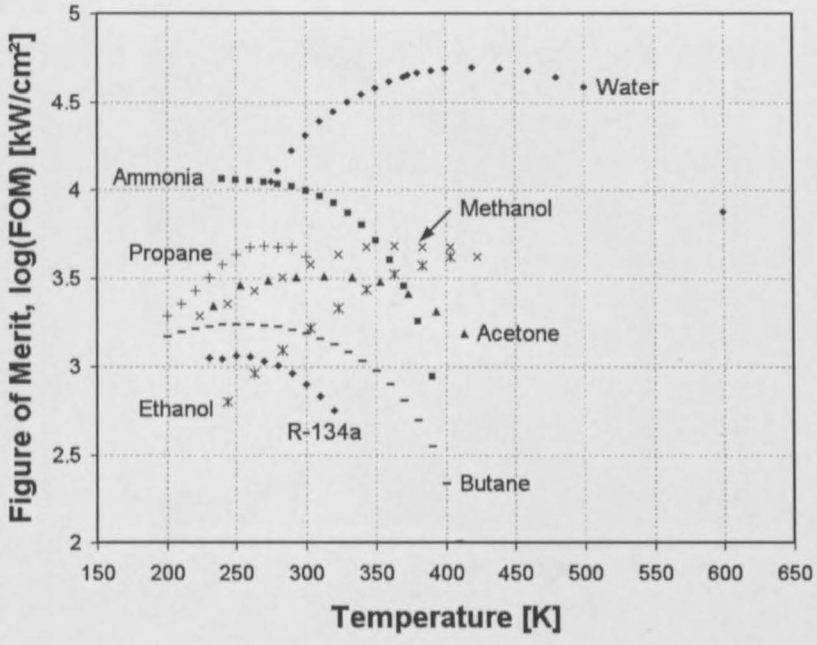

Figure 4-7: Figure of merit (FOM) for a number of heat pipe and thermosyphon fluids. The data used to compile this figure is from Lemmon, McLinden and Friend (2005), Faghri (1995) and Mills (1998).

The figure of merit (FOM) can be used to evaluate the maximum heat transfer rate for a working fluid. FOM is defined as $\rho_l \sigma h_{fg}/\mu$ and is usually expressed in kW/cm². It

is plotted in Figure 4-7. It shows that R134a has a lower FOM that butane, but water has the highest.

The FOM does not indicate the thermal resistance of the working fluid. This will have to be determined experimentally for the various diameters and working fluids. From the above working fluid considerations, it was decided to test the CLTS with R134a, butane and water.

4.2.1. CLTS experimental set up and procedure

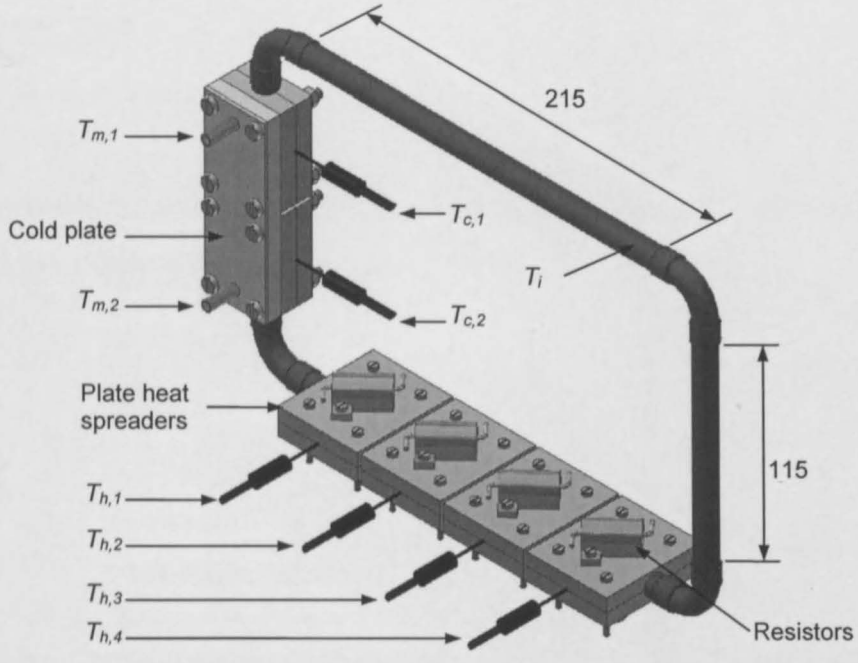

Figure 4-8: Sketch of the experimental CLTS set up. Insulation is not shown.

CLTS were manufactured out of cold drawn copper tubes, four elbows and a schurder valve as shown in Figure 4-8. The available evaporator length is 215 mm, while the condenser is 115 mm. The valve is placed in the centre of one of the condenser lengths. Heat is generated by 25 Watt ARCOL power resistors mounted on plate heat spreaders. The plate heat spreaders are 50 mm long and 10 mm thick for the ½" CLTS, while 8 mm thick for the ¼" and ⅜" CLTS. The resistors are

mounted so that they are above the CLTS evaporator and in the centre of the plate heat spreaders. The CLTS was assembled using the thermal paste application method in Jeggels and Dobson (2007).

The mass of working fluid required is the CLTS evaporator volume while the working fluid is at 25 °C. The fill ratio (FR) is defined as the mass of working fluid added to the CLTS divided by the mass required. The required mass for different diameters and working fluids is given in Table 4-3 for FR 1. The FRs used in the experiments are as close to the required mass as possible, but due to the inaccuracy of the scale the working fluid is only accurate to 0.001 kg.

$$V_{wf} = V_e = \pi d_i^2 L_e / 4 \tag{4.31}$$

$$m_{wf,required} = \rho_{wf}\big|_{T_{wf}=25°C} \times V_{wf} \tag{4.32}$$

$$FR = m_{wf,filled} / m_{wf,required} \tag{4.33}$$

Table 4-3: Mass of working fluid required for fill ratio 1 for different closed loop thermosyphon diameters and working fluids

Mass required for FR 1 [g]			
	CLTS diameter		
Working fluid	1/4"	3/8"	1/2"
R134a	5.0	13.4	25.9
Butane	2.3	6.3	12.2
Water		11	21

Butane and R134a were charged as follows: To fill the CLTS, the empty CLTS configuration was weighed using Adam equipment CBW-30 scale (serial no. AE 273510821). A specific volume of working fluid was drawn into an evacuated filling tube. A vacuum was drawn in the CLTS and the working fluid was poured into it from the filling tube. In order to get the working fluid to flow from one container to another, the container losing the working fluid is heated. The temperature difference causes a pressure difference between the containers. This results in fluid leaving the higher temperature container. When filled with working fluid, the CLTS valve is depressed and gases are allowed to escape to the atmosphere. The valve is depressed in order to remove non-condensable gases that are inside the CLTS. The CLTS is weighed.

The difference between the filled mass and the empty mass is the mass of working fluid added. Excess working fluid is purged until the working fluid in the CLTS is equal to the required working fluid mass.

The water used in the CLTS experiments was first distilled and boiled again before being used to charge a configuration. Since water is a liquid at atmospheric pressure, other methods need to be used to charge a CLTS. For the first method, a vacuum was drawn and the entrance of the CLTS valve is placed in distilled water. The valve is then opened and depending on the pressure of the vacuum, the entire volume of the CLTS can be filled with water. The second method uses a syringe to add slightly more than the required volume of water to empty CLTS configuration. Care must be taken that the syringe needle is in the CLTS tube and not in the valve. The water will otherwise come straight out of the CLTS. Care must also as be taken with the syringe itself. The recommended method to replace the syringe cap is when the cap is placed on a surface and the syringe's needle is moved into the cap, as shown in Figure 4-9 (b). Then only is the cap secured.

To get the correct mass of water in the CLTS, the CLTS evaporator plates are heated to above 100 ºC. The CLTS should be orientated such that the evaporator is the lowest part of the CLTS. This will allow the water to flow to the evaporator and to begin boiling, thereby increasing the pressure inside the CLTS. The heated CLTS is then orientated such that the valve is vertical, as shown in Figure 4-9 (a). Note the gloves worn by the author. The valve is then depressed and steam escapes from the CLTS. This is called purging. After about 2 seconds, the intensity of the steam will begin to diminish. The CLTS is then again orientated such that the evaporator is the lowest part of the CLTS. The water will begin to boil again, increasing the pressure inside. The difference between the filled mass and the empty mass of the CLTS assembly is the mass of working fluid added. The CLTS is purged until the required working fluid mass has been achieved. The second filling method is recommended due to the time saved in the purging process, since the added water is close to the required water mass. The author found that when the energy to heat the CLTS was supplied by the evaporator resistors, a 125 ºC evaporator temperature worked well to purge the water from the CLTS.

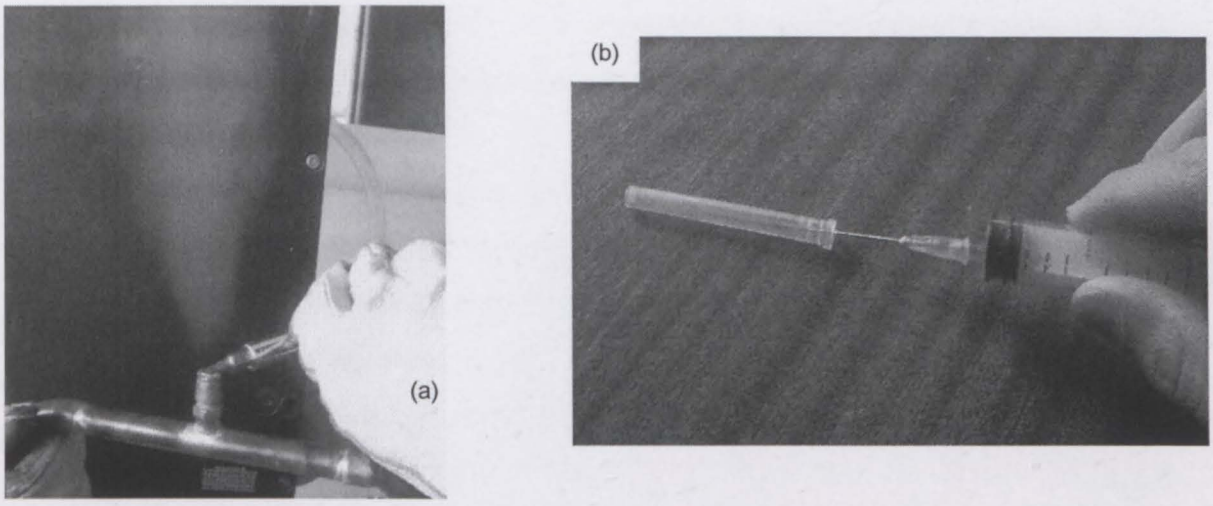

Figure 4-9: Steam purged from the CLTS (a) with the recommended syringe method

After the CLTS has been set up, thermocouples, power supply wires and water supply pipes were attached. The set up was placed such that the evaporator was horizontal, and insulated using glass wool. The cooling water flow rate was measured using a stop watch and a measuring cylinder. Power was supplied to the resistors by various power supplies or a variac. When using a Variac, a Brymen TBM805 digital multimeter (serial no.: 043330505) was used to measure the electrical resistance of the resistors and the voltage supplied by the Variac. When the author wanted to test above 200W, the 8 resistors had to be replaced by 16. This was done by having a single resistor's 2 bolt holes used by 2 resistors. For the same power there was no difference in the experimental data when using 8 or 16 resistors. At a given power rating, temperatures were recorded when they had reached quasi steady-state. Quasi steady-state is present since the temperature of the water increased during the testing, but very slowly. A computer, Solatron Instruments SI 35951C IMP (serial no. 00115331) and T-type thermocouples were used during the experiments.

4.2.2. CLTS experimental processing procedure

This section discusses the equations and methods used to process the experimental results of the close loop thermosyphon (CLTS) tests. The processed data for each

working fluid is discussed in 4.2.3, 4.2.4 and 4.2.5. The different working fluids will be compared to each other for different diameters in section 4.2.6.

The energy input into the system is calculated from the sum of the energy dissipated by the resistors. The energy dissipated by the resistors is calculated from Ohm's law, equation (4.34). The energy leaving the system is calculated from the energy gained by the cooling water (equation 4.35), while the percentage difference between the energy input and output is calculated using equation (4.36).

$$\dot{Q}_i = \sum V^2/R \tag{4.34}$$

$$\dot{Q}_o = \rho_m \dot{G}_m c_{p,av} \left(T_{m,o} - T_{m,i}\right) \tag{4.35}$$

$$\Delta\dot{Q} = 100 \times \left(\dot{Q}_i - \dot{Q}_o\right)/\dot{Q}_i \tag{4.36}$$

To evaluate the heat transfer rate for the CLTS, a system temperature difference was defined as the difference between the average plate temperature and the average condenser temperature (equation 4.39). To evaluate the difference in the plate temperatures for an experiment, the spread in the plate temperatures is indicated by S_+ and S_- (equation 4.40 & 4.41). The error bars shown in, e.g. Figure 4-10 (a), indicate the spread S_+ and S_-.

$$T_{h,ave} = \frac{1}{m}\sum_{n=1}^{m=3} T_{h,n} \tag{4.37}$$

$$T_{c,ave} = \frac{1}{m}\sum_{n=1}^{m=2} T_{c,n} \tag{4.38}$$

$$\Delta T_{sys} = T_{h,ave} - T_{c,ave} \tag{4.39}$$

$$S_+ = \left|\mathrm{MAX}\left(\left\{T_{h,n} - T_{c,av}\right\}\Big|_{n=1}^{m}\right) - \left(T_{h,av} - T_{c,av}\right)\right| \tag{4.40}$$

$$S_- = \left|\mathrm{MIN}\left(\left\{T_{h,n} - T_{c,av}\right\}\Big|_{n=1}^{m}\right) - \left(T_{h,av} - T_{c,av}\right)\right| \tag{4.41}$$

The evaporator and condenser inside heat transfer coefficients are calculated using equations (4.43) and (4.44), respectively.

$$A_{e,i} = \pi d_i L_e \tag{4.42}$$

$$h_{e,i} = \dot{Q}_i/\left(A_{e,i} \times \left(T_{h,av} - T_i\right)\right) \tag{4.43}$$

$$A_{c,i} = \pi d_i L_c \tag{4.44}$$

$$h_{c,i} = \dot{Q}_i \Big/ \left(A_{c,i} \times \left(T_{c,av} - T_i \right) \right) \tag{4.45}$$

The regression equations to be applied to the experimentally determined evaporator and condenser inside heat transfer coefficients are given by equations (4.46) and (4.47), respectively. Equation (4.46) was previously used by Meyer (2004). Equation (4.47) is based on equation (4.28), which was previously used by Meyer (2004). However, the Cond term in equation (4.28) was replace by FC term in equation (4.47). The film condensation (FC) is based on a Nusselt analysis of film condensation on the inside of a horizontal tube (Mills, 1998). Data used for the regression were while the CLTS experiment heat transfer rate increased linearly with temperature difference, and before maximum heat transfer rate was achieved.

$$h_{ei} = b \times Ja^{m1} Ku^{m2} d_i^{m3} \tag{4.46}$$

$$h_{ci} = b \times \mathrm{Re}_l^{n1} \mathrm{FC}^{n2} d_i^{n3} \tag{4.47}$$

where

$$Ja = c_{p,l} \left(T_w - T_{sat} \right) / h_{fg} \tag{4.48}$$

$$\mathrm{Re}_l = \frac{\rho V d_i}{\mu} = \frac{\rho \left(4\dot{m} / \rho \pi d_i^2 \right) d_i}{\mu} = \frac{4\dot{m}}{\pi d_i \mu} = \frac{4\dot{Q}/h_{fg}}{\pi d_i \mu} = \frac{4\dot{Q}}{\pi d_i \mu h_{fg}} \tag{4.49}$$

$$Ku = \dot{Q} \Big/ \left[\rho_v h_{fg} \left(\frac{\sigma g \left(\rho_l - \rho_v \right)}{\rho_v^2} \right)^{0.25} \right] \tag{4.50}$$

$$FC = \frac{g \rho_l \left(\rho_l - \rho_v \right) d_i^3 h_{fg}}{\mu_l k_l \left(T_{sat} - T_w \right)} \tag{4.51}$$

The Jakob number is the ratio of sensible to latent energy absorbed during the liquid-vapour phase change (Incropera and DeWitt, 2002). It, therefore, compares the maximum sensible heat, $c_p \Delta T$, absorded by the liquid to the latent heat absorbed (Lienhard and Lienhard, 2006). The Kutateladze number is a non-dimensionless heat flux rate. The Reynolds number is the ratio of the inertia and viscous forces (Incropera and DeWitt, 2002).

4.2.3. Processed CLTS data for R134a as working fluid

This section details the processed experimental results for the closed loop thermosyphon experiments using R134a as the working fluid. Note that the filling ratios referred to in this section are nominal filling ratios and not the actual filling ratios. Table 4-4 shows the actual FR for the CLTS R134a experiments. Figure 4-10 (a) shows the heat transfer characteristics of the experiments. It shows that using a larger diameter CLTS, increases the maximum heat transfer rate but decreases the thermal resistance. The latter can be see by the gradient of the experiments, were the lowest gradient (½" experiments) has the lowest thermal resistance. Although for the ¼" experiment a maximum heat transfer rate of 115 W was achieved, it is not useable since the plate temperature differences are too large for electronic cooling requirement.

Table 4-4: Actual fill ratio achieved for the R134a CLTS experiments compared to the nominal filling ratio

Nominal FR	FR 0.75	FR 0.5	FR 1
Experiment	Actual FR		
1/4" CLTS	0.61	-	-
3/8" CLTS	-	0.57	1.05
1/2" CLTS	-	0.50	0.93

The data used in the correlation of the ¼" experiment was for experiments less than 50 W. The heat transfer characteristic of the ⅜ experiments is similar below 100 W, thereafter it deviates. This can only be attributed to the fill ratio used for each experiment. Maximum heat transfer rate was also achieved for ⅜" FR 0.5 and 1 experiments, 209 W and 211 W, respectively. Maximum heat transfer rate was also achieved for ½" FR 0.5 and 1 experiments, 188 W and 280 W, respectively. Figure 4-10 (b) shows that the experiments achieved an energy balance of, on average, -10% to a maximum of -20%.

Figure 4-10 (c) and (d) show that the evaporator and condenser inside heat transfer coefficients increase and decrease with increasing power input, respectively. The

higher the heat flux rate in the evaporator, the higher the nucleate boiling and 'bubble pumping' effect and hence the higher the evaporator heat transfer rate. Liquid deposition on a surface creates a film which increases in thickness as the heat transfer rate increases. Due to the thermal resistance of the film, the condensation heat transfer coefficient decreases with increasing heat transfer rate. Figure 4-10 (e) and (f) show all the regression correlations used for the evaporator and condenser inside heat transfer coefficients, respectively. Figure 4-10 (g) and (h) show the best correlations for the evaporator and condenser inside heat transfer coefficients, respectively. The best correlations are given in Table 4-5. The correlations show that the inside heat transfer coefficients are dependent on the inside diameter of the CLTS. There was not a good correlation for the evaporator heat transfer coefficients using the Jakob, Kutateladze and diameter as the regression terms. Each CLTS diameter has its own evaporator heat transfer coefficient correlation. This can also be shown by noting the different behaviours of the evaporator heat transfer coefficients for the different diameters as shown in Figure 4-10 (c). The four left most data points in Figure 4-10 (h) correspond to the data points in (d) were the power input is below 25 W. The condensation correlation is therefore accurate to 20 % for power input below 25 W and 10 % above 25 W power input.

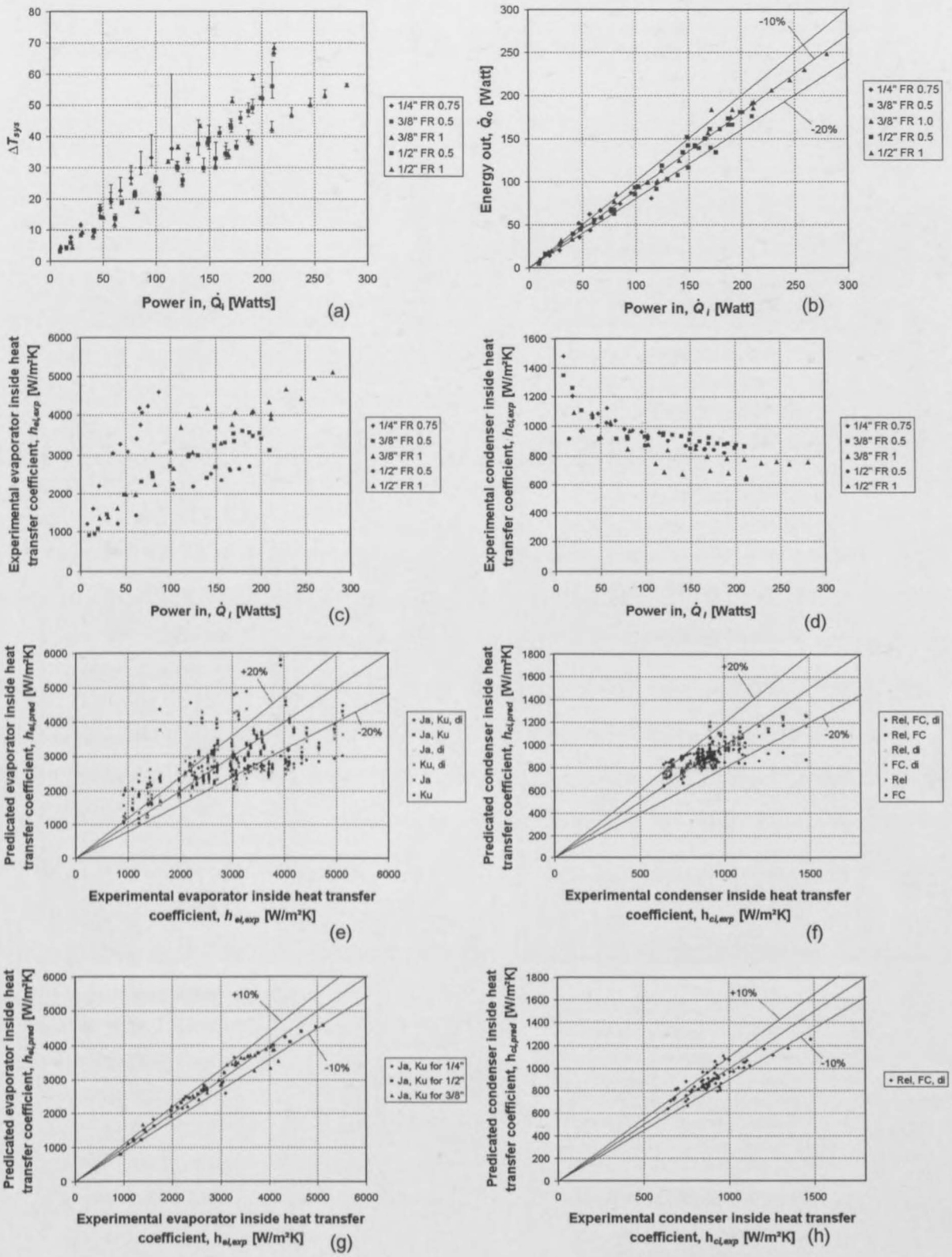

Figure 4-10: Heat transfer rate, energy balances and evaporator and condenser inside heat transfer coefficients, predicted and experimental, for CLTS with R134a as working fluid

Table 4-5: Regression coefficients for the evaporator and condenser inside heat transfer coefficients for CLTS with R134a as working fluid

Regression terms used	Ja, Ku for 1/4"	Ja, Ku for 1/2"	Ja, Ku for 3/8"	Regression terms used	Re_l, FC, d_i
b	76904.716	62677743	9948275	b	0.130240
m1	1.0587224	-0.98381	-0.61069	n1	0.007929
m2	-0.0137391	1.255909	0.946487	n2	0.258710
m3				n3	-0.984119
R^2	0.88	0.02	0.93	R^2	0.75
Average % difference	8.1	5.1	5.8	Average % difference	6.1
Maximum % difference	15.8	15.0	20.4	Maximum % difference	18.6

4.2.4. Processed CLTS data for butane as working fluid

This section details the processed experimental results for the closed loop thermosyphon (CLTS) experiments using butane as the working fluid. Note that the filling ratios used in this section are the nominal filling ratios and not the actual filling ratios. Table 4-6 shows the actual FR for the CLTS butane experiments. Figure 4-11 (a) shows the heat transfer characteristic of the experiments. It shows that using a larger diameter CLTS decreases the thermal resistance. This can be seen by the gradient of the experiments, where the lowest gradient (½" experiments) has the lowest or best thermal resistance.

Table 4-6: Actual fill ratio achieved for the butane CLTS experiments compared to the nominal filling ratio

Nominal FR	FR 0.75	FR 0.5	FR 1	FR 1.5
Experiment	Actual FR			
1/4" CLTS	0.86	-	-	-
3/8" CLTS	-	0.50	1.11	-
1/2" CLTS	-	0.57	1.00	1.31

The maximum heat transfer rate was not achieved for the butane experiments. The experiments were stopped when the system temperature difference, ΔT_{sys}, went above 70 °C, but average maximum temperature difference is around 80 °C. Figure 4-11 (b) shows that the experiments achieved an energy balance to a maximum of -

10%. Figure 4-11 (c) and (d) show that the evaporator and condenser inside heat transfer coefficients increase and decrease with an increasing power input, respectively. Figure 4-11 (c) shows that the evaporator inside heat transfer coefficients behave similarly, except for the ¼" experiment which is significantly higher than the other experiments. The higher evaporator inside heat transfer coefficients for the ¼" experiment is attributed to the fluid behaviour at small diameters. Figure 4-11 (e) and (f) show all the regression correlation results, while (g) and (h) show only best correlation results, for the evaporator and condenser respectively. The best correlation coefficients are given in Table 4-7.

Table 4-7: Regression coefficients for the evaporator and condenser inside heat transfer coefficients for CLTS with butane as working fluid

Regression terms used	Re_l, FC, d_i	Regression terms used	Ja, Ku, d_i
b	3.40459E-08	b	146192.4
n1	0.405281	m1	-1.03379
n2	0.621449	m2	1.287164
n3	-1.69608	m3	-1.32344
R^2	0.90298	R^2	0.982916
Average % difference	3.516666	Average % difference	4.495361
Maximum % difference	12.58395	Maximum % difference	14.91612

The experiment ½" CLTS FR of 1.5 was not correlated on its own or with other experiments. The condenser inside heat transfer coefficient behaves similarly when compared to the other experiments, as shown in Figure 4-11, but below 150 W the condenser heat transfer coefficient starts to decrease instead of increasing. When the FR is equal to 1.5, then the entire evaporator length is filled and excess liquid goes into the rest of the CLTS. When the power input and therefore also the mass flow rate is small, there is condensate in the condenser of the CLTS. This condensate hinders the condensation of vapour in the condenser. And therefore the condenser inside heat transfer coefficient decreases at low power input rates. Due to this decrease the experiment was not considered.

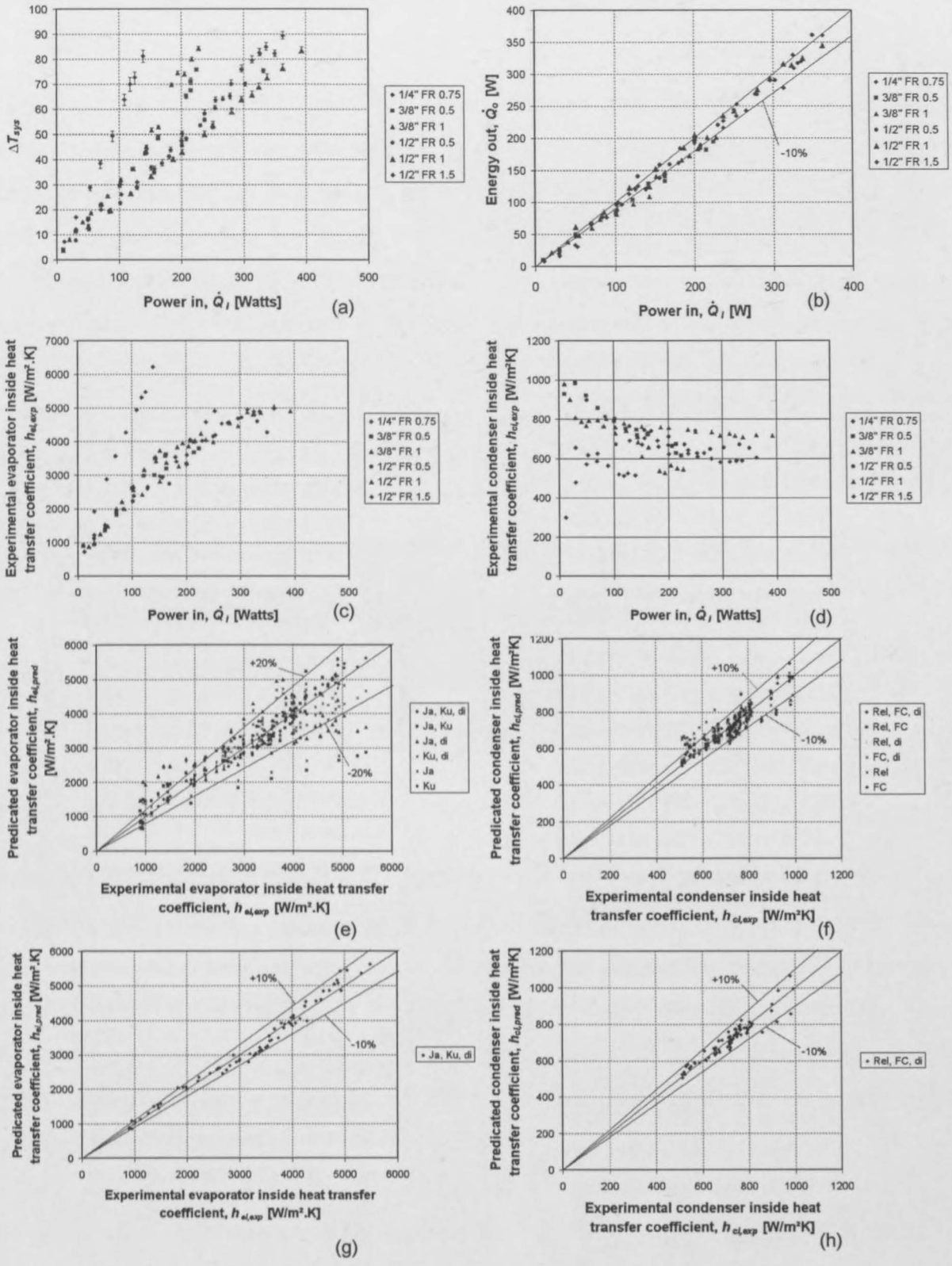

Figure 4-11: Heat transfer rate, energy balances and evaporator and condenser inside heat transfer coefficients, predicted and experimental, for CLTS with butane as working fluid

4.2.5. Processed CLTS data for water as working fluid

This section details the processed experimental results for the closed loop thermosyphon (CLTS) experiments using water as the working fluid. Note that the filling ratios used in this section are the nominal filling ratios and not the actual filling ratios. Table 4-8 shows the actual FR for the CLTS water experiments. Figure 4-12 (a) shows the heat transfer characteristic of the experiments. It shows that using a larger diameter CLTS decreases the thermal resistance. This can be see by the gradient of the experiments, were the lowest gradient (½" experiments) has the lowest or best thermal resistance. Figure 4-12 (b) shows that the energy balance did not exceed -10%.

Table 4-8: Actual fill ratio achieved for the water CLTS experiments compared to the nominal filling ratio

Nominal FR	FR 0.5	FR 1
Experiment	Actual FR	
3/8" CLTS	0.45	0.91
1/2" CLTS	-	1

Although the system temperature difference for ½" FR 1 experiment can be expected to go to zero for zero power input, the experiment ⅜" FR 1 does not do that. This behaviour can be explained by the decrease of the condenser inside heat transfer coefficient, as shown in Figure 4-12 (d), which is due to the excess working fluid hindering the condensation of vapour. The decrease in the condensate heat transfer of coefficient was also seen in the ½" FR 1.5 butane CLTS. Other FR 1 experiments did not show this behaviour.

When the FR is decreased to 0.5 for the ⅜" CLTS, the thermal resistance is decreased. However, a maximum heat transfer rate was achieved for this experiment. Also there was a minimum heat transfer rate for stable temperatures. For power inputs below 200 W, the temperatures did not reach a steady-state value and were therefore not recorded. A similar behaviour was seen with the ½" CLTS FR 1 experiment. The minimum power input for a stable temperature is 100 W. If the FR

for the ½" CLTS is decreased, it is suspected that the minimum power input will increase and there should be a decrease in the maximum heat transfer rate. ½" FR 1 and ⅜" FR 1 did not reach a maximum heat transfer rate (Table 4-10 on page 4-32). Note the plate temperature differences shown in Figure 4-12 (a) for ⅜" FR 0.5.

Table 4-9: Regression coefficients for the evaporator and condenser inside heat transfer coefficients for CLTS with water as working fluid

Regression terms used	Rel, FC for 1/2" FR 1	Rel, FC for 3/8" FR 1	Rel, FC 3/8" FR 0.5	Regression terms used	Ja, Ku, di for FR 1	Ja, Ku for 3/8" FR 0.5
b	1.945943	2.08729E+20	2.48233E-11	b	88746.24	458249.9882
n1	0.16668	0.77168	0.54325	m1	0.517576	1.659923881
n2	0.28176	-2.03320	1.39978	m2	-0.38885	-0.004934
R^2	0.92	1.00	0.93	m3	1.116521	
				R^2	0.861445	0.986627613
Average % difference	1.46	3.65	2.13	Average % difference	4.591665	0.976249633
Maximum % difference	3.60	9.30	3.47	Maximum % difference	10.83692	2.313380399

The evaporator inside heat transfer coefficients increase with increasing power input, however the condenser heat transfer coefficients decrease with increasing power input, as shown in Figure 4-12 (c) and (d). Figure 4-12 (e) and (f) show all the regression correlation results, while (g) and (h) show only best correlation results, for the evaporator and condenser respectively. The correlation coefficients are given in Table 4-9.

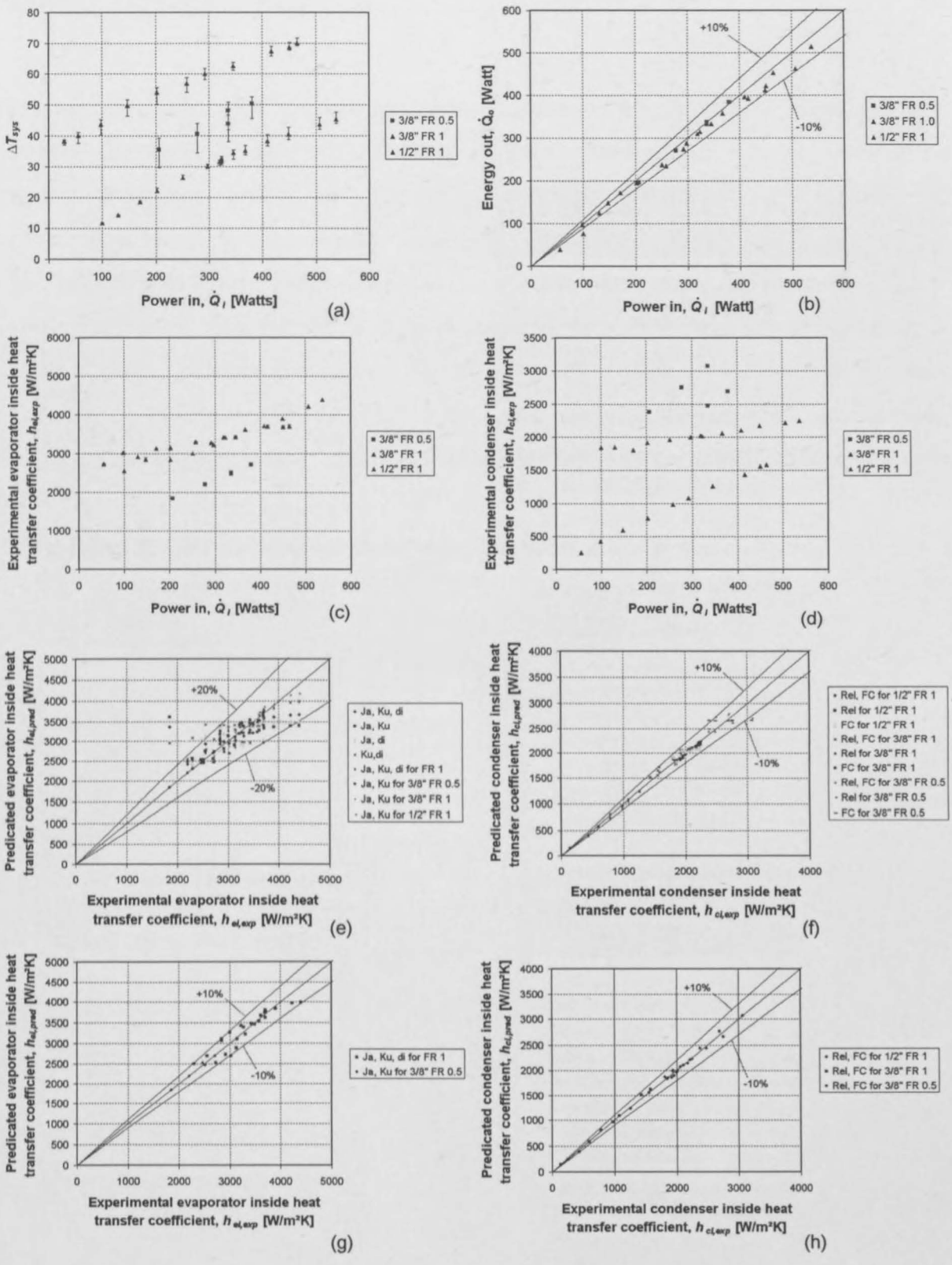

Figure 4-12: Heat transfer rate, energy balances and evaporator and condenser inside heat transfer coefficients, predicted and experimental, for CLTS with water as working fluid

4.2.6. Comparison of the CLTS working fluids

This section details the comparison between the different working fluids for the different diameters of the CLTS. Table 4-10 gives a summary of the maximum heat transfer rates and system temperature differences. Experiments using R134a as working fluid reached a maximum heat transfer rate, while butane experiments did not. This coincides with R134a having a lower FOM than butane, as shown in Figure 4-7 on page 4-16. The maximum heat transfer rate is also dependent on the fill ratio of the CLTS. This can be shown by the different maximum heat transfer rates achieved by the ⅜" water and ½" R134a experiments. Figure 4-13 shows and discusses the thermal resistances for different working fluid for specific diameters.

Table 4-10: Maximum heat transfer rates for correlations

		Maximum value		
CLTS diameter	Experiment	Heat transfer [W]	ΔT_{sys} [°C]	Limiting factor[3]
¼"	R134a FR 0.75	57.2[4]	19.0	HTR
	Butane FR 0.87	138.9	81.2	TD
⅜"	R134a FR 1	211.8	68.5	HTR
	R134a FR 0.5	209.9	56.0	HTR
	Butane FR 1	227.6	84.3	TD
	Butane FR 0.5	224.4	75.8	TD
	Water FR 0.5	380.3	51.9	HTR
	Water FR 1	465.1	70.1	TD
½"	R134a FR 0.5	187.5	39.5	HTR
	R134a FR 1	280.6	56.6	HTR
	Butane FR 0.5	350.3	82.1	TD
	Butane FR 1	393.4	83.4	TD
	Water FR 1	537.9	45.3	RC

[3] The experiment is limited by reaching a maximum heat transfer rate (HTR), exceeding a maximum temperature difference for ΔT_{sys} (TD) or limited by the resistors maximum power capacity (RC).

[4] The maximum heat transfer rate achieved was 114 W, resulting in ΔT_{sys} being 36°C. The value shown in Table 4-10 is the maximum value used for the correlations.

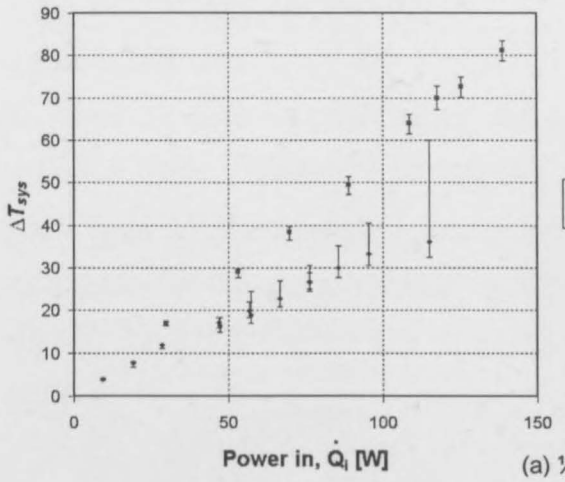

(a) ½" CLTS

R134a has a lower thermal resistance than butane, but has a maximum heat transfer rate of 114 W. Butane did not reach a maximum heat transfer rate for the experiments.

The plate temperature differences, shown by the 'error' bars in the graph, can be decreased by adding a heat pipe to the evaporator plates. This will be discussed in more detail in section 4.2.7.

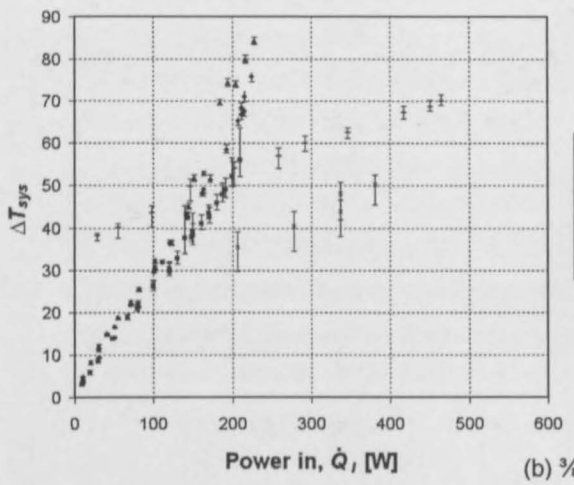

(b) ⅜" CLTS

Butane and R134a have similar thermal resistances, but higher than the water FR 0.5 experiment. Water FR 0.5 has a minimum power input to achieve stable evaporator plate temperatures. Water FR 0.5 and R134a experiments have reached maximum heat transfer rates.

Water FR 1 can achieve heat transfer rates of 400 W and higher, but has higher thermal resistance at R134a and butane below 200 W.

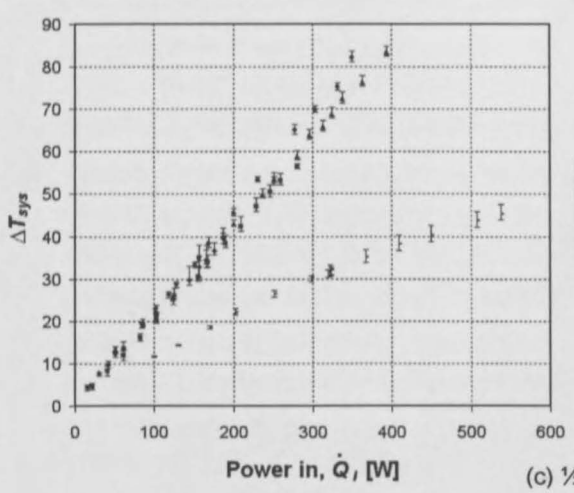

(c) ½" CLTS

Butane and R134a have similar thermal resistances, but are significantly lower than water FR 1. R134a has reached a maximum heat transfer rate, while water FR 1 was limited by the power input capacity of the resistors.

Figure 4-13: Comparison of the heat transfer rates for different diameters and working fluids for the CLTS experiments

Figure 4-10 (c) shows that for the R134a experiment, the evaporator inside heat transfer coefficients are more scattered than for the butane experiments, Figure 4-11 (c). The heat transfer coefficients for the ¼" CLTS are higher than for the other diameters. The evaporator heat transfer coefficients for the R134a, butane and water experiments increase as the power input increases. The condenser heat transfer coefficients for the water experiments increase with increasing power input (Figure 4-12 (d)). This is different when compared to the decreasing condenser heat transfer coefficient for increasing power input for the R134a and butane experiments.

4.2.7. Discussion and conclusions

The experimental set up, procedure and processing procedure for experiments conducted on the closed loop thermosyphon (CLTS) have been documented. R134a, butane and water have been tested with varying fill ratios. Each working fluid has been discussed separately and then compared to each other for different CLTS diameters.

Since the heat transfer rate required is 320 W, multiple ¼" and ⅜" butane and R134a CLTS can be used. ⅜" water FR 0.5 CLTS can transfer the energy required at around a 45°C system temperature difference. An additional heat pipe will need to be used to decrease the plate temperature differences. However, ½" water FR 1 CLTS will be able to do it in 35°C system temperature difference. ½" Butane can transfer the energy, but at a 75°C system temperature difference. ½" R134a cannot transfer 300 W.

It is difficult to get a purged ¼" CLTS to specific fill ratio. This was because the ¼" CLTS has a very small volume to be filled. Care must be taken when filling the ¼" CLTS due to deformation when overfilling it with R134a and butane. No deformation occurred with the ⅜" and ½" CLTS.

The relatively large temperature spread in the evaporator plate is an indication of a non-uniform heat transfer rate along the CLTS evaporator, such as in the ¼" R134a FR 0.75 and ⅜" water FR 0.5 experiments. Heat pipes can be used to create a more

uniform heat transfer rate along the evaporator. This will then decrease the evaporator temperature spread. The heat pipes can be mounted in the CLTS evaporator plates, parallel to the evaporator. The heat transfer characteristics of the heat pipe CLTS configuration will have to be experimentally determined.

Note that when the BTS and CLTS were tested, the plate heat spreaders were placed 1 to 2 mm apart. Practical designs would have the plates connected to each other. This would result in conduction between the different plates. A reduction in the plate temperature spread will occur in this case.

When the water CLTS was tested, a vibration was felt in the CLTS. It started when the water started boiling and reduced when a steady-state temperature had been achieved. A 'kick in' or start up vibration is typical for water filled thermosyphons. This occurs due to the high surface tension and liquid-vapour density differences of water. This causes bubbles to form which rapidly expand inside the thermosypshon. Water filled CLTS would not be recommended for components which are sensitive to vibration induced electronic noise, like pisoelectric effect and crystal containing components.

4.3. Discussion, conclusion and recommendation

Alternate HPA cooling solutions have been evaluated. It was estimated that the plate temperature for the original HPA cooling solution transistors is around 65 °C. In comparison, a CLTS LRU design will allow a transistor mounting base temperature of between 0 to 40 °C. The temperature will depend on the CLTS configuration used, the cold plate design and the cooling fluid temperature and mass flow rate. The CLTS design has a cooling fluid temperature independent of the system container temperature.

Correlations for the CLTS evaporator and condenser inside heat transfer coefficients were generated. It was only possible to get a single correlation for the evaporator inside heat transfer coefficient and another for the condenser coefficient for the butane CLTS experiments. The 3 evaporator correlations for R134a are for each

diameter, while each water filled configuration tested had its own evaporator and condenser correlations. Therefore, it is concluded that it is not possible to get a single correlation that will give an accurate prediction of the evaporator or condenser inside heat transfer coefficients for all the CLTS tests conducted.

The BTS heat transfer limit is less than 200 W when using R134a as working fluid. A CLTS can transfer in excess of 500 W when water is used as the working fluid. The recommended solution for an alternative HPA cooling solution is the use of a ½" FR 1 water CLTS. The temperature and flow rate of the refrigerant or water is dependent on the cold plate design and the total heat transfer rate required. It is recommended that the condenser length be increased, since the condensation heat transfer coefficient is low. Increasing the condenser length will also allow a larger cold plate to be used, which will result in a lower thermal resistance for the cold plate. A proposed HPA unit CLTS LRU design is shown in Figure 4-14. The LRU is bolted to the refrigerant or water cooled cold plate from the outside of the unit.

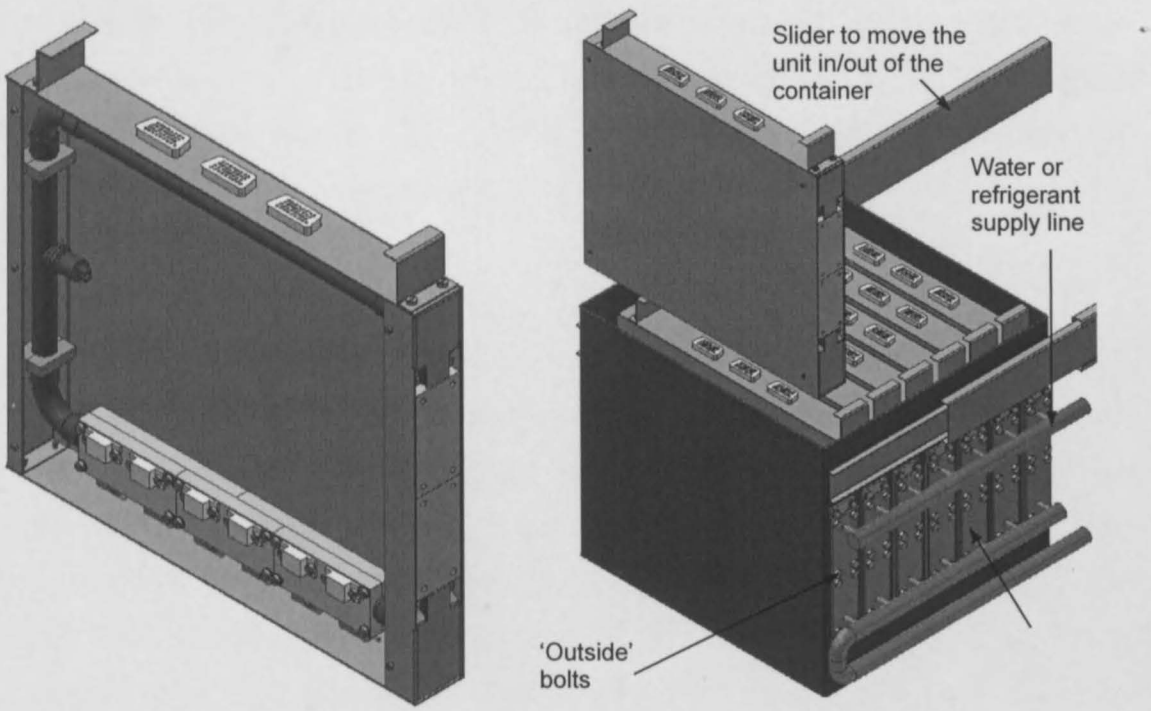

Figure 4-14: A proposed HPA unit LRU design.

LRUs are by definition line replaceable units. If one of the units becomes faulty or damaged, that can be replaced quickly. Designing with a LRU allows the designer to have fewer redundant units, since the units can be replaced quickly. One must however be careful when using a LRU design. Energy dissipated by the components inside the LRU must still be transferred to the environment through an interface.

An advantage that a thermosyphon has over a heat pipe is that the former has a lower thermal resistance than a heat pipe of the same diameter. This is because a heat pipe has a wick or porous material on the inside. The wick or porous material allows the working fluid to use surface tension driven capillary action to allow the flow of condensate against gravity. This then enables the heat pipe to transfer heat energy against gravity. The wick or porous material is still a material and therefore also has a resistance to heat transfer. Thermosyphons must work with gravity and therefore are more orientation dependent than heat pipes.

Another advantage of thermosyphons is that it is easier to manufacture than heat pipes. For South Africa, this means that thermosyphons can be easily manufactured locally. The cost and time to manufacture is therefore dependent on the facilities available. Heat pipes would need to be specified and manufactured abroad. Exchange rates and shipping costs would be significant factors in the overall cost of the heat pipes.

Testing a heat pipe or thermosyphon for electronic cooling should be done using plate heat spreaders with resistors mounted on them. When a themosyphon or heat pipe reaches its maximum heat transfer rate, the heat flux in a region of the evaporator decreases. When resistors are used, the heat flux to the heat pipe remains constant. Thus when the maximum heat transfer rate is achieved, the evaporator temperature increases uncontrollably. If however the energy is added by a tube-in-tube type heat exchanger, the heat transfer takes place over a smaller area. The overall effect will be a non-linear increase in the temperature difference between the condenser and evaporator. However, the uncontrollable temperature increase will not occur. A heat exchanger determined maximum heat transfer rate will therefore differ to a maximum heat transfer rate determined by plate mounted resistors.

As stated in point 12 (on page 4-5) of the CSLD for the CLTS and BTS HPA LRU designs, the energy gain by the refrigeration unit needs to be dissipated to the environment. It is possible that this final point may be overlooked in the system design. This may result in the condenser of the refrigeration units being placed, for example, next to the diesel generator. By doing the CSLD the designer will be aware of point 12. A proposed condenser configuration is shown in Figure 4-15. The air enters and leaves the condenser without interacting with the system container air. The condenser is also insulated from the rest of the system.

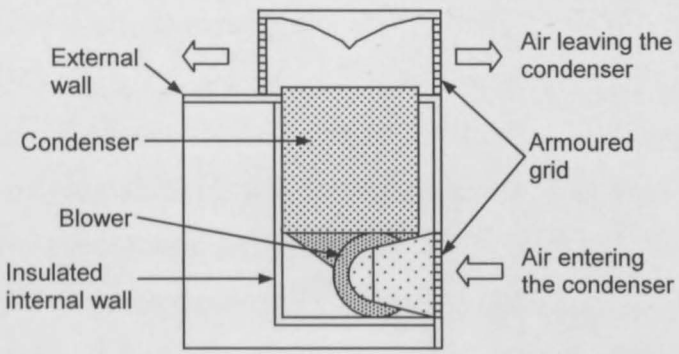

Figure 4-15: Proposed condenser configuration

Chapter 5 Conclusion

This thermal management project arose from the thermal problems encountered with the ESR 220 radar system (Kameelperd). The transistors in the high power amplifier (HPA) fail due to thermal shock resulting from rapid cooling when not transmitting and excessively high temperatures at high system container temperatures. In order to prevent the excessively high transistor temperatures the system container temperature is uncomfortably low for the personnel in the system container. The four processors in the digital signal processor (DSP) exceed their temperature specifications if the DSP fans are switched off.

Having set up a thermal management process in Chapter 2, it is applied to the radar system. From the cooling solution level definitions analysis of the radar system it was found that the thermal problems encountered relate to the HPA transistor cooling solution employed in the radar equipment container (REC) and the cooling solution's interaction with the rest of the system. The existing cooling solution consists of fins sintered to an aluminium plate and onto which the transistors are bolted. A blower is mounted in the HPA, which provides air flow through the fins. A numerical model, using experimental data, estimated that under non-failure condition the plate temperature is approximately 65 °C.

The interaction of the cooling solution with the rest of the radar system limits the air flow through the REC. The CFD analysis of the REC showed that the inappropriate positioning and configuration of the various units in the REC not only limits the total air flow rate through the container, but also inhibits the distribution of air to the DSP processors. Changes to the REC have been recommended and discussed in section 3.5.

The transistor base temperature limit of 65 °C has been calculated using a numerical analysis of the original HPA cooling solution. A closed loop thermosyphon (CLTS) line replaceable unit (LRU) design is the proposed alternative HPA cooling solution. The CLTS uses a ½" CLTS filled with water, to a fill ratio of 1. Various cooling solution concepts were evaluated, including a bent thermosyphon (BTS), but the

CLTS design was the solution selected. The proposed solution can achieve a transistor base temperature below the numerically determined temperature limit. The transistor temperatures are dependent on the cold plate design, the water or refrigerant temperature and the flow rate of the CLTS LRU design. A discussion of the BTS and CLTS experiments, and recommendations for the CLTS design has been discussed in section 4.3.

It is concluded, finally, that the thermal management design process methodology must be implemented from the beginning of the procurement process so that the thermally associated risk of the product would have been significantly reduced, if not eliminated.

Chapter 6 References

Belady, C., June 2001, *Effective thermal design for electronic systems*, Hewlett-Packard company, http://www.coolingzone.com [13 August 2005].

Dul, J. and Weerdmeester, B., 2001, *Ergonomics for beginners: A quick reference guide*, Second edition, Taylor and Francis, London.

Faghri, A, 1995, *Heat pipe science and technology*, Taylor & Francis, London.

Gelbart, M, 2004, *Modern Israeli Tanks and Infantry Carriers 1985 - 2004*, Osprey Publishing, Oxford.

Graham, A., 2007, Private communications.

Imura, H. and Ippohshi, S., 2000, *Heat transfer characteristics in two-phase crank-shaped closed loop thermosyphons*, Proceedings of the 6th International Heat Pipe Symposium, Chiang Mai.

Incropera, F.P. and DeWitt, D.P., 2002, *Fundamentals of heat and mass transfer*, Fifth edition, John Wiley and Sons.

Ippohshi, S., Tabvara, S., Motomatu, K., Mutoh, A. and Imura, H., 2003, *Development of a top-heat-mode loop thermosyphon*, 6th ASME-JSME Thermal engineering joint conference, 16-20 March 2003.

Jeggels, Y.U., 2007, *Thermal management design process for electronic equipment*, unpublished.

Jeggels, Y.U. and Dobson, R.T., 2007, *Improving thermal contact resistance: A case study.*

Jeggels, Y.U., 2006, *Thermal management and temperature control of a containerised rapid deployment radar system: Project proposal report*.

Kraus, A.D. and Bra-Cohen, A., 1983, *Thermal analysis and control of electronic equipment*, McGraw-Hill, New York.

Kordyban, T, 1998, *Hot air rises and heat sinks: Everything you know about electronic equipment is wrong*, ASME Press, New York.

Lemmon, E.W., McLinden, M.O., and Friend, D.G., "Thermophysical Properties of Fluid Systems" in NIST Chemistry WebBook, NIST Standard Reference Database Number 69, Eds. P.J. Linstrom and W.G. Mallard, June 2005, National Institute of Standards and Technology, Gaithersburg MD, 20899 (http://webbook.nist.gov).

Lienhard, J.H., and Lienhard, J.H., 2006, *A heat transfer textbook*, Third edition, Philogiston Press, Cambridge Massachusetts (http://web.mit.edu/lienhard/www/ahtt.html).

Meyer, A., 2004, *Development of a range of air-to-air heat pipe heat recovery heat exchangers*, Mechanical Engineering Department, Stellenbosch University.

Mills, A.F., 1998, *Heat Transfer*, Prentice-Hall, New Jersy.

Minichiello, A. and Belady, C., 2002, *Thermal design methodology for electronic systems*, 2002 Inter Society Conference on Thermal Phenomena.

Miyasake, A., Nakajima, K. and Tsunoda, H., 1995, *Experimental results for capillary looped pipe applied to direct cooling method*, Journal of Thermophysics and Heat Transfer, Vol. 9, No. 1, January – March 1995, p 96-100.

Papst, undated, "KAT_01GB.pdf", http://www.papst.de. [8 December 2004]

Philips, 1997, RX1214B170W datasheet, http://www.datasheetarchive.com/RX1214B170W-datasheet.html [1 November 2007].

Remsburg, R., 2001, *Thermal design of electronic equipment*, CRC Press, New York.

RRS website, 2007, http://www.rrs.co.za/products/2d-surveillance.htm [4 June 2007].

Sergent, J.E. and Krum, A., 1998, *Thermal management handbook for electronic assemblies*, McGraw-Hill, New York.

Steinberg, S.D., 1980, *Cooling techniques for electronic equipment*, Wiley & Sons, New York.

Yeh, L and Chu, R.C., 2002, *Thermal management of mircoelectronics equipment*, ASME Press, New York.

Appendix A Data DVD

In this section, the data DVD is contained. The DVD contains the calculations (using MS Office Excel and MATLAB), correspondence, documentation (Thesis report, proposal report and the thermal management design process in MS Office WORD and Adobe PDF format), drawing files (Autodesk INVENTOR 9 Professional, also in Adobe PDF and SAT file formats), experimental data, Flomerics' FLOTHERM results, literature and pictures accumulated and used during the project.

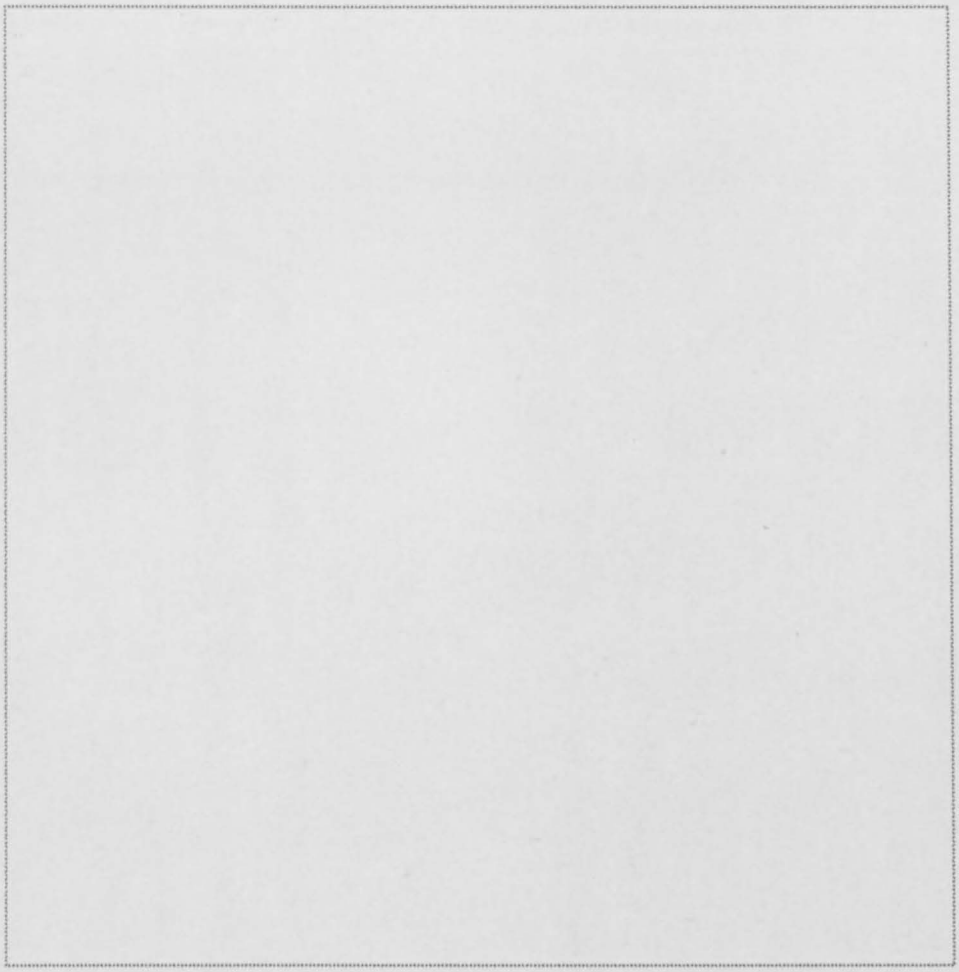

Appendix B Support material figures for the TMDP

This section shows the figures for the TMDP logic flow diagram, Figure B-1, and an example of the cooling solution level definition breakdown, Figure B-2. Both these figures are an important part of the thermal management design process. The TMDP logic flow diagram starts at the 'perform circuit analysis' process and finishes by the 'solution' block.

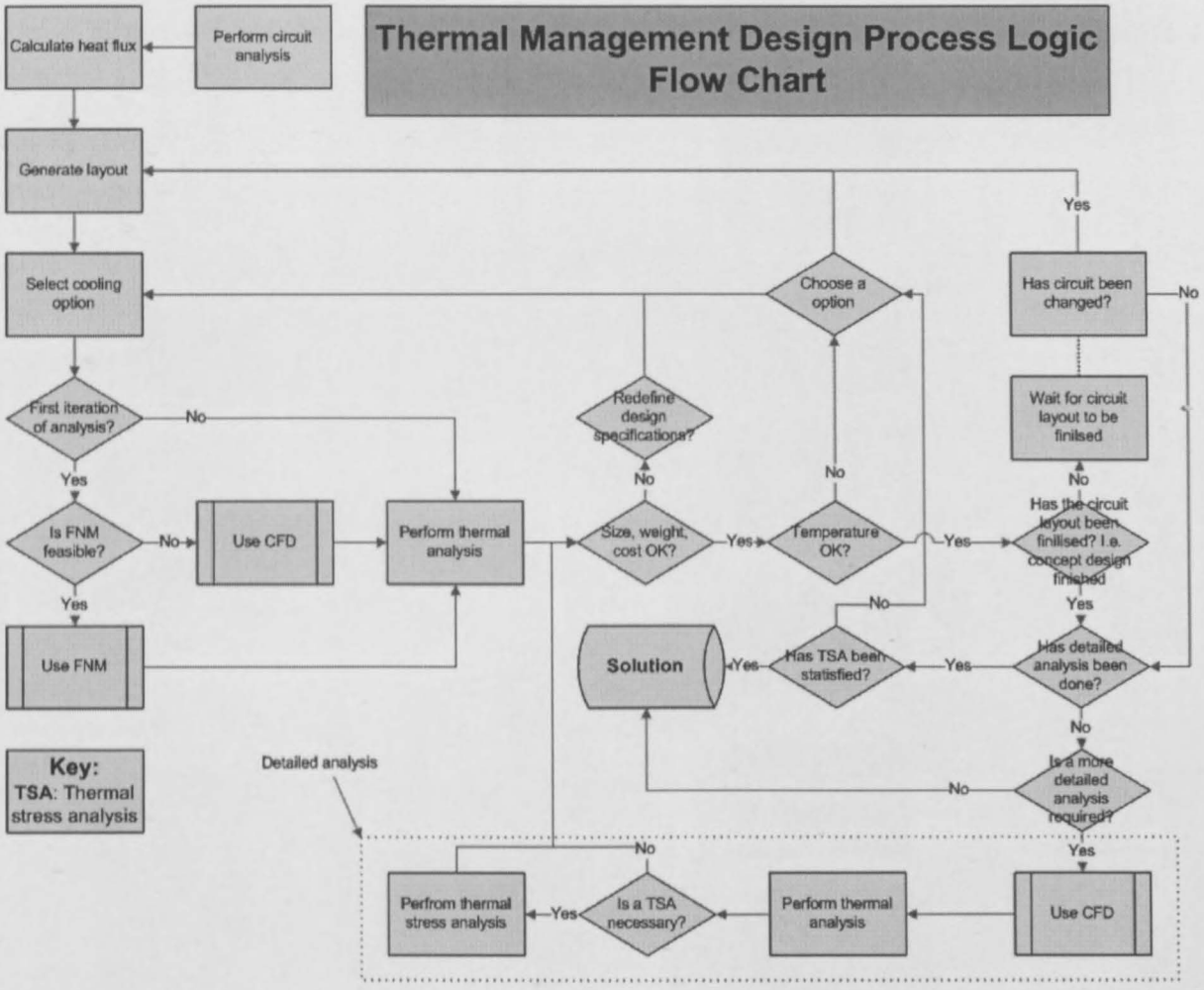

Figure B-1: Thermal management design process logic flow chart, based on the thermal design process by Sergent and Krum (1998)

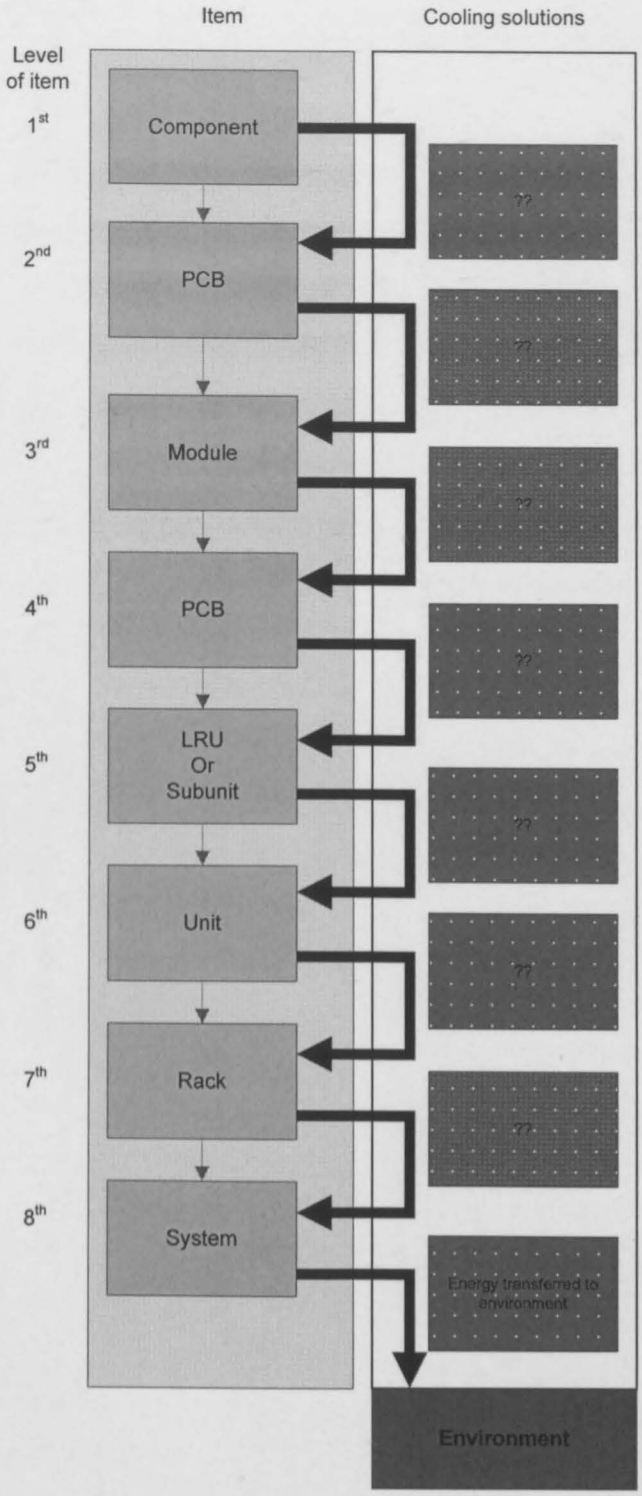

Figure B-2: An example of cooling solution system level (CSLD) (Jeggels, 2007)

Appendix C Additional data for Chapter 3

This section gives the measured experimental values for the data used in the FLOTHERM simulation of the radar equipment container.

Appendix C.1 Experimental data for the air flow through the detection processor of the digital signal processor

A AIR FLOW TA-5 (Bat no.: 315473) hot wire anemometer was used to measure the velocity of the air above and below the DSP estimation processor's heat sink. The measured data are given in Table C-1, while the processed results are given in section 3.1.3 on page 3-6.

Table C-1: Measured experimental data used to estimate the air flow through the detection processor of the digital signal processor

Position	Below the DSP		Above the DSP	
Measured	Temp [°C]	Velocity [m/s]	Temp [°C]	Velocity [m/s]
	15.4	0.61	18.1	0.66
	15.4	0.61	18.1	0.66
	15.4	0.64	18.1	0.66
	15.4	0.54	18.1	0.67
	15.5	0.94	18.1	0.67
	15.5	1.03	18.2	0.67
	15.5	1.03	19.6	1.49
	15.5	1.09	19.6	1.49
	15.6	1.16	19.5	1.4
	15.6	0.89	19.5	1.17
	15.7	0.82	19.5	0.92
	15.7	0.82		
	15.7	0.81		
	15.7	0.81		
	15.7	0.84		
	15.7	0.89		
	15.7	0.89		
	15.7	0.95		

Appendix C.2 Experimental data for the exit air flow rate of the REC

A AIR FLOW TA-5 (Bat no.: 315473) hot wire anemometer was used to measure the velocities above the 3rd subunit from the right and left, as shown in Figure 3-2 on page 3-4. The velocity was measured directly above the exit, with the anemometer horizontal and the anemometer tip vertical. This was done to get the best possible velocity. Table C-2 gives the velocities and temperatures measured, as well as the processed air flow rate.

Table C-2: Experimental data for the exit air flow rate of the REC

Position	3rd subunit from right		3rd subunit from left	
Measured	Temp [°C]	Velocity [m/s]	Temp [°C]	Velocity [m/s]
	24.3	3.87	23.1	3.8
	24.5	4.48	23.2	3.82
	24.5	3.62	23.2	3.81
	24.5	3.86	23.2	4.33
	24.5	4.34	23.2	4.31
	24.5	4.14	23.2	3.8
	24.5	4.23	23.2	4.27
	24.5	4.09	23.2	4.5
	24.5	3.65	23.2	4.42
	24.5	3.65	23.2	4.4
	24.6	4.83	23.2	4.4
	24.6	4.83	23.2	4.33
	24.8	4.94	23.2	4.32
	24.8	4.94	23.2	3.55
	25	4.65	23.2	4.02
	25	4.65	23.3	4.38
			23.4	4.32
			23.4	3.87
			23.6	4.33
			23.7	4.21
			23.7	4.2
			23.8	3.48
Average value	24.6	4.298125	23.30909	4.130455
Area [m²]		0.0037		0.0037
Flow rate, G [m³/s]		0.015903		0.015283
Average flow rate, G [m³/s]	0.155929			

Appendix C.3 EMI shield pressure loss coefficient calculation

This section details the calculation method, figures and tables used in the calculation of the EMI shield pressure loss coefficient. Table C-3 comes from Sergent and Krum (1998). It was used to determine the pressure lost coefficient for the flow through the EMI filter at the bottom of the radar equipment container. Although data in the Table C-3 is not exactly like the EMI shield configuration, it was however the closest that could be found in general literature.

Table C-3: Pressure loss coefficient K for flow through a thin-walled grid (l/D_h < 0 – 0.015) with sharp-edged orifice of different shapes (Sergent and Krum, 1998).

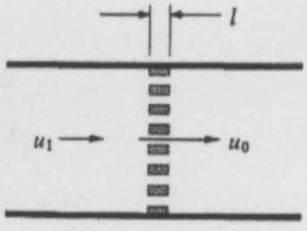

$$K = \frac{\Delta p}{1/2 \rho u_1^2}$$

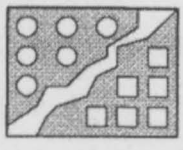

A_0 = area of one orifice
A_1 = area of upstream duct
P_1 = perimeter of upstream duct

$$D_h = \frac{4A_0}{P_1} \qquad \frac{F_0}{F_1} = \frac{\sum A_0}{A_1} \qquad \mathrm{Re}_{Dh} = \frac{u_0 D_h}{\nu}$$

	Re_{Dh}							
F_0/F_1	100	200	400	1,000	2,000	4,000	10,000	20,000
0.20	41.8	38.3	37.8	36.2	36.8	37.8	41.2	43.8
0.30	15.7	14.1	13.3	13.2	13.4	13.8	14.8	15.8
0.40	6.86	5.96	5.54	5.55	5.73	5.89	6.47	6.92
0.50	2.96	2.44	2.32	2.40	2.56	2.68	3.04	3.28
0.60	1.33	1.12	1.08	1.14	1.23	1.30	1.50	1.61
0.70	0.61	0.53	0.50	0.55	0.59	0.62	0.71	0.78
0.80	0.26	0.22	0.22	0.24	0.25	0.27	0.31	0.34
0.90	0.09	0.07	0.06	0.07	0.08	0.08	0.10	0.10
0.95	0.02	0.02	0.02	0.03	0.03	0.03	0.04	0.04

Figure C-1 (a) shows the dimensions and layout of the holes measured from the REC EMI shield, while (b) shows two drawings of a ¼ EMI shield. For computational purposes on a ¼ model was used. The area of the upstream duct A_1 was chosen as the area inside the dotted square in Figure C-1 (b). Areas A_1 and $\sum A_0$ were calculated from the CAD drawings.

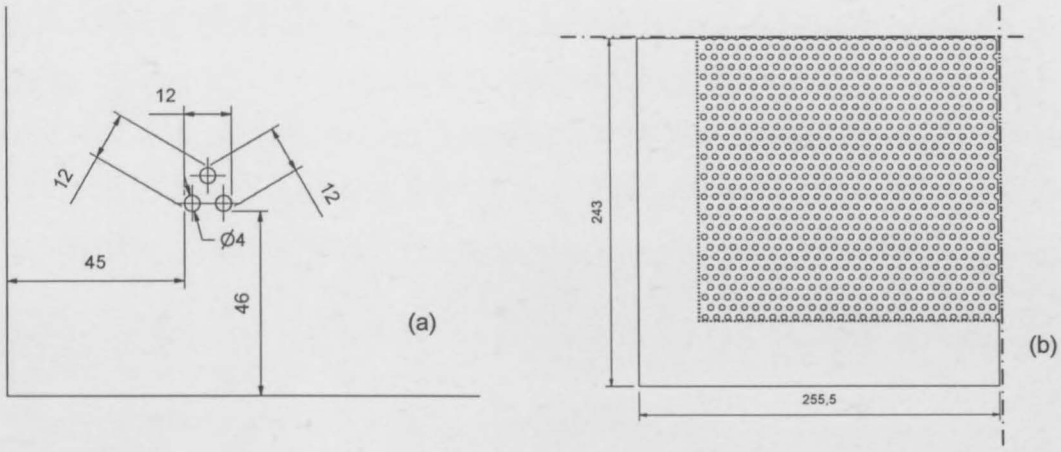

Figure C-1: Sketches used for the calculation of the pressure loss coefficient of the EMI shield

The diameter of the hole in equation (C.1) is used to calculate the area of the hole in equation (C.2). From the CAD drawing, the total flow area is given by equation (C.3), while the upstream flow area is given by equation (C.4). The velocity through the EMI shield can be calculated using equation (C.5). The equations used to calculate Re_D and F_0/F_1 are shown in the Table C-3.

$$D_h = 4 \times 10^{-3} \text{ m} \tag{C.1}$$

$$A_0 = \pi D_h^2 / 4 \tag{C.2}$$

$$\sum A_0 = 0.0373 \text{ m}^2 \tag{C.3}$$

$$A_1 = 0.16587 \text{ m}^2 \tag{C.4}$$

$$\dot{G} = u_0 \sum A_0$$
$$\therefore u_0 = \dot{G} / \sum A_0 = 4.02 \text{ m/s} \tag{C.5}$$

$$\begin{aligned} Re_D &= \rho D_h u_0 / \mu_0 \\ &= \frac{1.177 \times 4 \times 10^{-3} \times 4.02}{18.87 \times 10^{-6}} \\ &= 1003 \end{aligned} \tag{C.6}$$

$$\frac{F_0}{F_1} = \frac{\sum A_0}{A_1} = 0.225 \tag{C.7}$$

Defining x_i as independent and y_i as dependent variables, equation (C.8) is used to calculate the y_n value at x_n, assuming linear interpolation between x_1 and x_2. Table C-4 shows the results for the linear interpolation for the calculation of the pressure loss coefficient K at the Re_D and F_0/F_1 values calculated in (C.6) and (C.7), using linear interpolation equation (C.8). The pressure loss coefficient is calculated as 30.

$$y_n = \frac{(y_2 - y_1)}{(x_2 - x_1)}(x_n - x_1) + y_1 \text{ where } x_1 < x_n < x_2 \qquad (C.8)$$

Table C-4: Calculation of the pressure loss coefficient K from the calculated Re_D and F_0/F_1 values

	Re_D			
F_0/F_1	1000	1003	2000	
0.2	36.2	36.20	36.8	Calculated
0.225		30.45		Table data
0.3	13.2	13.20	13.4	

Similarly, with an EMI shield of 4 mm holes with 0.3 mm between them, results in a K value equal to 0.35, as shown in Table C-5. ($\sum A_0$ = 0.125 m², u_0 = 1.2 m/s, Re_D = 299.6, F_0/F_1 = 0.757.)

Table C-5: Calculation of the pressure loss coefficient K from the calculated Re_D and F_0/F_1 values

	Re_D			
F_0/F_1	200	299.6	400	
0.7	0.53	0.5233	0.5	Calculated
0.757		0.3504		Table data
0.8	0.22	0.2200	0.22	

Appendix C.4 Finite difference approximation of the Fourier's law for heat conduction

The phenomenological law governing heat flow in a solid object is Fourier's law of heat conduction, which states that in a homogeneous substance, the local heat flux is proportional to the negative of the local temperature gradient (Mills, 1998):

$$\frac{\dot{Q}}{A} = \dot{Q}'' \text{ and } \dot{Q}'' \propto -\frac{dT}{dx} \tag{C.9}$$

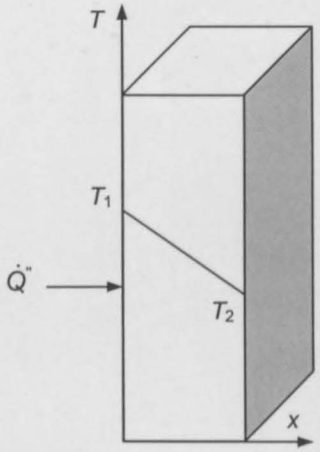

Figure C-2: One dimensional heat transfer by conduction (Incropera and DeWitt, 2002)

Where $\dot{Q}''$ is the heat flux, or heat flow per unit area perpendicular to the flow direction, T is the local temperature, and x is the coordinate in the flow direction (Mills, 1998). Introducing a constant of proportionality k,

$$\dot{Q}'' = -k\frac{dT}{dx} \tag{C.10}$$

Where k is the thermal conductivity of the substance. Therefore the heat transfer rate across an area A is:

$$\dot{Q} = -kA\frac{dT}{dx} \tag{C.11}$$

For the nodal network shown in Figure C-3, the finite difference approximation for the temperature gradient between node m and m+1 is:

$$\left.\frac{\partial T}{\partial x}\right|_{m+1/2,n} \approx \frac{T_{m+1,n} - T_{m,n}}{\Delta x} \tag{C.12}$$

Similarly, for the temperature gradient between node m and m-1 is:

$$\left.\frac{\partial T}{\partial x}\right|_{m-1/2,n} \approx \frac{T_{m,n} - T_{m-1,n}}{\Delta x} \tag{C.13}$$

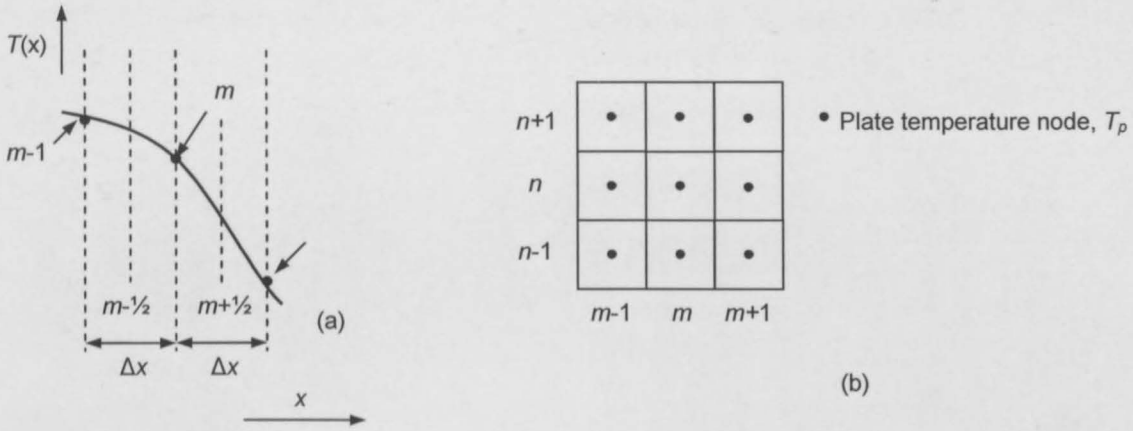

Figure C-3: Finite difference approximation (a) and Nodal network (Incropera and DeWitt, 2002)

Therefore the heat transfer rate from node m+1 to node m can be approximated from equations (C.11) and (C.12) as:

$$\dot{Q}_{(m+1,n)\to(m,n)} = kA\frac{T_{m+1,n} - T_{m,n}}{\Delta x} \tag{C.14}$$

Where $A = \Delta x \Delta z$ (C.15)

Equation (C.14) assumes that the temperature at node m+1 is greater than the temperature at node m. Similarly for the other nodes, the heat transfer rate for each node can be calculated.

Appendix D Subunit bench test measured and processed data

Table D-1 shows the measured and processed data for the subunit bench test. The equations used to process the data are discussed in section 3.4.1. The table comes from MS Office Excel spread sheet 'rec data 3.xls', which is provided on DVD Appendix A.

Table D-1: Raw data and worked data for the subunit bench test

Distance from edge	Distance	Vertical height, h_n	Area, A_n	V_1	V_2	V_3	V_{av}	m
[mm]	[mm]	[mm]	[m²]	[m/s]	[m/s]	[m/s]	[m/s]	[kg/s]
0	0	0	0	0	0	0	0.00	0
65	65	81	0.001053	2.48	2.47	2.48	2.48	0.003024852
97	32	32	0.000416	2.82	2.83	2.85	2.83	0.001367096
129	32	31	0.000403	2.75	2.74	2.75	2.75	0.001283864
159	30	30	0.00039	2.72	2.72	2.72	2.72	0.001230387
189	30	28	0.000364	2.42	2.42	2.37	2.40	0.001014667
215	26	26	0.000338	2.58	2.59	2.65	2.61	0.001021905
241	26	30.5	0.0003965	3.51	3.49	3.48	3.49	0.001606539
276	35	52.5	0.0006825	2.93	2.93	2.92	2.93	0.002316776
311	35	0	0	0	0	0	0.00	0
	311	311	0.004043					0.012866087

Width	Total flow area		Total mass flow rate	Average, av. velocity	Density
[mm]	[m²]		[kg/s]	[m/s]	[kg/m³]
13	0.004		0.0128661	2.78	1.159866923

Distance from edge	Displacement from edge	Vertical height	Area	m	Tmo	Q	dT	Displacement from edge
[mm]	[mm]	[mm]	[m²]	[kg/s]	[°C]	[W]	[°C]	[m]
0	0	0	0	0	0	0	0	0
65	65	97	0.001261	0.004	35.20	78.796459	19.50	0.065
64	129	62	0.000806	0.0026	37.60	56.563485	21.90	0.129
60	189	56	0.000728	0.0023	44.80	67.88618	29.10	0.189
52	241	96	0.001248	0.004	36.40	82.783148	20.70	0.241
70	311	0	0	0	0	0	0	0.311
311		311	0.004043	0.0129		286.02927		

Tinlet	Specific heat	Tav [K]	**Total heat transferred to air, Qt**
15.70	1006.964756	300.25	**[W]**
			286.03

Appendix E Regression coefficients for bent thermosyphon experiments

The experimental set up, procedure and results of the bent thermosyphon (BTS) experiments have been discussed in section 4.1 on page 4-6. This section gives the regression coefficients for the evaporator and condenser inside heat transfer coefficient correlations. The coefficients were determined using the 'data regression' tool in MS Excel. The experimental data used in the determination of the regression coefficients are given in Appendix A on the data DVD in the file 'large standard bent thermosyphon r134a charts.xls'.

Table E-1: Regression coefficients for BTS 90° FR 1

	Regression hei			Regression hci		
Regression terms used	Ja, Ku	Ja	Ku	Re_l, Cond	Re_l	Cond
b	11745577.25	34385.4	607387.0177	-	16099.64	3.72E-36
m1	-0.8899	0.7535		-	-0.24278	
m2	1.0126		0.4821	-		10.39713
R^2	0.9571	0.8253	0.9197	-	0.433506	0.000602

Table E-2: Regression coefficients for BTS 90° FR 0.5

	Regression hei			Regression hci		
Regression terms used	Ja, Ku	Ja	Ku	Re_l, Cond	Re_l	Cond
b	6336518.14	63548.1	1359101.762	1.59E-24	4923.056	5.7E-139
m1	-0.6875	1.0610		-0.4169	-0.4458	
m2	0.9348		0.5931	7.2852		37.4106
R^2	0.9819	0.8143	0.9578	0.8899	0.8807	0.3401

Table E-3: Regression coefficients for BTS 60° FR 1

	Regression h_{ei}			Regression h_{ci}		
Regression terms used	Ja, Ku	Ja	Ku	Re_l, Cond	Re_l	Cond
b	5560447.80	41874.62	1439942.01	7.11608E+39	1619.989	3.04E-13
m1	-0.3923	1.0151		-0.2089	-0.1887	
m2	0.8440		0.6098	-9.7253		4.0560
R^2	0.9946	0.9858	0.9939	0.8468	0.7898	0.0115

Table E-4: Regression coefficients for BTS 45° FR 1

	Regression hei			Regression hci		
Regression terms used	Ja, Ku	Ja	Ku	Re_l, Cond	Re_l	Cond
b	164238	19710	280735.0171	5.47E+08	151505.1	3.4E-255
m1	0.2007	0.7586		-0.55376	-0.54821	
m2	0.3434		0.4466	-0.94179		68.64456
R^2	0.9632	0.8703	0.9531	0.995389	0.995353	0.731022

Appendix F Regression coefficients for the CLTS experiments

The experimental set up, procedure and results of the closed loop thermosyphon (CLTS) experiments are discussed in section 4.2 on page 4-15. This section gives the regression coefficients for the evaporator and condenser inside heat transfer coefficients correlations. The regression coefficients were determined using the 'data regression' tool in MS Excel. The experimental data used in the determination of the regression coefficients are given in 'CLTS data butane.xls', 'CLTS data R134a.xls' and 'CLTS data water.xls' on the data DVD in Appendix A.

Appendix F.1 CLTS working fluid: R134a

Table F-1: Condenser inside heat transfer coefficient regression coefficients for CLTS with R134a as working fluid

Regression terms used	R_{el}, FC, d_i	R_{el}, FC	R_{el}, d_i	FC, d_i	R_{el}	FC
b	0.13024	5066.8	682.47	0.23195	1798.1	398.22
n1	0.007929	-0.12825	-0.10366		-0.10754	
n2	0.25871	-0.05542		0.2414		0.049893
n3	-0.98412		-0.203	-0.9316		
R^2	0.75	0.71	0.73	0.76	0.63	0.045
Average % difference	6.1	7.1	6.92	6.13	7.63	11.2
Maximum % difference	18.6	27.5	24.4	18.87	31.6	41.0

Table F-2: Evaporator inside heat transfer coefficient regression coefficients for CLTS with R134a as working fluid

Regression terms used	Ja, Ku, d_i	Ja, Ku	Ja, d_i	Ku, d_i	Ja	Ku
b	46501	17549	4987.2	303670	9687.8	9270.8
m1	0.41851	0.43559	0.48568		0.47972	
m2	0.0874	0.071938		0.172276		0.125658
m3	0.18654		-0.14628	0.65119		
R^2	0.59	0.56	0.50	0.21	0.51	0.09
Average % difference	18.3	18.1	20.0	31.3	20.2	32.0
Maximum % difference	64.7	69.9	79.8	134.7	76.6	172.6

Table F-3: Evaporator inside heat transfer coefficient regression coefficients for CLTS with R134a as working fluid

Regression terms used	Ja, Ku for 1/4"	Ja, Ku for 1/2"	Ja, Ku for 3/8"
b	76904.716	62677743	9948275
m1	1.0587224	-0.98381	-0.61069
m2	-0.0137391	1.255909	0.946487
R^2	0.8837237	0.015021	0.931391
Average % difference	8.0519967	5.06868	5.775161
Maximum % difference	15.775287	15.04323	20.39146

Appendix F.2 CLTS working fluid: Butane

Table F-4: Condenser inside heat transfer coefficient regression coefficients for CLTS with butane as working fluid

Regression terms used	Re_l, FC, d_i	Re_l, FC	Re_l, d_i	FC, d_i	Re_l	FC
b	3.4E-08	61.33729	8127.262	16.47056	1407.686	40.89213
n1	0.405281	-0.02001	-0.12005		-0.11338	
n2	0.621449	0.118914		0.148021		0.132101
n3	-1.69608		0.36847	-0.1215		
R^2	0.90298	0.823554	0.783686	0.833427	0.569378	0.814645
Average % difference	3.516666	5.183715	5.974679	5.133223	9.312557	5.144039
Maximum % difference	12.58395	17.97681	20.94318	17.15136	29.64834	18.0516

Table F-5: Evaporator inside heat transfer coefficient regression coefficients for CLTS with butane as working fluid

Regression terms used	Ja, Ku, d_i	Ja, Ku	Ja, d_i	Ku, d_i	Ja	Ku
b	146192.4	1064166	6874.176	39074.37	48455.87	1074087
m1	-1.03379	0.003677	1.022894		0.974365	
m2	1.287164	0.580911		0.692832		0.582873
m3	-1.32344		-0.4502	-0.95275		
R^2	0.982916	0.649678	0.624891	0.914956	0.567985	0.649585
Average % difference	4.495361	16.11195	21.30421	10.77168	20.93699	16.12169
Maximum % difference	14.91612	57.37345	113.0256	48.25089	110.2902	57.24375

Appendix F.3 CLTS working fluid: Water

Table F-6: Evaporator inside heat transfer coefficient regression coefficients for CLTS with water as working fluid

Regression terms used	Ja, Ku, d_i	Ja, Ku	Ja, d_i	Ku, d_i	Ja, Ku, d_i for FR 1	Ja, Ku for 3/8" FR 0.5	Ja, Ku for 3/8" FR 1	Ja, Ku for 1/2" FR 1
b	46353.05	4158.421	80247.88	22824.61	88746.24163	458249.9882	14723.26	8.884444
m1	0.215281	0.20838	0.094686		0.517575524	1.659923881	0.079248	0.794806
m2	-0.05098	-0.05751		-0.0208	-0.388846766	-0.004934014	0.118139	-0.94851
m3	0.508211		0.630014	0.475997	1.116521252			
R^2	0.59	0.41	0.30	0.24	0.86	0.99	0.91	0.90
Average % difference	8.6	9.7	13.7	13.4	4.6	1.0	3.6	3.9
Maximum % difference	82.1	96.1	61.8	60.1	10.8	2.3	8.5	9.8

Table F-7: Condenser inside heat transfer coefficient regression coefficients for CLTS with water as working fluid

Experiment	1/2" FR 1			3/8" FR 1			3/8" FR 0.5		
Regression terms used	Re_l, FC	Re_l	FC	Re_l, FC	Re_l	FC	Re_l, FC	Re_l	FC
b	1.94594	1541.33	221435	2.09E+20	60.9017	1.7E-155	2.48E-11	1668.24	2048.06
n1	0.16668	0.0790		0.771681	0.72393		0.54325	0.128113	
n2	0.28176		-0.20769	-2.0332		17.22653	1.399777		0.012156
R^2	0.91896	0.824372	0.59605	0.996837	0.99118	1.92E-31	0.930023	0.188821	0.001321
Average % difference	1.46029	2.0700	3.376678	3.646541	5.71486	1698.448	2.12994	7.097715	7.43761
Maximum % difference	3.5986	5.504092	6.538213	9.301276	12.9249	6793.894	3.471489	11.72159	13.1703